Manipulating the inverse Faraday effect at the nanoscale

Xingyu Yang

Sorbonne University

Physique en Île-de-France (ED 564)

Institut des nanosciences de Paris (INSP) / Nanophotonics and Quantum Optics

Manipulating the inverse Faraday effect at the nanoscale

Reported by Xingyu YANG

PhD Thesis in Physics

Supervised by Mathieu MIVELLE

Defense Date September 27, 2024

Defense Committee:

COLAS DES FRANCS Gérard	Professeur	Reviewer
SALAS MONTIEL Rafael	Ingénieur de recherche HDR	Reviewer
BAIDA Fadi	Professeur	Examiner
SAINCTAVIT Philippe	Directeur de recherche	Examiner
ELSAWY Mahmoud	Inria Starting Faculty Position (ISFP)	Examiner
MIVELLE Mathieu	Chargé de recherche	Thesis director

Manipulating the inverse Faraday effect at the nanoscale

RÉSUMÉ

Le magnétisme induit par la lumière désigne le phénomène par lequel un matériau est magnétisé par une impulsion optique. Dans les matériaux transparents, cette magnétisation peut être directement induite par une lumière polarisée circulairement. De même, dans les matériaux métalliques, la lumière polarisée circulairement peut entraîner des électrons le long de trajectoires solénoïdales microscopiques, ce qui entraîne une magnétisation. Parfois, la lumière génère des courants macroscopiques continus qui induisent une magnétisation continue dans les métaux. Collectivement, ces phénomènes font partie de l'effet Faraday inverse.

Dans le cadre de cette recherche doctorale, j'ai étudié les courants de dérive induits par la lumière dans diverses nanoantennes en or, afin d'obtenir des champs magnétiques stationnaires améliorés par effet plasmonique. Pour cette étude, j'ai utilisé la méthode FDTD (Finite-Difference Time-Domain) ainsi que les théories appropriées sur le magnétisme induit par la lumière. Tout au long de cette thèse, nous avons analysé les propriétés optiques de différentes nanoantennes et élucidé les mécanismes physiques à l'origine des courants de dérive induits par la lumière et des champs magnétiques stationnaires. Nous avons démontré une méthode permettant d'obtenir des effets de Faraday inverses renforcés par des plasmons et exploré la faisabilité de la magnétisation par une lumière incidente polarisée linéairement. En outre, nous avons étendu l'effet Faraday inverse à de nouveaux domaines de recherche, notamment la création de skyrmions par le biais de champs magnétiques stationnaires.

Les effets magnétiques induits par la lumière restent un domaine de recherche riche et prometteur. Les résultats de cette étude ont des applications potentielles dans divers domaines, tels que les matériaux et dispositifs magnéto-optiques, le stockage optique de données, les applications biomédicales, la spintronique, l'informatique quantique, la recherche fondamentale en électromagnétisme et la science des matériaux.

MOTS CLÉS: effet Faraday inverse, nanoantenne plasmonique, manipulation du champ optique, courant de dérive, magnétisme induit par la lumière

ABSTRACT

Light-induced magnetism refers to the phenomenon where a material becomes magnetized by an optical pulse. In transparent materials, this magnetization can be directly induced by circularly polarized light. Similarly, in metallic materials, circularly polarized light can drive electrons along microscopic solenoidal paths, resulting in magnetization. Occasionally, light generates macroscopic circulating DC drift currents, which further induce DC magnetization in metals. Collectively, these phenomena are termed the inverse Faraday effect.

In this PhD research, I investigated light-induced drift currents in various gold nanoantennas, achieving plasmonically enhanced stationary magnetic fields through these currents. The study utilized the Finite-Difference Time-Domain (FDTD) method alongside pertinent theories of light-induced magnetism. Throughout these projects, we analyzed the optical properties of different nanoantennas and elucidated the physical mechanisms behind light-induced drift currents and stationary magnetic fields. We demonstrated a method to achieve plasmonically enhanced inverse Faraday effects and explored the feasibility of magnetization through linearly polarized incident light. Furthermore, we extended the inverse Faraday effect to new research domains, including the creation of skyrmions via stationary magnetic fields.

The magnetic effects induced by light remain a rich and promising field of research. The findings of this study have potential applications in various areas, such as magneto-optical materials and devices, optical data storage, biomedical applications, spintronics, quantum computing, fundamental electromagnetism research, and advanced materials science.

KEY WORDS: inverse Faraday effect, plasmonic nanoantenna, optical field manipulation, drift current, light-induced magnetism

Table of contents

1 Introduction

Optics is the branch of physics that studies the behavior and properties of light, with the interaction between light and matter playing a key role throughout the long history of optical research. Light-matter interaction refers to the ways in which light (electromagnetic radiation) interacts with matter (atoms, molecules, nanoparticles, etc.). This interaction is fundamental to numerous phenomena in physics, chemistry, and technology.

1.1 Research background

1.1.1 Light-matter interaction in nanoscale

Early in the 4th century, the Roman people had already created the Lycurgus Cup (Figure 1-1), a type of glass that exhibits different colors depending on whether light is passing through it[1]. This demonstrates an early application, intentional or not, of the principles of light-matter interaction on the nanoscale. In the 20th century, nanotechnology gained significant attention and rapidly developed. The American physicist Richard Feynman delivered a lecture titled "There's Plenty of Room at the Bottom" at an American Physical Society meeting[2]. In this lecture, Feynman described a process that might be developed to manipulate individual atoms and molecules using one set of precise tools to build and operate another, proportionally smaller set, continuing down to the micro-nano scale. He noted that as a result of this, scaling issues would arise from the changing magnitude of various physical phenomena. Photonics research, as a typical field at the micro-nano scale, greatly benefited from these advancements in nanotechnology. The study of light-matter interactions received increased attention due to the significant progress in nanotechnology, enabling deeper investigation into the mechanisms of light and matter[3]. These studies are now known as nano-optics.

Nano-optics is the science that studies the interaction between light and matter at the micro and nano scale. The micro-nano scale lies between classical electromagnetism and quantum mechanics. In this region, the properties of light-matter interaction are determined by scale effects[4], leading to many novel characteristics such as extraordinary transmission[5, 6] and reflection[6], high absorption[7, 8], local field enhancement[4, 9, 10], directional scattering[11, 12], photothermal conversion[13-15], inverse Faraday effect (IFE)[16-18], and light-induced stationary magnetic fields[19, 20], etc.

(a)  (b) 

Figure 1-1. (a) The Lycurgus Cup is a 4th-century Roman glass cage cup. The Lycurgus Cup displays (a) a red color when illuminated from behind and (b) a green color when viewed from the front. [This file is licensed under the CC BY-SA 3.0 Deed | Attribution-ShareAlike 3.0 Unported license. https://en.wikipedia.org/wiki/Lycurgus_Cup]

Nowadays, nano-optics has become a well-developed scientific discipline that specifically studies light-matter interactions at the micro-nano scale. In this scale, light strongly couples with nanostructures, enabling phenomena such as negative refractive index[21], negative permittivity[22], negative permeability[23], and breaking the diffraction limit of half the wavelength to achieve super-resolution imaging[24]. These amazing electrical, magnetic, mechanical, and chemical properties show great potential in the development of next-generation optical devices[25].

1.1.2 Magnetic effect of light

Among all these novel characteristics during light-matter interaction, we study the magnetic effect of light. The magnetic effect of light primarily describes the interaction between light and the magnetism of materials, encompassing various aspects such as the photomagnetic effect[26], photomagnetoelectric effect[27], and magneto-optical effect[28]. Each of these effects has different physical mechanisms and applications. Here, we simply divide these magnetic effects into two types according to their mechanisms.

1) Interaction between Light and Magnetized Matter

This type of magnetic effect requires magnetized matter or an external static magnetic field, including the Faraday effect[29], Kerr magneto-optical effect[30], Zeeman effect[31], and Cotton-Mouton effect[32]. For instance, Figure 1-2 displays the schematic of the Faraday

effect[29]. For a transparent solid or liquid placed in a uniform magnetic field, if a polarized plane wave passes through it in the direction parallel to the magnetic field, the transmitted light remains plane polarized, but the plane of polarization is rotated by an angle. The rotation angle depends on the direction of the magnetic field and is proportional to the field intensity. This optical rotation is called the Faraday effect.

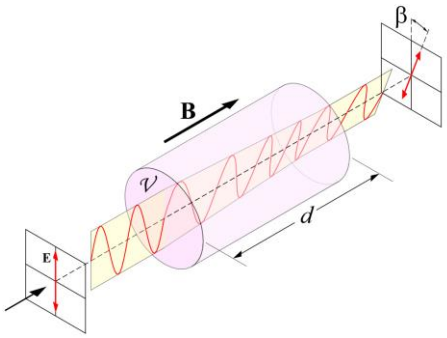

Figure 1-2. Illustration of the Faraday Effect. (A) A left circularly polarized light incident on a material induces a magnetization opposite to the direction of light propagation, while (B) a right circularly polarized light creates this magnetization in the direction of light propagation. [This file is licensed under the CC BY-SA 3.0 Deed | Attribution-ShareAlike 3.0 Unported license. https://en.wikipedia.org/wiki/Faraday_effect#/media/File:Faraday-effect.svg]

The Faraday effect can be simply explained by considering linearly polarized light as a superposition of right-handed and left-handed circularly polarized beams. We can then examine the effects of each component (right-handed or left-handed polarized) separately. In the case of circularly polarized light, the direction of the electric field rotates at the frequency of the light, either clockwise or counterclockwise. In a material, this electric field causes a force on the charged particles, leading to their circular motion. As a result, a magnetic field is induced by these motions. The induced magnetic field has the same direction or the opposite direction with respect to the propagating direction of light, depending on the handedness of the light. In the presence of an external static magnetic field, the induced magnetic field will increase or decrease the total magnetic field. For this reason, right-handed and left-handed polarized light behave differently in the material; one of them will be slowed more than the other, causing a phase difference between the left- and right-polarized beams. When the two beams are combined after this phase shift, the result is again a linearly polarized beam, but with a rotation of the polarization vector.

The Faraday effect describes the influence of a static magnetic field applied to the transmitted light in a transparent material. However, sometimes magneto-optical interactions occur directly if the material itself is magnetized. The magneto-optic Kerr effect (MOKE) is

an example of this case[30]. It describes the changes to light reflected from a magnetized surface, including polar MOKE, longitudinal MOKE, and transverse MOKE. These effects are categorized by the direction of the magnetization vector with respect to the reflecting surface and the plane of incidence, as depicted in Figure 1-3.

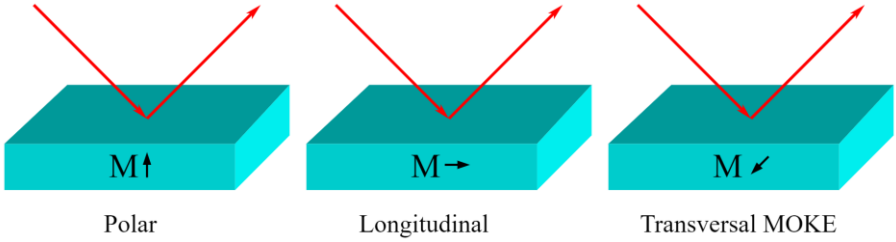

Figure 1-3. MOKE can be further categorized based on the orientation of the magnetization vector relative to the reflecting surface and the plane of incidence. These categories are known as polar MOKE, longitudinal MOKE, and transversal MOKE, respectively. [This file is licensed under the CC BY-SA 3.0 Deed | Attribution-ShareAlike 3.0 Unported license. https://en.wikipedia.org/wiki/Magneto-optic_Kerr_effect#cite_note-1]

Similar to the Faraday effect, MOKE also describes the change in the polarization angle applied to incident light. It occurs when the incident light reflects from the surface of a magnetic material. Here, we choose the polar Kerr effect as an example. As seen in Figure 1-4, when the magnetization vector is perpendicular to the reflection surface and parallel to the plane of incidence, the light reflected from this magnetized surface will experience a rotation in polarization. Similar to the Faraday effect, MOKE can also be explained by considering right-handed and left-handed circularly polarized beams independently. One can then refer to the case of linearly polarized light.

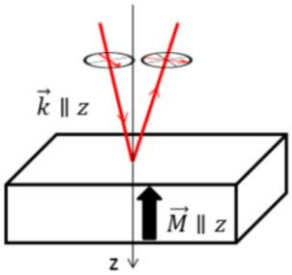

Figure 1-4. Polar Kerr effect. When linearly polarized light is incident on a magnetic material, the reflected light undergoes a rotation in the polarization angle. [This file is licensed under the CC BY-SA 3.0 Deed | Attribution-ShareAlike 3.0 Unported license. https://en.wikipedia.org/wiki/Voigt_effect]

Therefore, this type of magnetic effect in light-matter interaction depends on an external

magnetic field or the magnetization of the material itself. The other type of magnetic effect of light refers to the phenomenon where the magnetism of materials changes after light is applied to the material.

2) Change of Magnetism Induced by Light

Photomagnetism is the effect where a material acquires or loses its ferromagnetic properties in response to light[33]. The current model for this phenomenon is a light-induced electron transfer, accompanied by the reversal of the spin direction of an electron. In this process, the magnetic susceptibility, magneto-crystalline anisotropy, and hysteresis loop of the material may be influenced by incident light. This leads to an increase in spin concentration, causing the magnetic transition.

There are also studies related to the change of magnetism induced by light, specifically light-induced magnetization[20, 34], where non-magnetic materials gain magnetization from circularly polarized light[17, 35]. These phenomena are also known as the inverse Faraday effect[16, 17], as displayed in Figure 1-5. The IFE occurs when circularly polarized light incident on a non-absorbing crystal induces a magnetic moment proportional to the Verdet constant of that material.

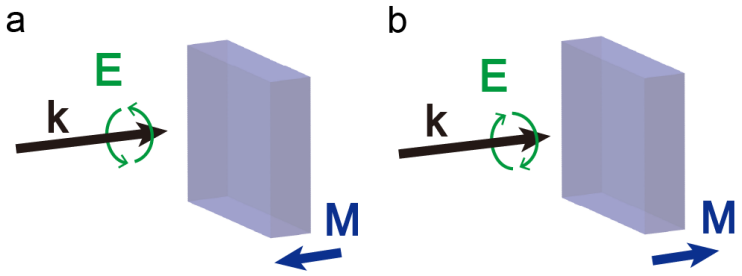

Figure 1-5. Illustration of the Inverse Faraday Effect. (a) When left circular polarization is incident on a material, it induces magnetization opposite to the direction of light propagation. (b) When right circular polarization is incident on a material, it creates magnetization in the direction of light propagation. This effect demonstrates how circularly polarized light can influence the magnetization direction in non-absorbing materials, known as the inverse Faraday effect.

The induced magnetization can have the same direction or opposite direction as the light's propagating direction, depending on the handedness of the light. As depicted in Figure 1-5, left circular polarization incident on a material induces magnetization opposite to the direction of light propagation, whereas right circular polarization creates magnetization in the direction of light propagation. As explained in the description of the Faraday effect, circularly polarized light induces a circular motion of charged particles within the material, which is the underlying

mechanism behind the induced magnetization. The inverse Faraday effect was initially studied in transparent materials[17], and later expanded to include plasma[18] and metallic materials[16, 19].

These effects not only demonstrate the diversity of magnetic interactions between light and matter, but also provide new perspectives and tools for optical research and applications. They contribute significantly to advancing our understanding of how light can manipulate magnetic properties in various types of materials.

1.1.3 Research interests

In this PhD project, I am focusing on the plasmonic-enhanced photomagnetic effect in gold nanoantennas[19, 20]. Gold is the most commonly used metallic material in plasmonic research. Traditionally, gold is considered non-ferromagnetic and does not typically respond to magnetic fields. However, metallic materials contain numerous free electrons, and electrons are integral to the origin of magnetism. Whether viewed through the electron spin dipole moment in quantum mechanical theory or Ampère's molecular current explanation of magnetism, electrons play a crucial role.

In early publications, researchers hypothesized that metallic materials could exhibit magnetism under the influence of circularly polarized light, arising from specific motions of these free electrons[16]. Subsequently, this light-induced magnetism in metals was both theoretically predicted and experimentally verified[19, 20], a phenomenon known as the inverse Faraday effect.

A typical constraint of the IFE is its small magnitude of magnetization. Compared with general research on ferromagnetic materials, this light-induced magnetization is almost negligible. However, in nano-optics, the IFE might find applications because we can greatly enhance this light-induced magnetization by utilizing surface plasmonic resonance (SPR) through nanoantennas[19].

The IFE in metallic materials requires high-frequency electromagnetic waves. Noble metals are known to sustain multipole resonances in nano-optics research[9], and plasmonic resonance also demands high-frequency electromagnetic waves. Therefore, the prerequisites for IFE study in metals align perfectly with the excitation conditions of surface plasmon resonance. For this reason, the disadvantage of the IFE could be overcome by introducing SPR into IFE studies.

By leveraging SPR in IFE studies, the disadvantage of small magnetization magnitude can be addressed. The enhanced electromagnetic field confinement and intensity near nanoantennas can amplify the light-matter interaction, potentially leading to significant

improvements in light-induced magnetization effects observed in metallic materials[19, 36]. This approach opens up new avenues for utilizing IFE in practical applications within nano-optics and related fields.

1.2 Research status

To better understand surface plasmonic resonance and the inverse Faraday effect, we investigate the development of surface plasma research and IFE studies, respectively. We then highlight some recent work in this cross-research area that has already linked SPR with light-induced magnetization.

1.2.1 Surface plasmonic resonance

The SPR phenomenon has gained increasing attention since its first discovery in 1902 by R.W. Wood[37]. While studying diffraction gratings, Wood noticed some anomalies in the reflection spectrum. As depicted in Figure 1-6, he was astounded to find that under certain incident angles, the reflection intensity showed a sudden drop. In his words, "a change of wavelength of 1/1000 is then sufficient to cause the illumination in the spectrum to change from a maximum to a minimum."

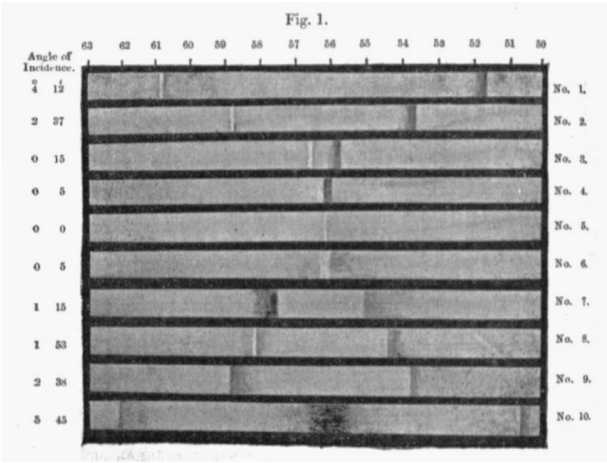

Figure 1-6. Anomalous reflection of metal grating discovered by R.W. Wood. The X-axis represents wavelength, the Y-axis denotes various incident angles, and the color indicates reflection intensity. [Figure from: R. Wood, 1902, On a remarkable case of uneven distribution of light in a diffraction spectrum, *Proceedings of the Physical Society of London*, Vol. 18 Issue 1 Pages 269-275]

No clear theoretical explanation was given at that time, but Wood made some pioneering observations from his experiments. 1) The diffraction grating has certain conditions under which these anomalies appear, as the drop in intensity only occurred at specific incident angles. 2) Polarization is key to explaining this singular behavior, as he found that the singular anomalies were exhibited only when the polarization direction was at a right angle to the grating.

The first theoretical explanation of these anomalies was given by Lord Rayleigh in 1907[38]. He proposed a dynamical theory of the grating based on an expansion of the scattered electromagnetic field in terms of outgoing waves. With this assumption, he found that the scattered field was singular at wavelengths for which one of the spectral orders emerged from the grating at the grazing angle. He observed that these wavelengths, now called the Rayleigh wavelengths, correspond to the Wood anomalies. Furthermore, these singularities appeared only when the electric field was polarized perpendicular to the rulings, consistent with Wood's experimental conclusions. His theory successfully predicted the normal behavior near the Rayleigh wavelength in Wood's later papers.

In 1941, U. J. Fano explained this phenomenon through a surface electromagnetic wave at the metal-dielectric interface[39]. He made a Fourier expansion of the dielectric constant and conductivity, characterizing these optical parameters by the metallic reflection grating due to its periodic profile (Figure 1-7a). In this way, the influence of the grating's geometry was quantified. Fano considered multi-order waves with different tangential momenta diffracted by the metallic grating and successfully matched the diffracted wave with the spatial periodicity of the metallic grating. He particularly emphasized the contribution of "superficial waves" traveling along the surface of the grating and exponentially damped in the normal direction, now known as surface waves. Fano further summarized the main elements influencing the intensity in Wood's experiment: 1) the wavelength of the light; 2) the angle of incidence; 3) the angle of emergence of the diffracted waves; 4) the geometry of the grating; 5) the optical properties of the metal; and 6) the polarization. Fano's conclusions aligned with the modern understanding of SPR phenomena, paving the way for further surface plasmon research.

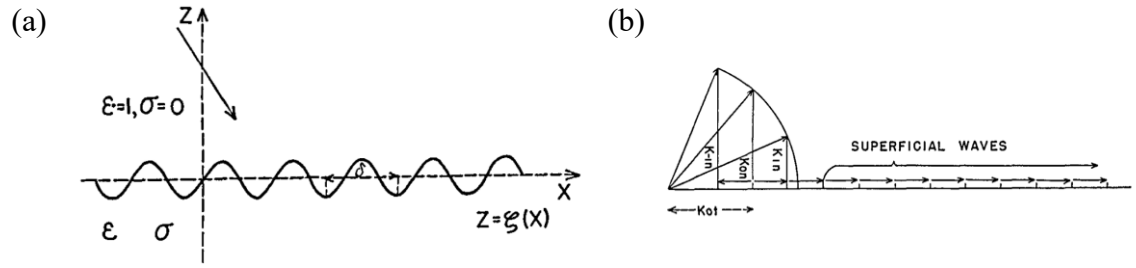

Figure 1-7. U.J. Fano explained the anomalous reflection phenomenon through a surface electromagnetic wave at the metal-dielectric interface. (a) The periodic optical parameters, such as the dielectric constant and conductivity, define the characteristics of the metallic reflection grating. (b) Fano constructed the normal momentum component of the diffracted wave to elucidate how the anomalous reflection occurs. [Figure from: U. Fano, 1941, The theory of anomalous diffraction gratings and of quasi-stationary waves on metallic surfaces (Sommerfeld's waves), *JOSA*, 31(3): 213-222]

Later in 1957, in a study of energy losses in metallic thin films, R.H. Ritchie assumed that the conduction electrons constitute a Fermi-Dirac gas[40]. He concluded that the energy distribution of electrons exhibited both collective and individual interaction characteristics. The assumption of an electron gas in metals has been widely accepted since then. Ritchie noticed the collective behavior of electrons in metallic thin films and further pointed out that the excitation of this collective behavior relied on the interface of the metal film, predicting the collective oscillation of excited electrons on the metal surface. Subsequent experiments on electron energy losses in gases and thin foils revealed that the energy loss resulted from the excitation of a surface plasma oscillation, with part of the restoring electric field extending beyond the specimen boundary. Following Ritchie's theory, E.A. Stern and R.A. Ferrell formally proposed the concept of the surface plasmon (SP) in 1960[41]. This marked the first official naming of the surface plasmon.

In 1963, Mcalister and Stern successfully stimulated surface plasmon polaritons (SPPs) in a silver film using light[42]. They measured the transmission of light with different wavelengths and incident angles passing through the thin silver. P-polarized and s-polarized light were applied, respectively. As predicted, a drop in transmission occurred in the vicinity of the plasma frequency only for the p-polarized light. For this reason, they emphasized that the drop in transmission observed in this experiment could only be explained as the excitation of a collective mode (Figure 1-8) and could not be attributed to an interband-absorption effect. An interband absorption would result in dips for both s and p polarization at all angles of incidence.

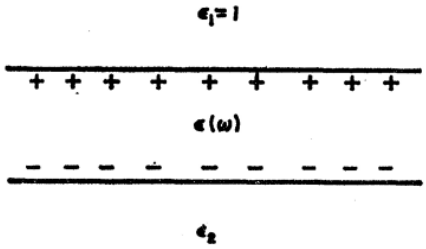

Figure 1-8. Illustration of the type of plasma oscillation excited. Charges appear only at the surfaces, with zero volume charge density. [Figure from: A. J. McAlister and E. Stern, 1963, Plasma resonance absorption in thin metal films, *Physical Review*, Vol. 132 Issue 4 Pages 1599]

Figure 1-8 shows the schematic of surface plasma oscillation, where the oscillation can be initiated by a displacement of the electrons in the film, producing a negative surface charge on one face and a positive surface charge on the other face, with no volume charge present. Mcalister and Stern further accurately determined the plasma frequency of the silver film associated with this drop in the transmission spectrum. Their study confirmed Ferrell's model of the coupling between electromagnetic radiation and a surface plasma mode in thin metallic films. Additionally, the presence of any film or contaminant on the specimen surface affects the surface plasma oscillation. This effect was later described in terms of the excitation of electromagnetic "evanescent" waves at the surface of the metal, and evanescent waves became a means to study ultra-thin metal films and coatings.

In 1968, A. Otto proposed a simple method to excite surface plasmon waves through a prism[43], a method still widely used today, known as the Otto configuration. He demonstrated that the phase velocity of the surface plasmon wave at a metal-vacuum surface is smaller than the velocity of light in a vacuum, as seen in Figure 1-9a. The curve describes the dispersion relation of the nonradiative surface plasmon wave at a metal-vacuum surface, while the straight line represents the dispersion of plane electromagnetic waves in a vacuum. In Figure 1-9a, the plane wave and surface plasmon wave cannot coexist simultaneously. Therefore, these waves cannot be excited by light striking the surface, as long as the surface is perfectly smooth.

According to Otto’s research, if a prism is brought near the metal-vacuum interface, the SPW can be excited optically by the evanescent wave present in total reflection, as depicted in Figure 1-9b. Otto’s method was observed as a strong decrease in reflection for the transverse magnetic light at a specific angle of incidence. The decreased energy in reflection was coupled to excite plasma oscillation at the metal-vacuum interface. Otto demonstrated that the nonradiative surface plasma wave could be coupled to light waves, without using surface roughness, by the method of frustrated total reflection from a high refractive index medium.

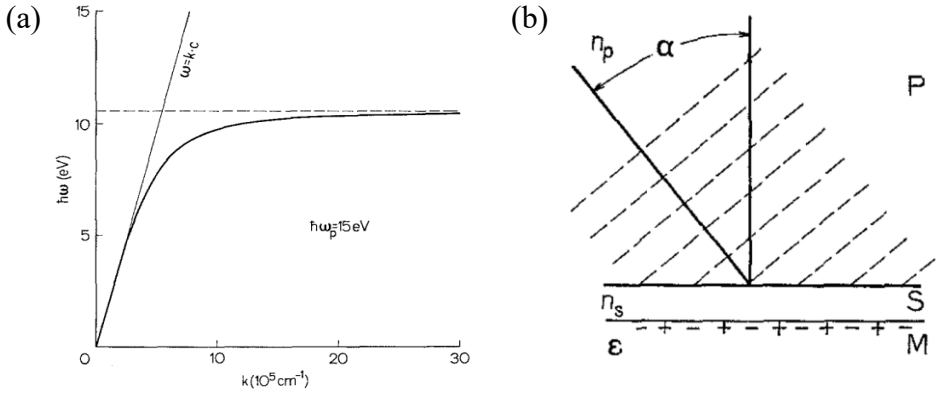

Figure 1-9. (a) The dispersion relation of the nonradiative surface plasma wave at the metal-vacuum interface. The X-axis represents the wavenumber k, while the Y-axis indicates the frequency of the wave, marked in electron volts. The straight line represents the dispersion relation of plane electromagnetic waves in vacuum. (b) A plane wave incident from prism (P) at an angle α upon an interface composed of prism (P), dielectric (S), and metal (M). The broken lines depict the equal phase planes of the incident wave. The plus (+) or minus (-) signs symbolize the surface charge wave. [Figure from: A. Otto, 1968, Excitation of nonradiative surface plasma waves in silver by the method of frustrated total reflection, *Zeitschrift für Physik A Hadrons and nuclei*, Vol. 216 Issue 4 Pages 398-410]

Kretschmann proposed a similar method to couple SPPs with evanescent waves from totally reflected light at the metal-air interface, known as the Kretschmann configuration[44]. As displayed in Figure 1-10, a metal film is attached to the prism. The light again illuminates from the prism, and an evanescent wave penetrates through the metal film. In 1982, Boardman edited the book "Electromagnetic Surface Modes," comprehensively summarizing this surface electromagnetic motion from both theoretical and experimental perspectives. By then, a complete theoretical and experimental system had been established.

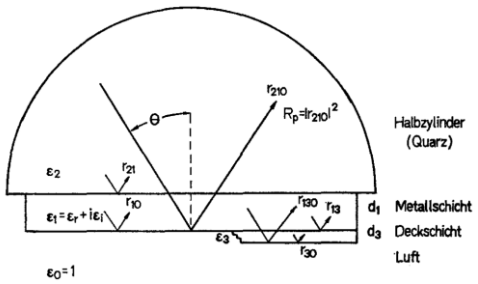

Figure 1-10. The Kretschmann configuration operates on the same principle as Otto's method, where light interacts with a metal film to excite SPPs. However, in the Kretschmann configuration, the light penetrates through the metal film and interacts specifically at the metal-air interface to excite SPPs. [Figure from: E. Kretschmann, 1971, Die bestimmung optischer konstanten von metallen durch anregung von oberflächenplasmaschwingungen, *Zeitschrift fur physik*, Vol. 241 Issue 4 Pages 313-324]

Benefiting from the greatly developed fabrication technologies after the 21st century, researchers have also focused on SPR phenomena in tiny objects, known as localized surface plasmon resonance (LSPR)[9, 45, 46]. LSPR is the result of the confinement of a surface plasmon in a nanoparticle smaller than the wavelength of incident light. In LSPR, the electronic gas oscillates along the periodic force applied by the light on the nanoparticles, resulting in a greatly enhanced electric field near the particle's surface. This oscillation frequency is determined by the density of electrons, the effective electron mass, and the size and shape of the charge distribution.

1.2.2 Light-induced dc magnetization

The light-induced DC magnetization was first mentioned in 1963 by P.S. Pershan in his research on the nonlinear optical properties of solids[35]. In his paper, he described the interaction between macroscopic, nondissipative media and time-varying electromagnetic fields using a time-averaged potential function. Linear and nonlinear phenomena, including DC magnetization, could be derived from several forms of this potential function. He concluded that if one initially has a circularly polarized optical field propagating in a direction, there will be a magnetization at zero frequency oriented in the same direction. This was an early description of the IFE. Notably, he discussed the reciprocal nature of this effect, demonstrating that the Faraday effect and the production of DC magnetization due to incident circularly polarized light are reciprocal effects.

Two years later, in 1965, Pershan focused on this optically induced magnetization and named it the inverse Faraday effect[17]. At that time, IFE had been observed in Eu^{+2}:CaF_2 , several diamagnetic glasses, and various organic and inorganic liquids. All measurements were done in the absence of an applied DC magnetic field, unlike the Faraday effect. Pershan also experimentally confirmed IFE in Eu^{+2} doped CaF_2 via the temperature dependence of the magnetization, as seen in Figure 1-11.

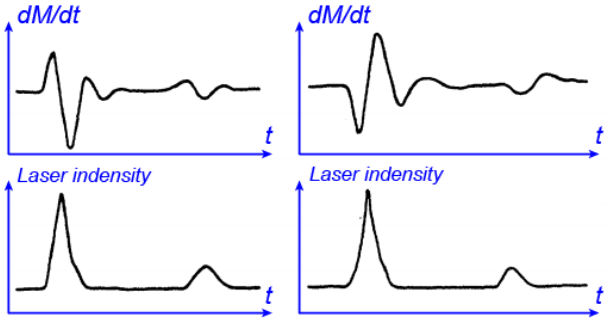

Figure 1-11. Experimental observation of IFE in Eu^{+2} doped CaF_2. Top panel shows oscilloscope traces of d*M*/d*t* obtained with right and left circularly polarized light, where *M* indicates magnetization and *t* represents time. Bottom panel depicted monitor of the laser intensity. The coordinate system (blue) here is added additionally to original results for better comprehension. [Figure from: J. Van der Ziel, P. S. Pershan and L. Malmstrom, 1965, Optically-induced magnetization resulting from the inverse Faraday effect, *Physical review letters*, Vol. 15 Issue 5 Pages 190]

The magnetization induced by a circularly polarized pulse beam was clearly displayed on an oscilloscope. For right and left circularly polarized light, the magnetization had opposite directions. This was an early observation of optically induced magnetization in a non-absorbing material.

In 1970, J. Deschamps, M. Fitaire, and M. Lagoutte demonstrated the IFE in plasma[18]. Their experiment showed that a magnetic field could be generated by electrons in a plasma when subjected to high-power pulses of circularly polarized microwaves. These findings confirmed the theoretical predictions of IFE in plasma. According to their research, when exposed to the electric field of a circularly polarized wave with angular frequency ω_0, electrons in the plasma undergo circular orbits with a frequency of $\omega_0/(2\pi)$. Each electron thereby acquires a magnetic moment, and the collective effect of these magnetic moments results in an induced magnetic field (B). This discovery provided empirical evidence of how circularly polarized microwaves can induce a significant magnetic response in plasma, extending the understanding and applications of IFE beyond solid-state materials to plasma environments. They further measured the induced magnetic field experimentally through a voltage proportional to the time derivative of B, as seen in Figure 1-12.

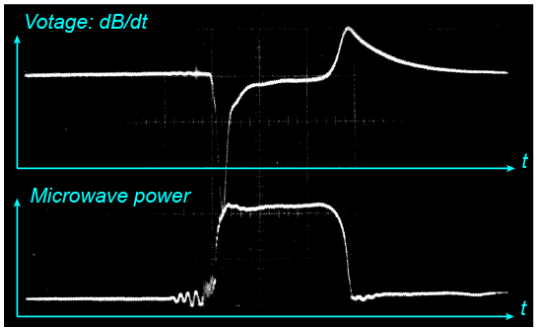

Figure 1-12. Detection of magnetic field induced by circularly polarized pulse beam. Bottom line represents the incident microwave pulse. Top line is the detected voltage that proportional to the time derivative of B. The coordinate system (light blue) here is added additionally to original results for better comprehension. [Figure from: J. Deschamps, M. Fitaire and M. Lagoutte, 1970, Inverse Faraday effect in a plasma, *Physical Review Letters*, Vol. 25 Issue 19 Pages 1330]

The voltage was induced by the variation of the magnetic flux. In their inferences, since the microwave pulses have a rise time and decay time, the variation of voltage was slow enough to be detected. Figure 1-12, two peaks had opposite signs. The first peak corresponded to the beginning of the pulse, and the second to the end of the same pulse. It was also noted that the first peak had a larger amplitude than the second. They explained this phenomenon by the origins of the two peaks: the first peak resulted from both the variation of the plasma itself (with frequency ω_p) and the electric field inside the plasma, while the second peak resulted solely from the variation of the electric field. When the handedness of incident light was inverted, the voltage changed its sign as expected for the effect of a magnetic field. This research verified that magnetization induced by circularly polarized light exists not only in transparent media but also in plasma. Their research paved the way for IFE studies in metallic materials, where free electrons can sometimes be treated as an electron gas and behave similarly to plasma.

In 2006, R. Hertel introduced a microscopic approach based on the Drude approximation of a free electron gas[16], identifying the magnetization in metallic materials due to the IFE as the result of microscopic solenoidal currents generated by incident electromagnetic waves. Compared to the relatively well-known phenomenological treatment of the IFE, the microscopic derivation presented in Hertel's theory provides clearer insight into the processes leading to the magnetization of the sample. Consequently, the same expression for DC magnetization as Y. Pomeau's derivation in 1967 was given[47]. An important aspect of Hertel's expression of the IFE is that it is free of material constants, allowing for quantitative predictions of the IFE. In particular, a strong dependence of the magnetization generated by the IFE on the frequency of the applied field is predicted.

In 2009, X. J. Chen investigated the trajectory of electrons under the influence of a circularly polarized light beam[48]. His study revealed that the electron's path generates a solenoidal current (Figure 1-13), leading to the creation of a magnetic moment for each electron. By averaging these magnetic moments across a unit volume of a free electron gas, Chen provided a straightforward microscopic explanation that aligned with R. Hertel's theoretical framework for the IFE in metals[16]. Hertel's earlier work proposed that the magnetization induced by IFE in metallic materials originates from microscopic solenoidal currents induced by incident electromagnetic waves. Chen's study validated this concept by demonstrating how the individual magnetic moments generated by electron orbits under circularly polarized light contribute to the overall magnetization observed in IFE experiments. Therefore, Chen's findings further supported the understanding of IFE at the microscopic level, reinforcing the theoretical foundation laid by Hertel and providing additional insights into the physical mechanisms underlying this intriguing optical phenomenon in metallic systems.

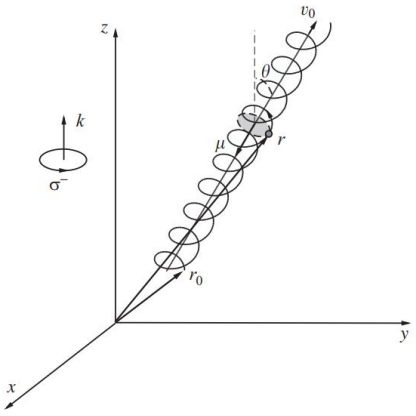

Figure 1-13. The solenoidal orbit of a free electron driven by a left-handed circularly polarized beam. The solenoidal current generates a magnetic moment. [Figure from: H.-L. Zhang, Y.-Z. Wang and X.-J. Chen, 2009, A simple explanation for the inverse Faraday effect in metals, *Journal of magnetism and magnetic materials*, Vol. 321 Issue 24 Pages L73-L74]

These studies provided theoretical and experimental verification of the existence of the IFE in transparent media, plasma, and metallic materials.

1.2.3 Plasma enhanced light-induced magnetization

As mentioned before, gold is a non-ferromagnetic material and shows no magnetic effect. However, according to IFE theory, metal can be magnetized by circularly polarized light. This light-induced magnetization is relatively weak compared to natural ferromagnetic materials.

On the other hand, noble metals are known to enable multiple surface plasmon modes, such as SPR in thin layers or LSPR in nanoparticles. In plasmonic resonance modes, the electric field, magnetic field, and energy are extremely confined in the vicinity of the nanostructure, indicating that the IFE could also be enhanced[19].

In 2017, M. Sheldon's group combined surface plasmon resonance and IFE research. They analyzed non-magnetic gold (Au) metal nanostructures, providing insight into the plasmonic enhancement of the magnetic and optoelectronic phenomena associated with the IFE[19]. Different from Hertel's theory, which is based on analysis in the frequency domain, Sheldon reported a simple numerical approach for tracking the optically induced motion of electrons in time inside plasmonic nanostructures that gives rise to the IFE.

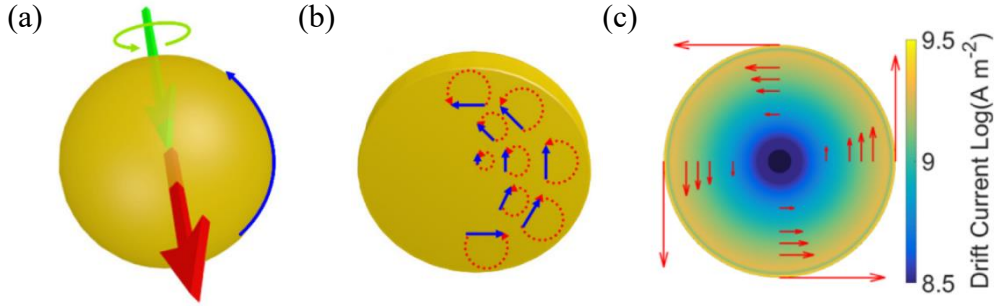

Figure 1-14. Plasmonic enhanced IFE. (a) Schematic of Au nanosphere, circularly polarized incident light (green arrow), and light-induced dc current (blue arrows). (b) A schematic view in cross section shows solenoid-like paths for each electron (red dotted curves) due to the forces experienced during the optical cycle. (c) Macro distribution of drift currents in Au nanoparticle. [Figure from: A. Nadarajah and M. T. Sheldon, 2017, Optoelectronic phenomena in gold metal nanostructures due to the inverse Faraday effect, *Optics Express*, Vol. 25 Issue 11 Pages 12753-12764]

As displayed in Figure 1-14a, an Au spherical nanoparticle under circularly polarized illumination (green arrow) would generate a static magnetic field (red arrow) along the optical axis, as well as circulating drift currents (blue arrow) due to the IFE. Figure 1-14b shows the trajectory of electrons; this nearly harmonic displacement motion of all the electrons is the primary mechanism producing the static magnetic field. However, optical field gradients inside the metal cause the electron trajectories to start and end at slightly different positions during one optical cycle, producing a net drift current (small blue arrows, not to scale). The drift current circulates through the entire structure with the same chirality as the optical source, providing a secondary contribution to the total static magnetization. Therefore, both solenoid-like currents in the micro region and the drift currents macroscopically distributed in the Au particle (Figure 1-14c) contribute to a static magnetic field. Both benefit from the enhanced E field in LSPR. For this reason, Sheldon's results indicated a significant enhancement of the

IFE in Au nanoparticles due to the larger optical field and field gradients compared to bulk Au films. This strong IFE had a spectral dependence on LSPR. Their study informed the development of new types of advanced magneto-optic materials.

Later in 2020, M. Sheldon's group experimentally measured light-induced magnetism in plasmonic gold nanoparticles[20]. They introduced an experimental quantification of optically induced magnetization in plasmonic gold nanoparticles due to the inverse Faraday effect. When Au nanospheres were illuminated by RHCP and LHCP, a DC magnetization was induced, with the direction depending on the polarization state. This DC magnetization led to a Faraday rotation of linearly polarized light. The strength of magnetization was experimentally measured through a comparative experiment, as seen in Figure 1-15.

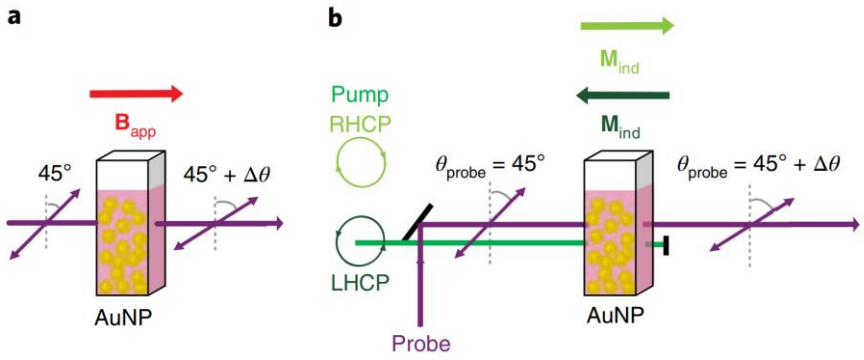

Figure 1-15. Experimental measurement of plasmonic enhanced IFE. (a) Schematic of the Faraday effect and the IFE in Au nanoparticles. The Faraday effect is the rotation of the polarization plane of light transmitted through a magnetized medium. Here the magnetization comes from an external applied static magnetic field. (b) The IFE is the induced magnetization of a medium (M_{ind}) during circularly polarized excitation (green line). The direction of induced magnetization depends on the helicity of the light. In this experiment, the optical rotation of a probe beam (purple line) indicates the existence of IFE. The rotation angle was then compared with the angle in (a), where the external applied magnetic field results into Faraday rotation. [Figure from: O. H.-C. Cheng, D. H. Son and M. Sheldon, 2020, Light-induced magnetism in plasmonic gold nanoparticles, *Nature Photonics*, Vol. 14 Issue 6 Pages 365-368]

Figure 1-15a depicts the Faraday rotation of the polarization plane of light transmitted through a magnetized medium, where the magnetization comes from an externally applied static magnetic field. In Figure 1-15b, the external applied magnetic field is replaced by RHCP or LHCP light. According to IFE, circularly polarized light also induces magnetization in Au nanoparticles. By comparing the rotation angle in Figure 1-15a and Figure 1-15b, Sheldon estimated the static magnetic field due to IFE. This light-induced magnetic moment is significant under typical ultrafast pulse excitation, with magnetization and demagnetization kinetics that are instantaneous within the subpicosecond time resolution of the study. This

research supported a mechanism of coherent transfer of angular momentum from the optical field to the electron gas and opened the door to all-optical subwavelength strategies for optical isolation that do not require externally applied magnetic fields.

These two theoretical and experimental studies built the link between plasmonic nanostructures and IFE, paving the way for plasmonic-enhanced IFE and light-induced stationary magnetic fields.

1.3 Research significance

The properties of magnetic fields vary widely across different scales, spanning orders of magnitude depending on their origin: from millennia-scale events like the reversal of Earth's magnetic poles to femtosecond timeframes associated with spin exchange interactions; from the tesla range used in hard drive writing heads to the few femtotesla found in neural activity; and from solar magnetic fields extending tens of thousands of kilometers to atomic scales of subnanometers.

In my PhD project, I focused on exploring magnetic effects during light-matter interactions at the nanoscale. Through the use of specially designed nanoantennas, I achieved precise manipulation of the Inverse Faraday Effect (IFE), realizing:

1) An intense, confined, and ultrafast magnetic fields;
2) IFE through linearly polarized incident light;
3) Neel-type skyrmion constructed by stationary B field.

However, such a confined, intense, and ultrafast field could have profound impacts on magnetism research and related technologies. Phenomena such as spin precession, spin−orbit coupling, and exchange interactions are rooted in the femtosecond time scale. The ability to probe and manipulate these processes and their transient mechanisms using ultrashort pulses of magnetic fields would advance various areas of magnetism research. Applications range from Zeeman splitting, magnetic trapping, and magnetic skyrmions to magneto-plasmonics, ultrafast magnetic modulation, and magnetic circular dichroism. Moreover, it extends to spin control, spin currents, and spin waves, offering new avenues for exploration and technological development.

As for the linearly excited IFE, our work has demonstrated a new possibility in magneto-optics by showcasing the excitation of the IFE through linear polarization. Traditionally, this magneto-optical phenomenon was thought to only occur with circular or elliptical polarization. The results presented here not only introduce a novel physical effect but also offer promising prospects for manipulating and controlling magnetic processes on ultrafast time scales.

Linearly excited IFE enables the ultrafast manipulation of magnetic domains within the near field by simply adjusting the incident polarization angle on the plasmonic nanoantenna. This all-optical interaction facilitates rapid nanomanipulation of magnetic phenomena such as domain reversal, skyrmions, circular dichroism, as well as control over spin, its currents, and waves. These capabilities hold significant potential for advancing technologies related to spintronics, magneto-optics, and ultrafast magnetism research.

For generation of Neel-type skyrmion through stationary B field, this research illustrates the generation of Neel-type skyrmions, showcasing a case study of magnetic field orientation reversal from the center to the periphery of a plasmonic structure. This spatial vector distribution aligns closely with the anticipated symmetry characteristics of skyrmions. The findings represent a significant advancement in generating and manipulating nanoscale magnetic field distributions using the inverse IFE. This breakthrough opens new avenues for implementing skyrmionic topological structures directly in magnetic materials through an all-optical approach, potentially operating at ultrafast timescales. Consequently, this work holds promise for applications across various fields, including the manipulation of magnetic processes, ultrafast magnetic modulation, magnetic trapping, spin currents, and spin precession. These advancements are expected to contribute directly to applications such as ultrafast data writing and processing.

In summary, I studied multiple aspects of the magnetic effects of light in my PhD project. The magnetic effect of light still represents a rich area of research with interdisciplinary implications spanning physics, materials science, optics, electronics, and biomedicine. Its applications range from information technology and telecommunications to healthcare and fundamental scientific exploration. My researches might find applications in many areas, including magneto-optical materials and devices, optical data storage, biomedical applications, spintronics and quantum computing, fundamental research in electromagnetism, advanced materials research, etc.

1.4 Research content

The research content includes plasmonic-enhanced IFE and a stationary DC current based on R. Hertel's theory. The light-induced magnetization, as well as the stationary magnetic field originating from this DC current, are numerically investigated in Lumerical FDTD. By designing different kinds of plasmonic nanoantennas, multiple light-induced stationary magnetic fields are realized.

1.4.1 Ultrafast, strong stationary magnetic field

In this research, we designed a bull-eye nanoantenna capable of efficiently confining electromagnetic energy in the near field and creating an ultra-strong stationary magnetic field (Figure 1-16). The bull-eye nanoantenna is composed of 10 concentric golden rings, which localize energy in the central area efficiently through plasmonic resonance. Each inner and outer radius of the rings is specially designed using a genetic algorithm (GA). This genetic algorithm simulates the evolution and reproduction of natural populations. The inner and outer radii of these concentric grooves in the bull-eye nanoantenna are identified as individual features, which can be mutated and altered during the evolution in GA. According to the optimization direction we set, the entire group, comprising all possible geometric dimensions, tends to produce the nanostructure with the strongest stationary magnetic field. At the end of the evolution, we obtained the bull-eye nanostructure with the strongest stationary magnetic field among the total group.

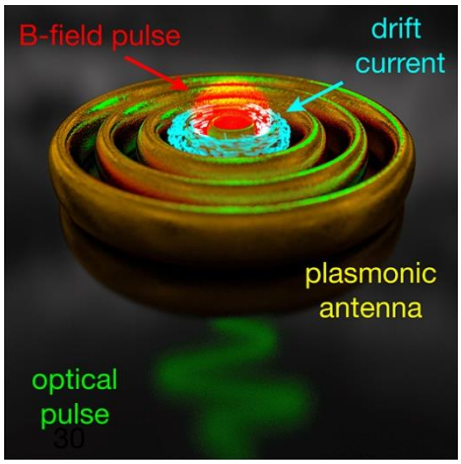

Figure 1-16. Schematic description of bull-eye nanoantenna. The bull-eye nanoantenna consists of 10 concentric gold rings on glass substrate. The nanostructure is excited by circularly polarized light from the substrate side. The interaction between circularly polarized light and the multilayer concentric circle structure results into plasmonic resonance, leading to confined electromagnetic energy in the central area. Hence, an ultrafast, strong stationary magnetic field is created.

Then, we analyzed the optimized bull-eye nanostructure and explained the physical origin of these strong magnetic fields. Additionally, we studied the time domain response of this stationary magnetic field. Numerical calculations verified that the generation of this ultra-strong stationary magnetic field is ultrafast, occurring within a few femtoseconds. As a result, our bull-eye plasmonic nanoantenna efficiently generated an ultrafast, confined, and strong

stationary magnetic field.

1.4.2 Stationary magnetic field through linearly polarized incident light

It is generally believed that linear polarization does not allow IFE, resulting in no DC magnetization or stationary magnetic field. However, in this project, we demonstrated a stationary magnetic field generated in a gold nanorod through linearly polarized incident light. In many nano-optical studies, nanoantennas show multiple abilities to manipulate electromagnetic fields in the near field. Here, we take advantage of the polarization conversion property of the plasmonic nanorod. Under specific light conditions, a gold nanorod can generate a local circularly polarized field through linearly polarized incident light, making it possible to create circulation drift current and a stationary magnetic field with linearly polarized light.

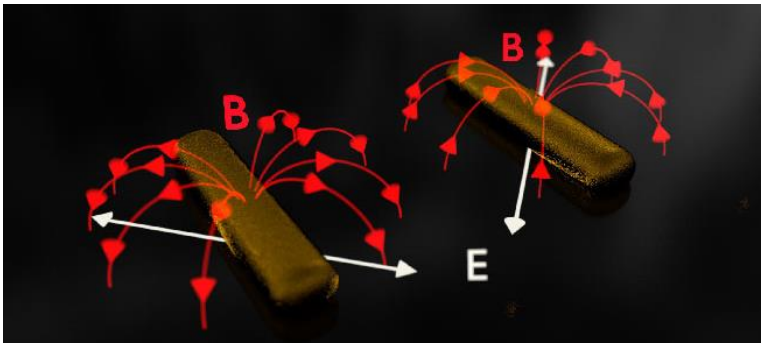

Figure 1-17. Schematic of plasmonic nanorod and light-induced stationary B field by linearly polarized incident light.

In our project, the nanorod possesses a high aspect ratio that enables two fundamental resonant modes: one along the short side and the other along the long side. Each mode acts as an oscillating electric dipole (ED). When considering both the short side and long side modes together, two perpendicular EDs exist in space. Consequently, the electric fields generated by these EDs are not parallel to each other. Additionally, the EDs along the long side and short side are excited with different strengths due to their distinct geometric dimensions, leading to a phase difference between them. This results in the creation of non-parallel, out-of-phase electric fields in the near field, which enables the existence of local elliptical polarization. Notably, elliptical polarization is a critical requirement for IFE. Indeed, the strengths of the two modes are manually adjusted by varying the polarization angle of the incident light. Since both modes contribute to the total electric field, adjusting their strengths also affects the total

electric field and local elliptical polarization. At a specific polarization angle, we were able to induce a circulating DC current around the nanorod based on R. Hertel's theory. Consequently, this led to the generation of a stationary magnetic field using linearly polarized incident light.

1.4.3 Skyrmionic topology out of Inverse Faraday Effect

In this research, we aimed to create a Neel-type skyrmion through a light-induced stationary magnetic field. Skyrmions are topologically stable quasiparticles observed in various fields such as quantum physics, solid-state physics, and magnetic materials. They can be constructed using unit vector fields of optical electric fields (E), magnetic fields (H), spin density vectors, and so forth. Figure 1-18 illustrates two fundamental 2D skyrmions studied in magnetism research. Notably, the Neel-type skyrmion exhibits a radial vector distribution, similar to the distribution of the stationary magnetic field generated by annular direct current (DC). Therefore, in this project, we manipulated the distribution of the stationary magnetic field generated by DC current in a plasmonic golden nanoring to construct a Neel-type skyrmion.

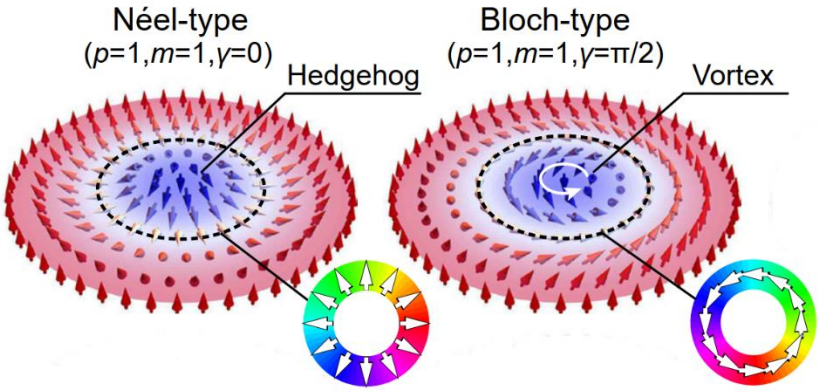

Figure 1-18. Neel-type and Bloch-type skyrmion. [Figure from: Y. Shen, Q. Zhang, P. Shi, L. Du, A. V. Zayats and X. Yuan, 2022, Topological quasiparticles of light: optical skyrmions and beyond]

We selected the nanoring structure due to its two fundamental resonant modes resulting from the coupling between the disk and cavity, known as the bonding mode and anti-bonding mode (also referred to as the bright mode and dark mode), respectively. Each mode can be described as a superposition of two concentric, parallel electric dipoles (EDs). The bonding mode consists of in-phase EDs, whereas the anti-bonding mode consists of out-of-phase EDs. This difference in configuration leads to distinct near-field electric field distributions and local

polarization states.

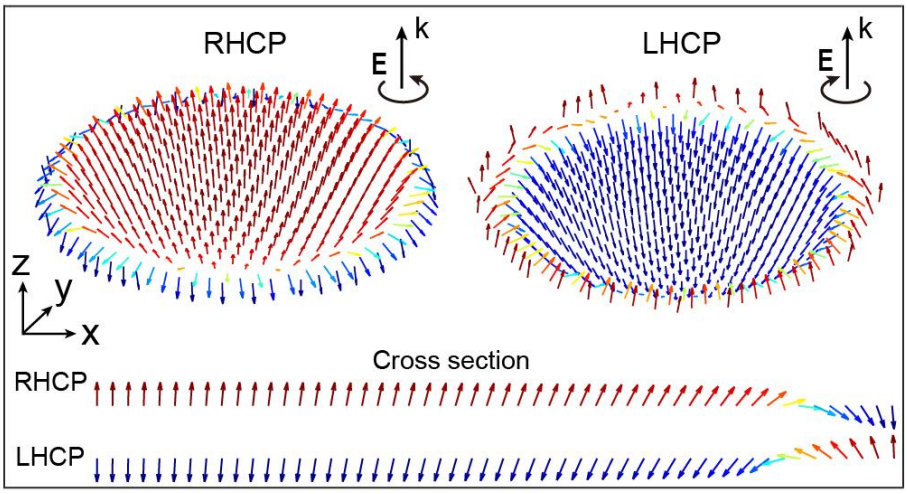

Figure 1-19. Neel-type skyrmion constructed by unit vector of light-induced stationary magnetic field at RHCP and LHCP.

In our research, the direction of the dc current is directly linked to the local polarization state. Specifically, left-handed circularly polarized light (RHCP) and right-handed circularly polarized light (LHCP) induce opposite dc currents. We demonstrated that two counter-propagating dc currents can generate a magnetic field exhibiting a skyrmion-like spatial distribution. By exciting different modes of the nanoring, we controlled the local polarization state. Consequently, we observed parallel-propagating and counter-propagating dc currents in the nanoring for the bonding mode and anti-bonding mode, respectively. By adjusting the geometric dimensions, we tuned the skyrmion-like stationary magnetic field into a Neel-type skyrmion with a defined skyrmion number. Finally, exciting the anti-bonding mode of the nanoring with RHCP and LHCP incident light separately, we successfully reversed the skyrmion number from +1 to -1, as displayed in Figure 1-19.

In conclusion, our theoretical investigation demonstrates that manipulating the polarization of light in the near-field of a plasmonic nanostructure allows for the generation of a vectorial magnetic field distribution that exhibits the topology of a Neel-type skyrmion with a skyrmion number of ±1.

REFERENCE

[1] G.D. Scott, A study of the Lycurgus Cup, Journal of Glass Studies, 37 (1995) 51-64.

[2] R. Feynman, There's plenty of room at the bottom, Resonance: Journal of Science Education, 16 (2011).

[3] E. Drexler, Engines of creation: The coming era of nanotechnology, Anchor1987.

[4] L. Novotny, B. Hecht, Principles of nano-optics, Cambridge university press2012.

[5] T.W. Ebbesen, H.J. Lezec, H. Ghaemi, T. Thio, P.A. Wolff, Extraordinary optical transmission through sub-wavelength hole arrays, nature, 391 (1998) 667-669.

[6] Y. Poujet, J. Salvi, F.I. Baida, 90% Extraordinary optical transmission in the visible range through annular aperture metallic arrays, Optics letters, 32 (2007) 2942-2944.

[7] J. Hao, L. Zhou, M. Qiu, Nearly total absorption of light and heat generation by plasmonic metamaterials, Physical Review B—Condensed Matter and Materials Physics, 83 (2011) 165107.

[8] W. Li, J. Valentine, Metamaterial perfect absorber based hot electron photodetection, Nano letters, 14 (2014) 3510-3514.

[9] S.A. Maier, Plasmonics: fundamentals and applications, Springer2007.

[10] H. Raether, The dispersion relation of surface plasmons on rough surfaces; a comment on roughness data, Surface Science, 125 (1983) 624-634.

[11] Y.H. Fu, A.I. Kuznetsov, A.E. Miroshnichenko, Y.F. Yu, B. Luk'yanchuk, Directional visible light scattering by silicon nanoparticles, Nature communications, 4 (2013) 1527.

[12] J.-M. Geffrin, B. García-Cámara, R. Gómez-Medina, P. Albella, L. Froufe-Pérez, C. Eyraud, A. Litman, R. Vaillon, F. González, M. Nieto-Vesperinas, Magnetic and electric coherence in forward-and back-scattered electromagnetic waves by a single dielectric subwavelength sphere, Nature communications, 3 (2012) 1171.

[13] X. Chen, Y. Chen, M. Yan, M. Qiu, Nanosecond photothermal effects in plasmonic nanostructures, ACS nano, 6 (2012) 2550-2557.

[14] Y. Li, X. Yang, Y. Yang, B. Wang, X. Li, R. Salas-Montiel, Optical nanoheating of resonant silicon nanoparticles, Optics Express, 27 (2019) 30971-30978.

[15] D. Jaque, L.M. Maestro, B. del Rosal, P. Haro-Gonzalez, A. Benayas, J. Plaza, E.M. Rodríguez, J.G. Solé, Nanoparticles for photothermal therapies, nanoscale, 6 (2014) 9494-9530.

[16] R. Hertel, Theory of the inverse Faraday effect in metals, Journal of magnetism and magnetic materials, 303 (2006) L1-L4.

[17] J. Van der Ziel, P.S. Pershan, L. Malmstrom, Optically-induced magnetization resulting from the inverse Faraday effect, Physical review letters, 15 (1965) 190.

[18] J. Deschamps, M. Fitaire, M. Lagoutte, Inverse Faraday effect in a plasma, Physical Review Letters, 25 (1970) 1330.

[19] A. Nadarajah, M.T. Sheldon, Optoelectronic phenomena in gold metal nanostructures due to the inverse Faraday effect, Optics Express, 25 (2017) 12753-12764.

[20] O.H.-C. Cheng, D.H. Son, M. Sheldon, Light-induced magnetism in plasmonic gold

nanoparticles, Nature Photonics, 14 (2020) 365-368.

[21] S.A. Ramakrishna, Physics of negative refractive index materials, Reports on progress in physics, 68 (2005) 449.

[22] D. Schurig, J. Mock, D. Smith, Electric-field-coupled resonators for negative permittivity metamaterials, Applied physics letters, 88 (2006).

[23] E. Ozbay, K. Guven, K. Aydin, Metamaterials with negative permeability and negative refractive index: experiments and simulations, Journal of Optics A: Pure and Applied Optics, 9 (2007) S301.

[24] B. Huang, H. Babcock, X. Zhuang, Breaking the diffraction barrier: super-resolution imaging of cells, Cell, 143 (2010) 1047-1058.

[25] K.D. Weltmann, J.F. Kolb, M. Holub, D. Uhrlandt, M. Šimek, K. Ostrikov, S. Hamaguchi, U. Cvelbar, M. Černák, B. Locke, The future for plasma science and technology, Plasma Processes and Polymers, 16 (2019) 1800118.

[26] W. Fisher, S. Rand, Optically-induced charge separation and terahertz emission in unbiased dielectrics, Journal of Applied Physics, 109 (2011).

[27] M. Fiebig, Revival of the magnetoelectric effect, Journal of physics D: applied physics, 38 (2005) R123.

[28] J. García-Merino, C. Martínez-González, C.T. San Miguel, M. Trejo-Valdez, H. Martínez-Gutiérrez, C. Torres-Torres, Magneto-conductivity and magnetically-controlled nonlinear optical transmittance in multi-wall carbon nanotubes, Optics Express, 24 (2016) 19552-19557.

[29] M. Mansuripur, The faraday effect, Optics and Photonics News, 10 (1999) 32-36.

[30] K. Shinagawa, Faraday and Kerr effects in ferromagnets, Magneto-optics, Springer2000, pp. 137-177.

[31] A.J. Kox, The discovery of the electron: II. The Zeeman effect, European journal of physics, 18 (1997) 139.

[32] C. Rizzo, A. Rizzo, D.M. Bishop, The Cotton-Mouton effect in gases: experiment and theory, International Reviews in Physical Chemistry, 16 (1997) 81-111.

[33] S.-i. Ohkoshi, H. Tokoro, Photomagnetism in cyano-bridged bimetal assemblies, Accounts of chemical research, 45 (2012) 1749-1758.

[34] O.H.-C. Cheng, B. Zhao, Z. Brawley, D.H. Son, M.T. Sheldon, Active tuning of plasmon damping via light induced magnetism, Nano Letters, 22 (2022) 5120-5126.

[35] P. Pershan, Nonlinear optical properties of solids: energy considerations, Physical Review, 130 (1963) 919.

[36] X. Yang, Y. Mou, B. Gallas, A. Maitre, L. Coolen, M. Mivelle, Tesla-range femtosecond pulses of stationary magnetic field, optically generated at the nanoscale in a plasmonic antenna, ACS nano, 16 (2021) 386-393.

[37] R. Wood, On a remarkable case of uneven distribution of light in a diffraction spectrum, Proceedings of the Physical Society of London, 18 (1902) 269-275.

[38] L. Rayleigh, On the dynamical theory of gratings, Proceedings of the Royal Society of London. Series A, Containing Papers of a Mathematical and Physical Character, 79 (1907) 399-416.

[39] U. Fano, The theory of anomalous diffraction gratings and of quasi-stationary waves on metallic surfaces (Sommerfeld's waves), JOSA, 31 (1941) 213-222.

[40] R.H. Ritchie, Plasma losses by fast electrons in thin films, Physical review, 106 (1957) 874.

[41] E. Stern, R. Ferrell, Surface plasma oscillations of a degenerate electron gas, Physical Review, 120 (1960) 130.

[42] A.J. McAlister, E. Stern, Plasma resonance absorption in thin metal films, Physical Review, 132 (1963) 1599.

[43] A. Otto, Excitation of nonradiative surface plasma waves in silver by the method of frustrated total reflection, Zeitschrift für Physik A Hadrons and nuclei, 216 (1968) 398-410.

[44] E. Kretschmann, Die bestimmung optischer konstanten von metallen durch anregung von oberflächenplasmaschwingungen, Zeitschrift fur physik, 241 (1971) 313-324.

[45] E. Hutter, J.H. Fendler, Exploitation of localized surface plasmon resonance, Advanced materials, 16 (2004) 1685-1706.

[46] K.M. Mayer, J.H. Hafner, Localized surface plasmon resonance sensors, Chemical reviews, 111 (2011) 3828-3857.

[47] Y. Pomeau, D. Quemada, Effet Faraday inverse dans un plasma, COMPTES RENDUS HEBDOMADAIRES DES SEANCES DE L ACADEMIE DES SCIENCES SERIE B, 264 (1967) 517-+.

[48] H.-L. Zhang, Y.-Z. Wang, X.-J. Chen, A simple explanation for the inverse Faraday effect in metals, Journal of magnetism and magnetic materials, 321 (2009) L73-L74.

2 Theory

When a free electron in space interacts with circularly polarized light, its trajectory forms a solenoid-like path. The magnetization of the medium due to the IFE arises from these microscopic solenoidal currents[1, 2]. Additionally, if optical field gradients exist within the metal, a second-order perturbation analysis of electron trajectories reveals the emergence of an additional macroscopic direct current (dc current)[3]. This current, known as a drift current, contributes to the overall magnetization effect. These physical phenomena are theoretically described by the electrodynamic motion of a free electron gas under the Drude approximation. Once the drift current is established, the light-induced stationary magnetic field can be determined using the Biot-Savart law. This law quantitatively relates the current distribution to the magnetic field it generates, providing a comprehensive description of the resulting magnetic field from the induced currents.

2.1 Inverse Faraday effect in metals

The trajectory of a single electron driven by a circularly polarized light beam in free space typically forms a closed circle, analogous to a ring current that results in a dc magnetization. This phenomenon can be succinctly explained using a simple electrodynamic model[1].

In this model, we simplify by neglecting the complex interactions among electrons and instead focus on the response of a single electron to an external electric field. The motion of a single electron driven by an electric field is governed by Newton's laws:

$$m\frac{d^2\mathbf{r}}{dt^2} = e\mathbf{E} \tag{2-1}$$

where

m	Mass of electron
t	Time variable
$\mathbf{r}$	Displacement of electron
e	Elementary charge (e < 0)
$\mathbf{E}$	External electric field with time factor exp(-$j\omega t$)
ω	Angular frequency of light

In our study, the external electric field is represented by incident light applied to the nanoantenna. In this scenario, both the electric field and the electron displacement are time-harmonic fields. They share the same oscillation frequency (ω) as the incident light. Therefore, the time derivative can be simply replaced by

$$\frac{d\mathbf{r}}{dt} = (-j\omega)\mathbf{r} \tag{2-2}$$

Therefore, Eq. (2-1) becomes

$$-m\omega^2\mathbf{r} = e\mathbf{E} \tag{2-3}$$

which indicates that the displacement of the electron is proportional to the external electric field. In the case of circularly polarized incident light, the electron's displacement will describe a spinning motion in the plane. Moreover, the trajectory of the electron forms a closed circle, with the radius of this circle being proportional to the amplitude of the light component.

$$r_0 = -\frac{eE_0}{m\omega^2} \tag{2-4}$$

where

r_0	radius of electron's circular path
E_0	Amplitude of the electric field

Therefore, the area of this closed circle is proportional to the square of the radius (r) in Eq. (2-4)

$$A = \pi r_0^2 = \pi \frac{e^2 E_0^2}{m^2 \omega^4} \tag{2-5}$$

On the other hand, the circulating electron could be equivalent to an annular DC current I, described by

$$I = \pm\frac{e\omega}{2\pi} \tag{2-6}$$

where (±) depends on handedness of circularly polarized light. The ring current (I) of area (A) thus generates a magnetic moment of

$$\mu = AI = \frac{e^3 E_0^2}{2m^2\omega^3} \tag{2-7}$$

Eq. (2-7) describes magnetization induced by single electron. Considering all the free electrons

in material, we have

$$\mathbf{M}^{(\pm)} = n\left(\pm\mu\right)\hat{\mathbf{e}}_{\mathbf{k}} = \pm\frac{ne^3E_0^2}{2m^2\omega^3}\hat{\mathbf{e}}_{\mathbf{k}} \tag{2-8}$$

where

n	Volume density of electrons
$\hat{\mathbf{e}}_{\mathbf{k}}$	Unit vector of wavenumber **k**, describing light propagating direction

This simple explanation based on single electron motion is identical to that obtained by R. Hertel, which effectively describes the IFE in metals[3, 4].

2.2 Light-induced drift current

Another phenomenon predicted by R. Hertel that accompanies IFE is a stationary dc current, also known as drift current. When a metallic material is exposed to a circularly polarized high-frequency electromagnetic wave, the induced electric current considering all free electrons can be described by a general definition

$$\mathbf{J} = en\mathbf{v} \tag{2-9}$$

where

J	Current density vector
v	Velocity of electron

For free electrons in metal driven by electromagnetic field, both electron density (n) and electron velocity (**v**) are function of electromagnetic field with time factor exp(-$j\omega t$), leading to a dc component in electric current **J**. In electrodynamics theory, electron velocity (**v**) and electron density (n) could be analytically described by Drude model and continuity equation for charge conservation, respectively.

2.2.1 Drude model

Since conduction electrons in metals are treated as free, the Drude model extends from the single Lorentz oscillator model where the restoring force and resonance frequency are zero[5, 6]. Therefore, the motion of electrons can be described by the equation

$$m \cdot \frac{d\mathbf{v}}{dt} + m \cdot \Gamma_d \cdot \mathbf{v} = e\mathbf{E} \tag{2-10}$$

where

Γ_d Friction force

In case of time-harmonic field, we have

$$m \cdot (-j\omega)\mathbf{v} + m \cdot \Gamma_d \cdot \mathbf{v} = e\mathbf{E} \tag{2-11}$$

Hence

$$\mathbf{v} = \frac{e}{m} \frac{\mathbf{E}}{(-j\omega + \Gamma_d)} \tag{2-12}$$

Therefore, the conduction current density corresponding to the movement of electrons with volume density (n) is

$$\mathbf{J_{cd}} = en\mathbf{v} = \frac{ne^2}{m(-j\omega + \Gamma_d)}\mathbf{E} \tag{2-13}$$

Defining the complex conductivity (σ) as

$$\sigma(\omega) = \frac{ne^2}{m(-j\omega + \Gamma_d)} \tag{2-14}$$

We have

$$\mathbf{J_{cd}} = \sigma\mathbf{E} \tag{2-15}$$

Therefore, in Drude approximation, conduction current ($\mathbf{J_{cd}}$) is proportional to electric field ($\mathbf{E}$). Then electron velocity ($\mathbf{v}$) Eq. (2-12) could be simply expressed by electric field ($\mathbf{E}$).

$$\mathbf{v} = \frac{\sigma}{en}\mathbf{E} \tag{2-16}$$

The velocity ($\mathbf{v}$) here will appear in further calculation of IFE.

2.2.2 Continuity equation of free electrons

A continuity equation describes the transport or conservation of a quantity. In classical electrodynamics, the continuity equation describes the conservation law of free electrons, which is

$$\frac{\partial n}{\partial t}+\nabla\cdot\left(n\mathbf{v}\right)=0 \tag{2-17}$$

By adding elementary charge (e) into both sides we have

$$e\frac{\partial n}{\partial t}+\nabla\cdot\mathbf{J}_{\mathbf{cd}}=0 \tag{2-18}$$

Therefore, there is a fluctuation of free electron density in time that is caused by the flow of conduction current ($\mathbf{J}_{\mathbf{cd}}$) in space. Here we separate electron density into time-averaged part <n> and fluctuating part (δn)

$$n=\langle n\rangle+\delta n \tag{2-19}$$

Since in electron density (n) only fluctuating part (δn) is function of time

$$e\frac{\partial\left(\delta n\right)}{\partial t}+\nabla\cdot\mathbf{J}_{\mathbf{cd}}=0 \tag{2-20}$$

Again, in case of time-harmonic field Eq. (2-20) becomes

$$e\left(-j\omega\right)\delta n+\nabla\cdot\mathbf{J}_{\mathbf{cd}}=0 \tag{2-21}$$

Hence, we have

$$\delta n=\frac{1}{j\omega e}\nabla\cdot\mathbf{J}_{\mathbf{cd}} \tag{2-22}$$

Same as electron velocity from Drude model, this fluctuating part of charge density (δn) play a role in IFE theory.

2.2.3 Drift current

Here we recall electric current in metal induced by high-frequency electromagnetic wave which described by Eq. (2-9). Considering both time-averaged part <n> and fluctuating part (δn) of electron density in Eq. (2-9), we have

$$\mathbf{J}=e\left(\langle n\rangle+\delta n\right)\mathbf{v} \tag{2-23}$$

The first part describes the conduction currents ($\mathbf{J}_{\mathbf{cd}}$), which dominates in $\mathbf{J}$. Therefore, the velocity of electron is simply approximated by Eq. (2-16) as

$$\mathbf{v}=\frac{\sigma}{e\langle n\rangle}\mathbf{E} \tag{2-24}$$

Then by replacing (δn) in Eq. (2-23) with the expression from continuity equation in Eq. (2-22), we have the second part of **J**

$$e(\delta n)\mathbf{v} = e\left(\frac{1}{j\omega e}\nabla\cdot\mathbf{J}_{\mathbf{cd}}\right)\mathbf{v} = e\left(\frac{1}{j\omega e}\nabla\cdot\mathbf{J}_{\mathbf{cd}}\right)\left(\frac{\sigma}{e\langle n\rangle}\mathbf{E}\right) \tag{2-25}$$

To be noted that both ($\mathbf{J}_{\mathbf{cd}}$) and (**E**) are function of time with the same factor exp(-$j\omega t$), which results into a time irrelevant component[3]

$$\begin{aligned} e\langle\delta n\cdot\mathbf{v}\rangle &= \frac{e}{4}\left(\delta n\cdot\mathbf{v}^{*}+\delta n^{*}\cdot\mathbf{v}\right) \\ &= -\frac{j}{4e\langle n\rangle\omega}\left[\mathbf{J}_{\mathbf{cd}}{}^{*}\left(\nabla\cdot\mathbf{J}_{\mathbf{cd}}\right)-c.c.\right] \end{aligned} \tag{2-26}$$

$$where \quad \mathbf{J}_{\mathbf{cd}} = \sigma\mathbf{E}$$

This time irrelevant dc current is what we called drift current, noted as $\mathbf{J}_{\mathbf{d}} = e\langle\delta n\mathbf{v}\rangle$. By a mathematical transformation for arbitrary vector **A**, **B**

$$\nabla\times(\mathbf{A}\times\mathbf{B}) = (\mathbf{B}\cdot\nabla)\mathbf{A}-\mathbf{B}(\nabla\cdot\mathbf{A})+\mathbf{A}(\nabla\cdot\mathbf{B})-(\mathbf{A}\cdot\nabla)\mathbf{B} \tag{2-27}$$

Drift current in Eq. (2-26) could be separated into two parts.

$$\mathbf{J}_{\mathbf{d}} = -\frac{j}{4e\langle n\rangle\omega}\nabla\times\left(\sigma^{*}\mathbf{E}^{*}\times\sigma\mathbf{E}\right)+\frac{1}{4e\langle n\rangle\omega}\left[j\left(\sigma^{*}\mathbf{E}^{*}\cdot\nabla\right)\sigma\mathbf{E}+c.c.\right] \tag{2-28}$$

Indeed, the two contributions represent magnetization current and the stationary currents induced by ponderomotive force, respectively. Therefore, drift current could be simple noted as

$$\mathbf{J}_{\mathbf{d}} = \nabla\times\mathbf{M}+\boldsymbol{\Gamma} \tag{2-29}$$

where

M	Magnetization
Γ	Stationary currents induced by ponderomotive force

The magnetization and ponderomotive force induced current are expressed as

$$\mathbf{M} = -\frac{j}{4e\langle n\rangle\omega}\left(\sigma^{*}\mathbf{E}^{*}\times\sigma\mathbf{E}\right)$$
$$\boldsymbol{\Gamma} = \frac{1}{4e\langle n\rangle\omega}\left[\, j\left(\sigma^{*}\mathbf{E}^{*}\cdot\nabla\right)\sigma\mathbf{E} + c.c.\right] \tag{2-30}$$

It can be shown that the magnetization described in Eq. (2-30) is equivalent to the magnetization given in Eq. (2-8), both originating from the motion of a single electron under circularly polarized incident light. Therefore, the magnetization current described by the drift current expression represents the circular motion of electrons induced by circularly polarized incident light. This provides a microscopic explanation for the IFE.

On the other hand, the stationary current related to ponderomotive force primarily arises from optical field gradients. In certain scenarios, a circulating ponderomotive force induces a stationary current at the microscopic level, which also contributes to the generation of a stationary magnetic field.

2.3 Light-induced stationary magnetic field

In metallic media, the magnetization induced by circularly polarized light results in a stationary magnetic field that has contributions from both conduction current and magnetization current[2]. The drift current, which arises from ponderomotive forces due to optical field gradients, represents conduction currents describing the movement of electrons. On the other hand, magnetization current describes the circular motion of bound electrons induced by circularly polarized light.

When calculating the light-induced stationary magnetic field due to the drift current, Biot-Savart's law is applied directly to determine the magnetic field generated by the current distribution.

$$\mathbf{B}(\mathbf{r}) = \frac{\mu_0}{4\pi}\iiint_V \frac{\mathbf{J_d}\times\mathbf{r}'}{\left|\mathbf{r}'\right|^3}\,dV \tag{2-31}$$

where

$\mathbf{B}$	Stationary magnetic field at $\mathbf{r}$
μ_0	Vacuum permeability
$\mathbf{J_d}$	Drift current
$\mathbf{r}'$	Source position where $\mathbf{J_d}$ located as

In plasmonic nanoantennas, the contribution of magnetization to the stationary magnetic field is described by the magnetization current, which is the first term of the drift current in Eq. (2-29).

The stationary magnetic field generated by the drift current in plasmonic nanoantennas can be significantly enhanced under specific conditions, benefiting from two main aspects:

1) Enhanced electric field in plasmonic resonant modes.

In plasma resonant modes, electromagnetic energy is highly confined in the near field, resulting in a significantly enhanced electric field. Due to the small geometric dimensions typical of nanoscale structures, large optical field gradients can be created, leading to a strong drift current. This enhanced electric field contributes to a strong stationary magnetic field.

2) Nanoscale distribution of drift currents.

The induced drift currents are distributed within the nanoantenna, which itself is on the nanoscale. The stationary magnetic field benefits from this short distance, as indicated by the denominator of Eq. (2-31), where the stationary magnetic field is inversely proportional to the square of the distance. Therefore, drift currents distributed throughout the nanoantenna can generate a strong stationary magnetic field in the near field.

2.4 Direction dependence of drift current

In some situations, we also care about the direction of drift current, by manipulation its direction we could further control the induced stationary B field through Biot-Savart law. According to our study, the direction of drift current is related to the polarization state of local electric field.

If we neglect the constant and focus on the direction of drift current in Eq. (2-26), the expression of drift current is simplified as

$$\mathrm{Im}\left[(\nabla\cdot\mathbf{E})\mathbf{E}^{*}\right] \tag{2-28}$$

Then we represent complex E field in amplitude and phase.

$$\tilde{E}=\left|\tilde{E}\right|e^{j\phi} \tag{2-29}$$

where

$\tilde{E}$ Complex electric field

$\left\|\tilde{E}\right\|$	Amplitude of complex field
ϕ	Phase of complex field

We simply consider the electric field and corresponding drift current in 2D situation, XY plane for instance. According to Eq. (2-29), the electric vector in XY plane is represented as

$$\mathbf{E}=\begin{bmatrix}\tilde{E}_x\\ \tilde{E}_y\end{bmatrix}=\begin{bmatrix}E_x e^{j\phi_x}\\ E_y e^{j\phi_y}\end{bmatrix} \tag{2-30}$$

where

$E_{x,y}$	Amplitude of x or y component in **E** vector
$\phi_{x,y}$	Phase of x or y component in **E** vector

The divergence in Eq. (2-28) is

$$\nabla\cdot\mathbf{E}=\frac{\partial\left(E_x e^{j\phi_x}\right)}{\partial x}+\frac{\partial\left(E_y e^{j\phi_y}\right)}{\partial y} \tag{2-31}$$

Assume phase is slowly changing compared with the amplitude, then spatial derivative mainly depends on amplitude

$$\nabla\cdot\mathbf{E}=\frac{\partial E_x}{\partial x}e^{j\phi_x}+\frac{\partial E_y}{\partial y}e^{j\phi_y} \tag{2-32}$$

Insert Eq. (2-32) into Eq. (2-28), we have

$$\begin{aligned}\left(\nabla\cdot\mathbf{E}\right)\mathbf{E}^*&=\left(\frac{\partial E_x}{\partial x}e^{j\phi_x}+\frac{\partial E_y}{\partial y}e^{j\phi_y}\right)\cdot\begin{bmatrix}E_x e^{-j\phi_x}\\ E_y e^{-j\phi_y}\end{bmatrix}\\&=\begin{bmatrix}E_x\left(\frac{\partial E_x}{\partial x}+\frac{\partial E_y}{\partial y}e^{-j\phi_x+j\phi_y}\right)\\ E_y\left(\frac{\partial E_x}{\partial x}e^{j\phi_x-j\phi_y}+\frac{\partial E_y}{\partial y}\right)\end{bmatrix}\end{aligned} \tag{2-33}$$

Amplitude and its spatial derivative are real values, they have not contribution in Eq. (2-28) where only imaginary part makes senses. Therefore,

$$\mathrm{Im}\left[\left(\nabla\cdot\mathbf{E}\right)\mathbf{E}^*\right]=\mathrm{Im}\left(\begin{bmatrix}E_x\frac{\partial E_y}{\partial y}e^{-j\phi_x+j\phi_y}\\ E_y\frac{\partial E_x}{\partial x}e^{j\phi_x-j\phi_y}\end{bmatrix}\right)=\begin{bmatrix}E_x\frac{\partial E_y}{\partial y} & 0\\ 0 & E_y\frac{\partial E_x}{\partial x}\end{bmatrix}\begin{bmatrix}\mathrm{Im}\left(e^{-j\left(\phi_x-\phi_y\right)}\right)\\ \mathrm{Im}\left(e^{j\left(\phi_x-\phi_y\right)}\right)\end{bmatrix} \tag{2-34}$$

It is clearly shown in Eq. (2-34) that the phase difference between x and y component of E field plays a key role. From this expression, we can make several observations.

1) For linearly polarized light the phase different is zero, leading to a pure real number. Hence no drift current exists. To create drift current, local E field need to be elliptical or circular polarization.

2) Circular polarization is better than elliptical polarization, because the imaginary part reaches maximum when the phase different is 90°.

3) Left-handed and right-handed circular polarization result into opposite directions.

In our research the local polarization state is described by the concept spin density. Spin density is defined by cross product of electric field and its conjugation. Then we normalized this result by the amplitude E_0.

$$\mathbf{s} = \frac{1}{E_0^2} \mathrm{Im}\left(\mathbf{E}^* \times \mathbf{E}\right) \tag{2-35}$$

where

$\mathbf{s}$	Spin density
E_0	Amplitude of local electromagnetic wave
$\mathbf{E}$	Complex electric field
$\mathbf{E}^*$	Conjugation of complex electric field

Spin density describes the rotation of the electric field within its corresponding plane. For instance, the z-component of spin density signifies the rotation of the electric field in the XY plane. After normalization, spin density ranges between (-1) and (+1). A spin density of (-1) or (+1) indicates circular polarization, where (-1) denotes clockwise rotation within the plane, and (+1) denotes counterclockwise rotation. A spin density of 0 represents linearly polarized light, while values between (-1) and (+1) denote elliptically polarized light.

In summary, the direction of the drift current can be inferred from the distribution of spin density. This parameter will be crucial in the subsequent research.

2.5 Numerical simulation method

Based on theoretical frameworks, our research focuses on studying light-induced DC currents and their resultant stationary magnetic fields. These theoretical analyses rely on the intricate distribution of electric fields within space. In PhD research, we utilize the commercial software “Lumerical FDTD” to numerically simulate the optical electric field data.

2.5.1 Lumerical FDTD

Lumerical FDTD is based on the Finite-difference time-domain (FDTD) method[7-9], which is a numerical analysis technique used for modeling computational electrodynamics and obtaining approximate solutions to the associated system of differential equations. To solve Maxwell's equations, the method discretizes space into a set of parallelepiped, Cartesian-style grids, as illustrated in Figure 2-1. The FDTD method then solves these differential equations on these discrete spatial and temporal grids.

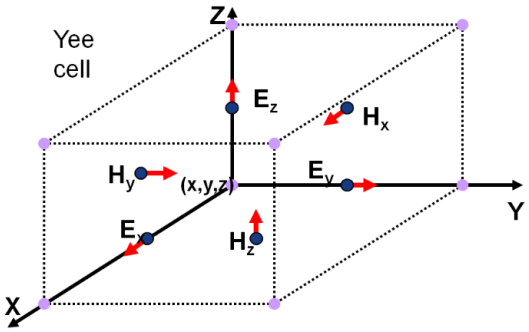

Figure 2-1. Discretized space in FDTD method, these rectangular, Cartesian style grids are also called Yee cell. The E and H field components to be solved are distributed on the grid. [Figure from Ansys Lumerical FDTD website, https://optics.ansys.com/hc/en-us/articles/360034914633-Finite-Difference-Time-Domain-FDTD-solver-introduction]

In the FDTD method, each field component is computed at slightly offset locations within the Yee cell grid. After solving Maxwell's equations, the results are automatically interpolated to the center of each grid point, allowing for the spatial distribution of electric (E) and magnetic (H) fields over time to be obtained in the time domain. Additionally, FDTD can leverage Fourier transforms on time-domain data to obtain frequency-domain solutions, enabling the calculation of a full range of frequency-domain results.

2.5.2 Simulation setup

In this section, we introduce the simulation setup used in our studies to ensure reproducibility. We designed multiple plasmonic nanoantennas, and below we describe the

setup for several key components of these simulation models:

1) Boundary conditions of FDTD region

The FDTD region specifies where the numerical simulation takes place. In our research, the bull-eye nanoantenna, nanorod, and nanoring are non-periodic structures. Therefore, we chose Perfectly Matched Layer (PML) absorbing boundary conditions to simulate the response of these nanoantennas located in infinite space.

2) Incident light

We utilized the "Total-Field Scattered-Field" (TFSF) source in our studies. This source is commonly used to study scattering from small particles illuminated by a plane wave. The TFSF source divides the computation region into two distinct parts.

a) Total field region. This region includes both the incident field and the scattered field.

b) Scattered field region. This region includes only the scattered field, with the incident light completely eliminated.

Although our research did not focus on the scattered field, we chose the TFSF source to effectively eliminate the incident field and avoid any potential reflections at the boundaries of the FDTD region, especially in cases where PML might not entirely eliminate reflected light.

3) Mesh setting

The mesh size directly impacts simulation accuracy and computational time. A smaller mesh provides better resolution of the optical field distribution but increases computational time. Given that the characteristic dimensions of our nanoantennas are approximately 10 – 20 nm, we set the mesh size covering the nanoantennas to 1 nm for optimal resolution. The mesh size for the remaining areas, primarily air or glass substrate, was set to default values to balance simulation accuracy and computational efficiency.

4) Material

All plasmonic nanoantennas in our studies consist of gold material deposited on a glass substrate. For the gold material, we selected "Au (Gold) - Johnson and Christy"[10] from the Lumerical FDTD database. The glass substrate material chosen was "SiO2 (Glass) - Palik" from the same database.

5) PML

PML layer is far from the object, the distance between PML layer and nanostructure is more than wavelength or two times of wavelength. The thickness of PML is set by default, since we have already chosen TFSF source to reduce the reflection at the boundary.

For other parameters in simulation models, we used default settings provided by Lumerical FDTD.

2.5.3 Simulation and calculation procedures

The Finite-Difference Time-Domain (FDTD) method efficiently calculates the electromagnetic response of complex structures such as our bull-eye nanoantenna. The spatial distributions of electric (E) and magnetic (H) fields obtained from Lumerical FDTD are crucial for further computations of drift current and light-induced stationary magnetic fields. Lumerical FDTD provides insights into light-matter interactions, aiding our understanding of complex electromagnetic phenomena.

In our research, Lumerical FDTD and Matlab are integrated. We developed scripts to call Lumerical FDTD and Matlab seamlessly, leveraging the strengths and advantages of both software platforms:

1) Powerful numerical simulation abilities from Lumerical FDTD

2) Powerful mathematical calculation ability from Matlab.

Matlab excels in matrix operations and numerical array calculations, ideal for processing the spatial E and H field distributions obtained from Lumerical FDTD simulations.

3) Official Matlab and Lumerical application programming interface (API)

The Matlab-Lumerical API enables control of Lumerical software directly from Matlab. This integration includes a high-speed data transmission channel, facilitating efficient computations of drift current and stationary magnetic fields.

4) Multiple mathematical tools in Matlab

Matlab provides extensive mathematical tools, enabling us to design optimization algorithms. For example, we can implement Genetic Algorithms (GA) in Matlab to automate the optimization of nanostructures through interaction with Lumerical FDTD.

The modeling, simulation, and calculation procedures are outlined below.

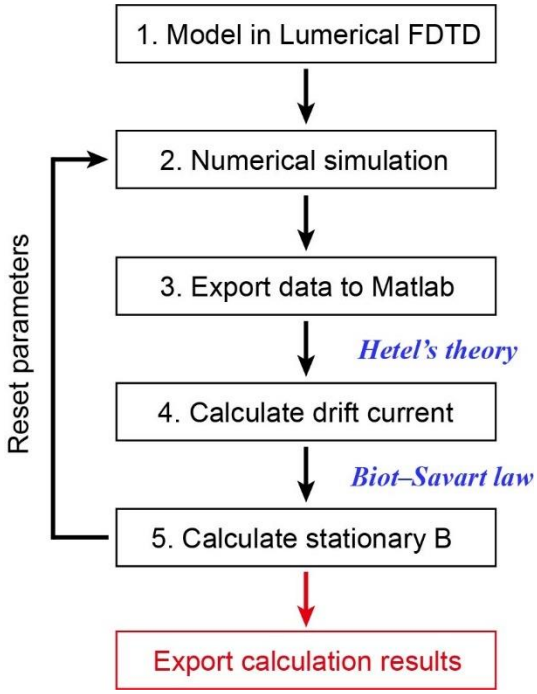

Figure 2-2. Flow chart of modeling, simulation and calculation. Modeling and simulation are completed in Lumerical FDTD. Calculation of drift current and stationary B field is carried out in Matlab. Communication between two software is realized by Matlab-Lumerical API.

The calculation of IFE includes five steps, as displayed in Figure 2-2.

1) Model the plasmonic nanoantenna in Lumerical FDTD software according to the scientific issue we are working on.

2) Run numerical simulation in Lumerical FDTD, so that we get original E and H field distribution.

3) Export spatial complex E and H data to Matlab. Optical E and H field distribution is stored and applied in further calculation.

4) Code in Matlab according to R.Hertel's theory. Then calculate spatial drift current distribution

5) Code in Matlab and calculate light-induced stationary magnetic field through Biot-Savart law.

Steps (1) to (5) outline the flow chart for a single simulation task, taking into account modeling, simulation, and calculation. For more complex tasks, such as optimizing the geometric parameters of a nanoantenna, this procedure from Step (1) to Step (5) iterates until the optimization process is completed. During this progression, Matlab adjusts parameters in the Lumerical model based on the specified optimization criteria. Additionally, algorithms can

be introduced to facilitate this process. In our bull-eye nanoantenna project, we have integrated a Genetic Algorithm (GA) within this framework.

2.6 Summary

This chapter introduces the theory of Inverse Faraday Effect (IFE), in particular the generation of light-induced dc current and the resulting stationary magnetic field. We illustrate the directional dependence of drift current through analytical derivation, establishing its correlation with the local polarization state. Additionally, we introduce spin density as a concept that succinctly characterizes the local light's polarization state. In future studies, we aim to predict the drift current's direction using spin density, a technique pivotal to our project outlined in Chapter 1. Finally, we detail our numerical simulation methodology, which involves modeling and simulation in Lumerical FDTD, followed by data analysis and calculation in Matlab. These two software tools are synergistically employed to tackle complex optimization tasks effectively.

Chapter 2 serves as a foundational numerical simulation platform. By incorporating various theoretical frameworks, we can delve into diverse scientific inquiries. Our approach involves modeling in Lumerical FDTD and conducting mathematical analyses in Matlab. The integration of Lumerical FDTD and Matlab through API allows us to employ multiple algorithms to achieve various research objectives, including but not limited to GA optimization.

REFERENCE

[1] H.-L. Zhang, Y.-Z. Wang, X.-J. Chen, A simple explanation for the inverse Faraday effect in metals, Journal of magnetism and magnetic materials, 321 (2009) L73-L74.

[2] A. Nadarajah, M.T. Sheldon, Optoelectronic phenomena in gold metal nanostructures due to the inverse Faraday effect, Optics Express, 25 (2017) 12753-12764.

[3] R. Hertel, Theory of the inverse Faraday effect in metals, Journal of magnetism and magnetic materials, 303 (2006) L1-L4.

[4] Y. Pomeau, D. Quemada, Effet Faraday inverse dans un plasma, COMPTES RENDUS HEBDOMADAIRES DES SEANCES DE L ACADEMIE DES SCIENCES SERIE B, 264 (1967) 517-+.

[5] S.A. Maier, Plasmonics: fundamentals and applications, Springer2007.

[6] W. Bade, Drude‐model calculation of dispersion forces. I. General theory, The Journal of Chemical Physics, 27 (1957) 1280-1284.

[7] K. Yee, Numerical solution of initial boundary value problems involving Maxwell's equations in isotropic media, IEEE Transactions on antennas and propagation, 14 (1966) 302-307.

[8] A. Taflove, Application of the finite-difference time-domain method to sinusoidal steady-state electromagnetic-penetration problems, IEEE Transactions on electromagnetic compatibility, DOI (1980) 191-202.

[9] A. Taflove, S.C. Hagness, M. Piket-May, Computational electromagnetics: the finite-difference time-domain method, The Electrical Engineering Handbook, 3 (2005) 15.

[10] P.B. Johnson, R.-W. Christy, Optical constants of the noble metals, Physical review B, 6 (1972) 4370.

3 Ultra-strong stationary magnetic field

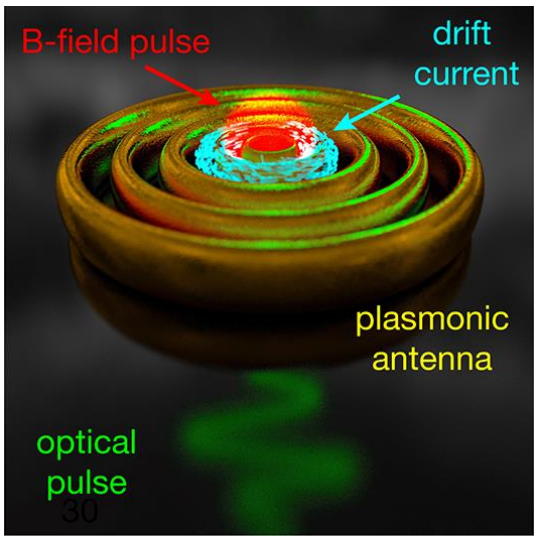

In this chapter, we demonstrate a method to create an ultra-strong, confined, and fast-responding stationary magnetic field through drift current in a bull-eye nanoantenna, as seen in the schematic above. According to our numerical calculations, the bull-eye nanoantenna is capable of generating a stationary magnetic field up to the tesla range in a few femtoseconds (fs) at an illumination power density of 10^{12} W/cm^2.

3.1 Bull-eye nanoantenna

In this research, we proposed a bull's-eye-shaped nanoantenna[1], as seen in Figure 3-1. The nanoantenna is composed of 10 concentric grooves made in a 40 nm thick gold layer placed on a glass substrate. Each groove has an independent inner and outer radius within the range we set. We chose the smallest width of the grooves to be 6 nm, while the largest is less than 30 nm. Similarly, the width of the metallic rings is chosen to be between 20 and 50 nm. We carefully selected these parameters to design a nanoantenna that, for instance, a helium focused ion beam (He-FIB) could fabricate in a cleanroom facility[2], both for reasons of etch resolution and processing time. The exact value of each inner and outer radius is selected by GA optimization[3], which will be described in detail below.

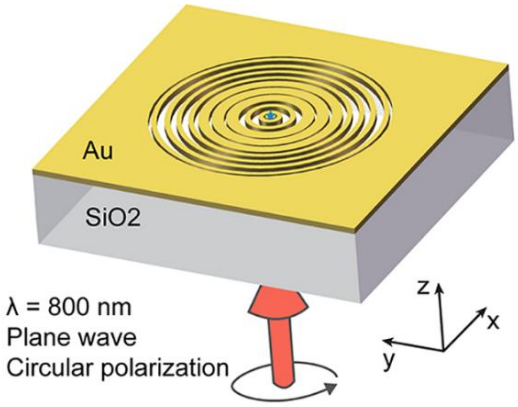

Figure 3-1. (a) Schematic of bull-eye-shaped nanoantenna. Nanoantenna is composed by 10 concentric grooves made in a 40 nm gold layer placed on a glass substrate. Then it is excited by a circularly polarized light with a power density of 10^{12} W/cm^2.

The nanoantenna is excited by a circularly polarized plane wave from the bottom (Figure 3-1). The incident light has a full-width at half-maximum power temporal duration of 5.3 fs with a power density of 10^{12} W/cm^2. This power density is chosen because the thin gold layer can withstand these peak powers for that duration[4, 5]. The wavelength is set to 800 nm, and the polarization is RHCP. Circular polarization is known to generate the inverse Faraday effect and drift current, and thus a stationary magnetic field.

Within these constraints, GA was allowed to optimize the diameters and sizes of the grooves independently of each other.

3.2 Genetic algorithm

The bull's-eye nanoantenna is constituted by 10 concentric grooves with independent inner and outer radii, producing 20 variables that need to be set in Lumerical FDTD. We developed a genetic algorithm to perform this multi-parameter optimization. The optimization problem is quantified into an iterative mathematical model.

3.2.1 Definition in GA model

GA simulates the evolution and reproduction of natural populations. The elements in GA are defined as follows:

a) Feature: A variable in GA, which is the inner and outer radius of each groove. Therefore, one nanoantenna has 20 features as variables.

b) Individual: One structure, considered as a single individual.

c) Generation: A set of individuals generated at the same time. In GA, we set one generation to have 40 individuals.

d) Group: A collection of all individuals in each generation. A group consists of many generations. GA stops when the improvement in each generation becomes stagnant.

The reproduction of new individuals is realized through “breeding” and “mutation” operations. These two operations mimic the behavior of genes in natural evolution. They are implemented numerically in the GA model, as explained below.

a) Breeding

Breeding is the exchange of features between different individuals in the same generation[6]. Figure 3-2 shows a schematic illustration of breeding. There are two individuals named A and B. The 20 variables of each individual are represented by a 2×10 matrix, noted as [A1, A2, A3, … A19, A20]. The first row represents the inner radii, and the second represents the outer radii, as seen in the top-left of Figure 3-2. Similarly, B is described by another matrix, as seen in the bottom-left of Figure 3-2.

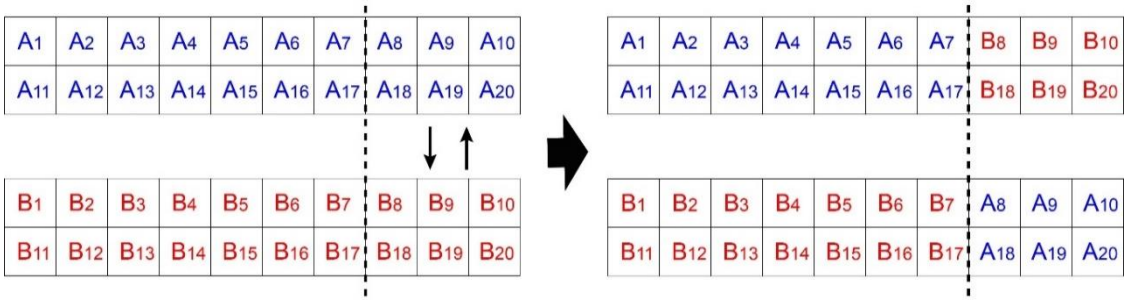

Figure 3-2. The schematic illustration of breeding between individuals A and B shows each individual with 20 features represented by a 2×10 matrix. The values in the matrix are the inner or outer radii of the nanoantenna. The original A and B are displayed on the left in blue and red, respectively. The new individuals generated by the breeding operation are on the right. Each new individual inherits features from both A and B.

Breeding involves data exchange between different individuals, similar to natural reproduction where half of the chromosomes randomly come from the paternal and maternal lines. The exchanged parts of A and B are also randomly selected. To clearly illustrate the

breeding process, the variables in A and B are displayed in different colors, blue for A and red for B, respectively. As shown in the left part of Figure 3-2, A and B are cut into two pieces at a random position. The cut-off parts are then swapped, generating two new individuals with features from both A and B, as seen in the right part of Figure 3-2.

b) Mutation

Mutation occurs in a single individual and involves a random change of variables[6]. Random change here has two meanings: the random selection of variables and the random modification of their numerical values. Taking individual A as an example, we set the mutation rate between 10% and 15%. This means that 2 or 3 variables in A will change to other values. As shown in Figure 3-3, mutation randomly affects features (A4, A9, A17). The unmutated features are displayed in blue, and the mutated features (a4, a9, a17) are marked in red. In this way, a new individual mutated from A is created.

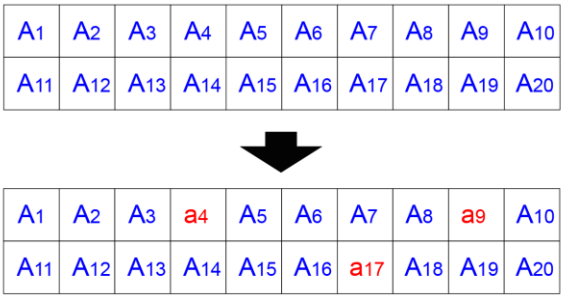

Figure 3-3. The schematic illustration of mutation shows the process occurring in a single individual. The unmutated individual is shown at the top. After mutation, several values are randomly changed (marked in red). The new individual generated by the mutation operation is displayed at the bottom.

The mutation rate directly influences evolution. At a low mutation rate, new individuals look quite similar to the unmutated individuals, which suggests that the new individuals will yield similar results as the unmutated ones. Considering all possibilities of mutations, the group will display a wider range of results during evolution. Therefore, with a low mutation rate, it is more likely to find the desired evolution direction. However, the disadvantage is that the algorithm takes more time and is more likely to be trapped by local optima. Conversely, a high mutation rate provides faster evolution and is more robust against local optima. However, it makes it more difficult to determine the direction of evolution. In this research, we carefully set the mutation rate between 10% and 15% to balance evolution speed, robustness, and accuracy of the evolution direction.

3.2.2 Optimization process of GA

The flow chart below briefly introduces the optimization process of GA.

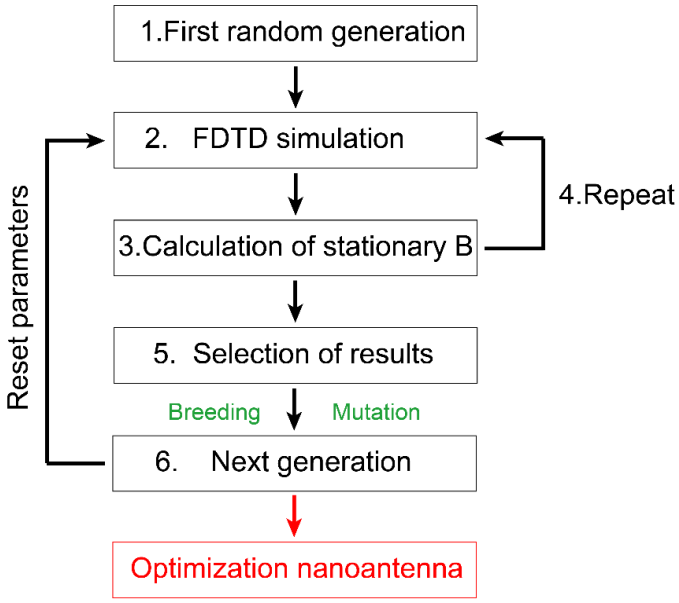

Figure 3-4. Flow chart of GA.

The optimization process consists of six steps:

1) The first generation is randomly created, including 40 individuals. Each individual contains 10 inner and 10 outer radii as variables. The inner and outer radii are within the previously set range.

2) For a single individual, the 10 inner and 10 outer radii are transferred to Lumerical FDTD. Thus, a bull's-eye nanoantenna with these features is modeled in the simulation software.

3) When the simulation is finished, the data are transferred to Matlab. Using the expression of drift current and the Biot–Savart law, the stationary magnetic field (B_stat) created by this nanoantenna is numerically calculated.

4) Each generation contains 40 individuals. Therefore, steps (2) and (3) are repeated 40 times to obtain all the results of the stationary magnetic field (B_stat) within one generation, created by each individual.

5) For one generation, the 40 results are compared. The 20 individuals with the strongest stationary magnetic fields are selected and carried over to the next generation, while the

remaining 20 individuals are discarded.

6) The next generation still contains 40 individuals. Half of them are the best results from the last generation, as mentioned in step (5). The remaining 20 individuals are newly generated from these best results through “breeding” and “mutation” operations. These operations retain the good features of the last generation and create better individuals in the next generation. These new features are then transferred to Lumerical FDTD, and new simulation models are built.

The first generation is randomly created in step (1). The operations from step (2) to step (6) describe a loop for one generation, where GA continuously creates individuals in each generation and retains the best half of them. New individuals are created from the selected individuals that carry desirable features. Through breeding and mutation operations, these desirable features are expected to be preserved and even enhanced, creating better individuals in the next generation.

This loop will repeat many times and stops when the improvement in each generation becomes stagnant. At that time, we choose the best result from the entire group as the optimized nanoantenna.

3.2.3 GA result

We recorded the stationary magnetic field generated at the center of the bull's-eye nanostructures, as seen in the figure below. The X-axis represents the generation, with each generation containing 40 structures. Therefore, there are 40 dots in each generation, and each dot represents a single simulation. The Y-axis represents the stationary magnetic field. We ran GA three times to mitigate the risk of the algorithm falling into a local optimum. The results are displayed in Figure 3-5.

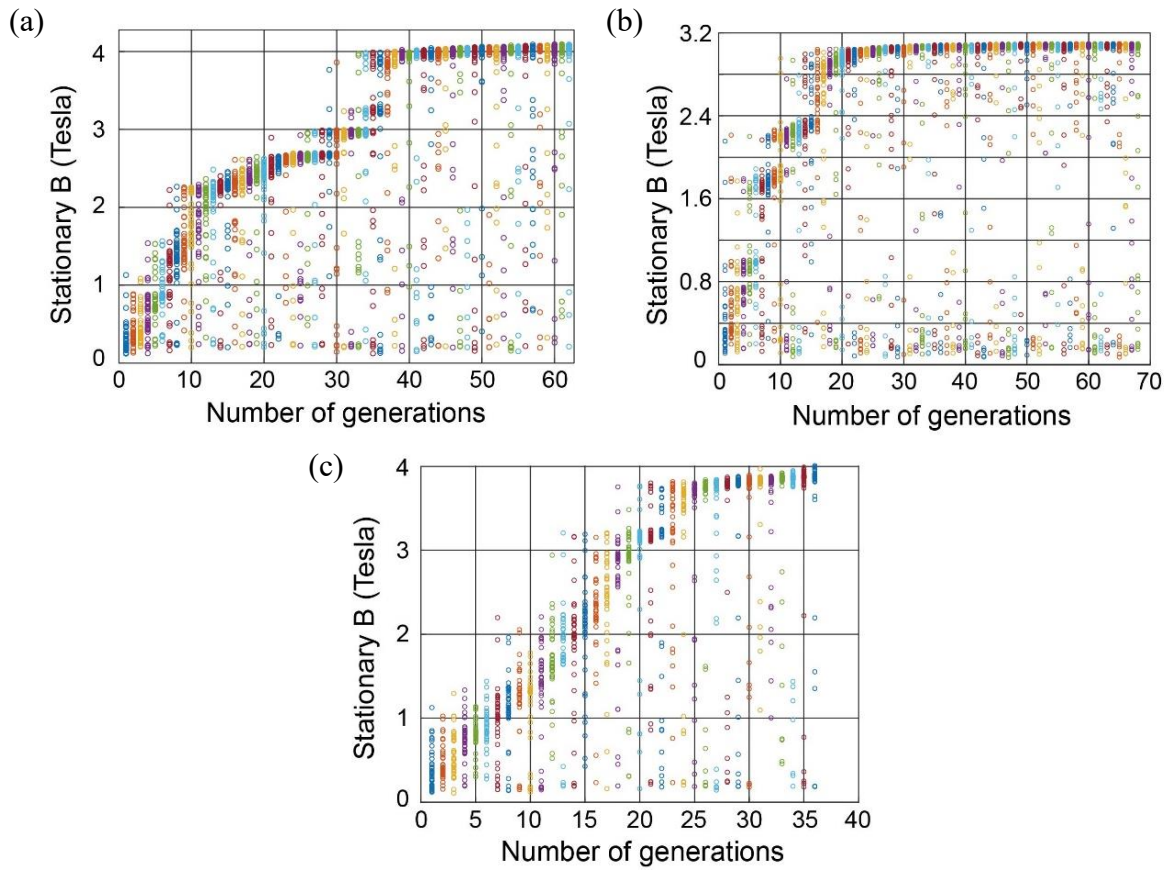

Figure 3-5. Results of three GA procedures, named as GA-(1), GA-(2) and GA-(3), respectively. Each dot represents a single simulation. All the stationary magnetic fields generated in the center of bull-eye nanostructures are recorded.

Clear evolutionary jumps can be observed during the selection process. Good results are more concentrated in the top part, indicating that the desirable features are successfully inherited by the next generation. However, there are still individuals that create weak stationary B fields in later generations. This shows the vitality of GA evolution, meaning that GA is still exploring more evolutionary directions.

We terminated GA when the improvement became nearly stagnant. Each GA procedure took around one month until termination. Consequently, the maximum stationary B fields in Figure 3-5a, Figure 3-5b, and Figure 3-5c are 4.2 T, 3.1 T, and 4 T, respectively.

3.3 Optimal results from GA procedures

In this section, we discuss the optimal results from the three GA procedures. The

corresponding geometric dimensions are shown in the table below.

(a)

Optimal result of GA-(1)										
Groove number	1	2	3	4	5	6	7	8	9	10
Inner radius (nm)	19	45	91	167	222	273	310	355	400	450
Outer radius (nm)	25	75	120	175	232	289	335	377	429	461

(b)

Optimal result of GA-(2)										
Groove number	1	2	3	4	5	6	7	8	9	10
Inner radius (nm)	0	29	85	124	189	245	299	344	400	447
Outer radius (nm)	8	35	91	142	195	274	323	374	422	455

(c)

Optimal result of GA-(3)										
Groove number	1	2	3	4	5	6	7	8	9	10
Inner radius (nm)	19	45	92	159	216	251	308	353	404	443
Outer radius (nm)	25	71	122	177	226	277	331	380	416	451

Figure 3-6. Geometric dimension of three optimal results.

It is interesting to note that the optimal results of GA-(1) and GA-(3) have similar geometric dimensions. As a result, they generate nearly the same amplitude of the stationary magnetic field. In Figure 3-6b, the inner radius of the first groove is zero, meaning the central part of the nanoantenna is air. Compared with the nano groove, the optical field is less enhanced in the hollow center, as discussed in the following paragraphs. This is the reason for the lower stationary magnetic field. Further analysis of the three optimal structures is discussed below.

3.3.1 Optimal result from GA-(1)

Additional calculation results from the optimal structure are presented in this section, including the optical E and H field distribution, the stationary B field amplitude, and its vector field distribution.

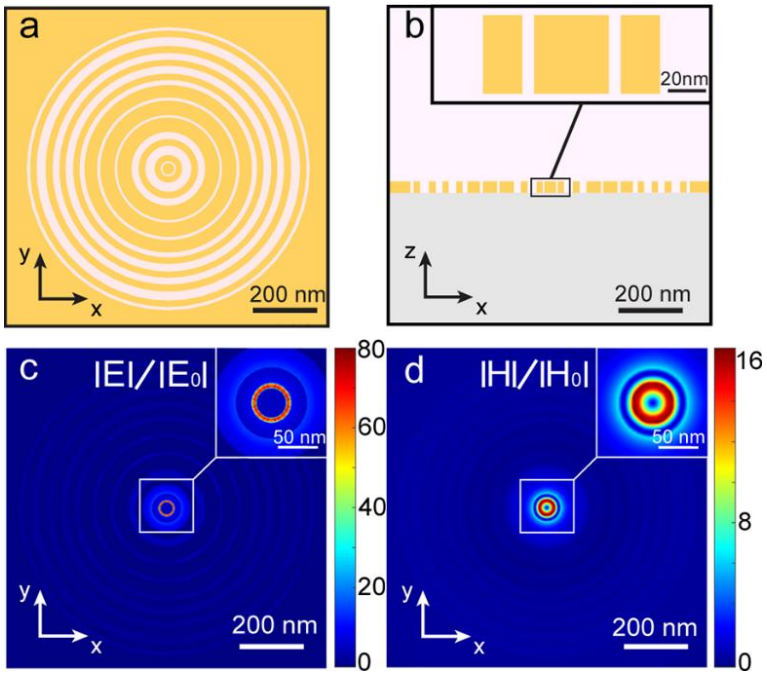

Figure 3-7. Optimal structure from GA-(1). (a) Geometric diagram in XY plane based on the data from Fig. (3-6a). (b) Schematic in XZ plane, including zoom image in central part. Optical (c) E field and (d) H field distribution.

The optimal result from GA-(1) generates the strongest stationary B field. Figure 3-7a and Figure 3-7b show the schematic of this nanoantenna in the XY and XZ planes, respectively. The relative proportions of the grooves in the figure match their actual proportions. Figure 3-7c and Figure 3-7d display the distribution of the optical E and H fields. It is evident that both E and H fields are enhanced in the central part, especially the optical E field, which is enhanced up to 80 times. As discussed in Chapter 2, the stationary B field is proportional to the strength of the drift current, according to the Biot-Savart law. The drift current is proportional to the square of the optical E field, as stated in R. Hertel's expression[7]. Therefore, the stationary B field greatly benefits from the enhanced E field, which is the square of 80 times. Additionally, the enhanced area is ring-shaped, which enables a confined circulating drift current (Figure 3-8). This is the key reason for the ultra-strong stationary B field.

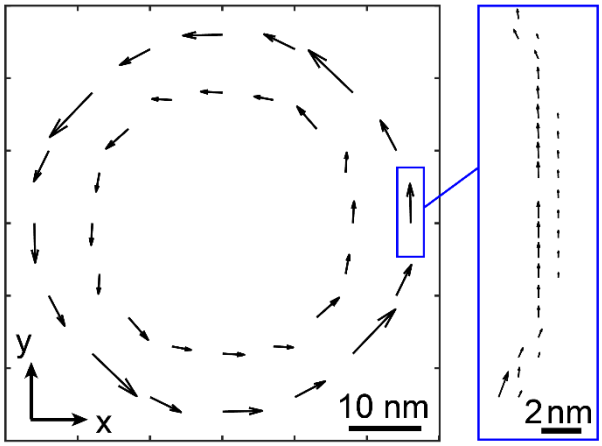

Figure 3-8. Distribution of drift current in XY plane. More detailed exhibition in zoom area is displayed in blue box.

Figure 3-8 shows the distribution of the drift current in the XZ plane at the middle thickness of the gold layer. The original calculation results are densely distributed in space, as seen in the zoomed image in the blue box. The drift current mainly appears at the edge of the metal where the optical field gradient is strongest. The direction is tangent to the edge. We selected part of the calculation result and displayed it on the left for a macro view. All the current vectors are scaled proportionally. The circulating drift currents created by the first groove can be clearly seen. The drift currents are uniformly distributed in azimuthal positions, due to the circular symmetry of both the RHCP light and the bull's-eye nanostructure in the XY plane. Hence, the drift currents are circularly symmetrically distributed. Additionally, the drift current is confined to the nanoscale, with a radius of around 20 nm. Therefore, an ultra-strong stationary B field could be induced by these annular DC currents via the Biot–Savart law.

The induced stationary B field is displayed below, including the three components of the stationary B field (Figure 3-9), the total field distribution (Figure 3-10a), and the vector field distribution (Figure 3-10b and Figure 3-10c).

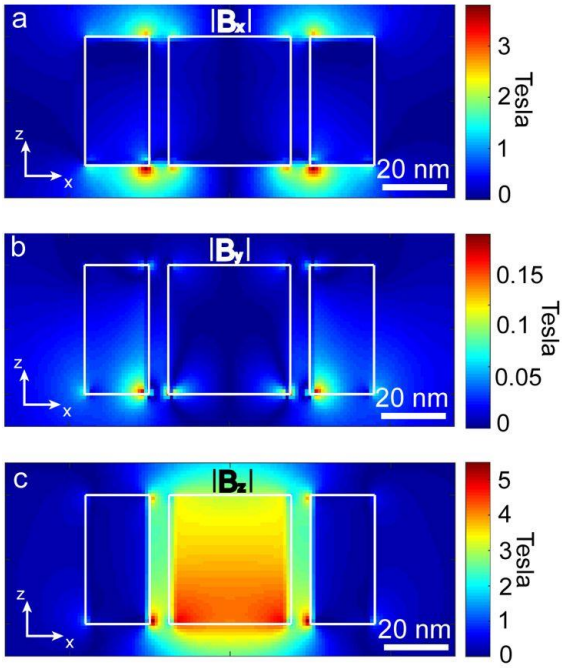

Figure 3-9. (a) x, (b) y and (c) z components of stationary B field.

The stationary B field is induced by drift currents in the XY plane, as seen in Figure 3-8. Therefore, the Bz component dominates the total field distribution. From a macro view, Bz is much stronger than Bx or By, and the total field distribution in Figure 3-10a closely resembles the Bz component in Figure 3-9c.

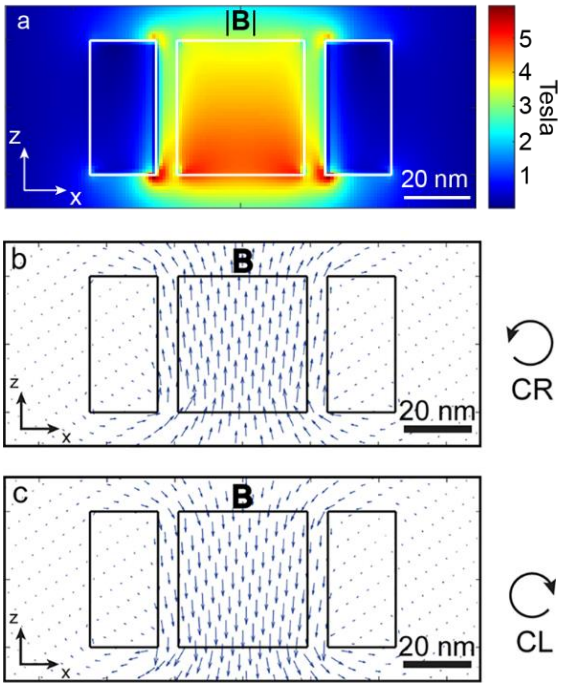

Figure 3-10. (a) Distribution of stationary B amplitude in XZ plane. Distribution of vector B field at (b) RHCP excitation and (c) LHCP excitation.

Figure 3-10a shows the spatial distribution of the stationary B field in an (XZ) cross-section at the center of the nanostructure (black rectangle in the inset of Figure 3-7b). The amplitude of the stationary B field at the center is around 4 T, which is consistent with the results from the GA procedure in Figure 3-5a.

As we can see, the magnetic field is strongly concentrated inside the nanoantenna in a volume of about 50×50×50 nm^3, particularly inside the metal (symbolized by the white rectangles). The strongest stationary B field appears at the bottom, which is reasonable since the incident light comes from the bottom. The amplitude of the stationary B field exponentially decays as we move away from the structure. This behavior is directly related to the $(1/r^2)$ dependence of Biot-Savart's law. Nevertheless, the strength of the stationary B field remains in the tesla range at a distance of about 10 nm from the metal in the z-direction. This range would allow practical use of this magnetic field. Notice that the value of the B field is overall slightly lower than in the selection process (Figure 3-5a) due to the change in mesh size from 2 nm to 1 nm, allowing a finer estimation of the field.

Figure 3-10b shows the vector distribution of the stationary B field under RHCP excitation. By replacing RHCP light with LHCP light, we can reverse the rotation direction of the drift currents in the XY plane and hence achieve a flip of the stationary B field in the z

direction, as seen in Figure 3-10c.

3.3.2 Optimal result from GA-(2)

The optimal result from GA-(2) is special because it features a structure with a hollow central part, as seen in Figure 3-11a, where the inner radius of the first groove is zero. The schematic diagram is provided here.

Figure 3-11a clearly shows the hollow center of this optimal nanostructure from GA-(2). As mentioned earlier, the optical field is less enhanced in the hollow center compared to the field enhancement in the nano groove. This phenomenon is clearly shown in Figure 3-11c, where the strongest E field enhancement appears in the groove but not in the hollow center.

Therefore, even though the E field enhancement still reaches 80 times, the central part contributes less to the drift current or stationary B field. The enhanced area in Figure 3-11c forms a ring shape, similar to the enhanced area in Figure 3-7c, but with a larger radius, leading to a decrease in the induced stationary B field at the center. Hence, less stationary B field is created. On the other hand, the strongest stationary B fields appear in the air, as seen in Figure 3-11e and Figure 3-11f. In contrast, in Figure 3-10a, the induced stationary B field is mainly confined to the metallic area. This significantly enhanced stationary B field in the hollow area may find applications in specific situations.

Figure 3-7

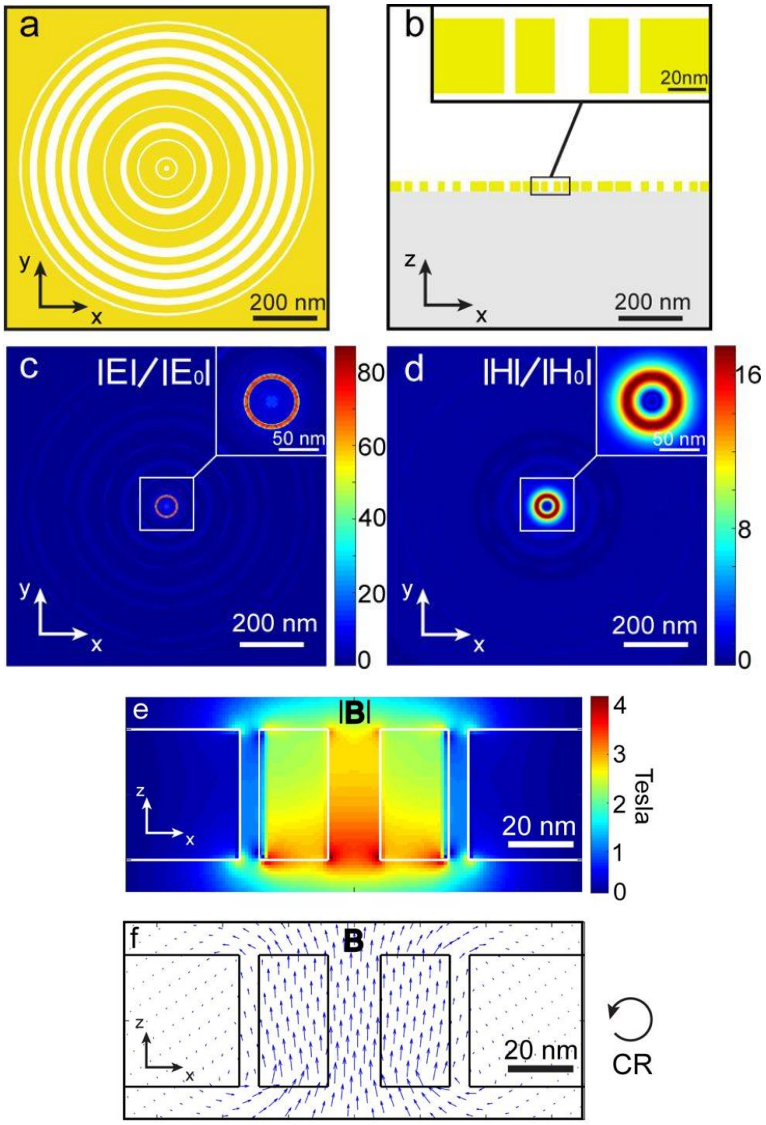

Figure 3-11. Optimal structure from GA-(2). (a) Geometric diagram in XY plane based on the data from Fig. (3-6b). (b) Schematic in XZ plane, including zoom image in central part. Optical (c) E field and (d) H field distribution. (e) Distribution of stationary B amplitude in XZ plane. (f) Distribution of vector B field at RHCP excitation.

3.3.3 Optimal result from GA-(3)

The optimal result from GA-(3) has a similar geometric dimension to that from GA-(1), as seen in Figure 3-6a and Figure 3-6c. The corresponding optical field and induced stationary B field are displayed below.

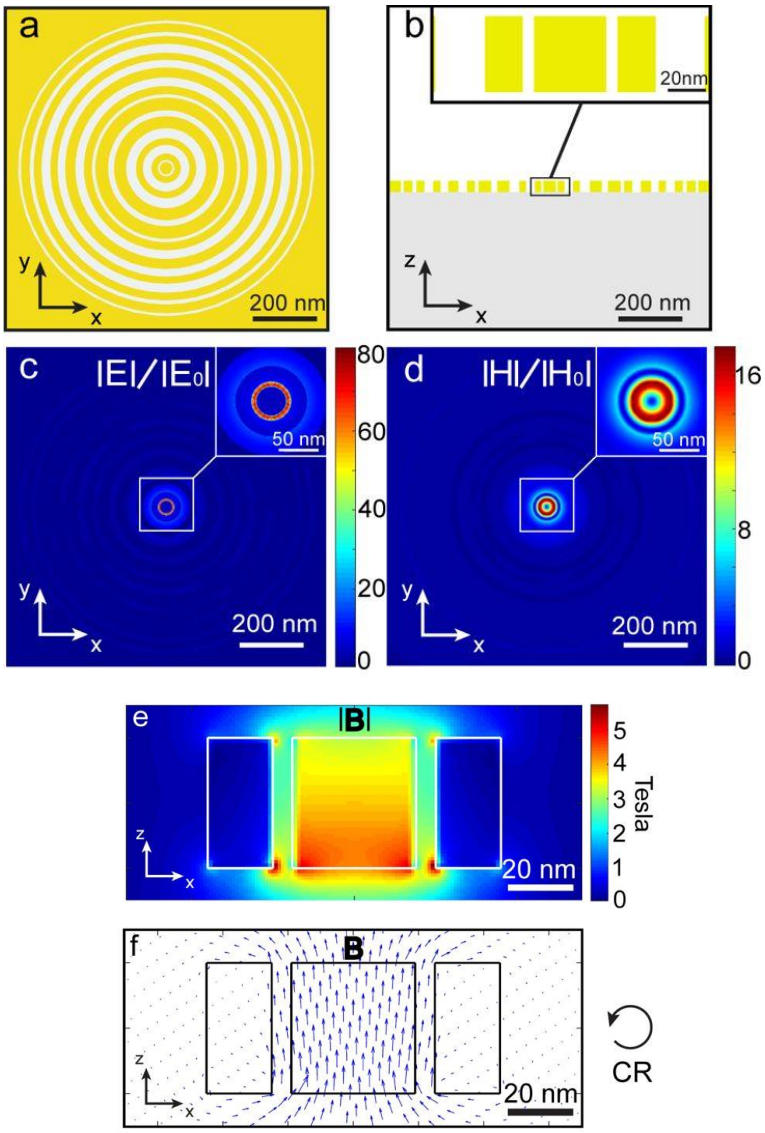

Figure 3-12. Optimal structure from GA-(3). (a) Geometric diagram in XY plane based on the data from Fig. (3-6b). (b) Schematic in XZ plane, including zoom image in central part. Optical (c) E field and (d) H field distribution. (e) Distribution of stationary B amplitude in XZ plane. (f) Distribution of vector B field at RHCP excitation.

The optimal structure from GA-(3) has similar calculation results to that from GA-(1) due to their close geometric dimensions. Therefore, the analysis of the optimal result from GA-(1) is also valid here.

Considering all three optimal structures, two different optimal stationary B fields are generated, which are 4 T and 3.2 T. This indicates that GA has the possibility of falling into a local optimum. In GA-(2), the improvement became stagnant after the 15th generation. While it is possible that GA might eventually escape this local optimum due to a positive mutation, the time cost is considerable. We have already spent one month on the GA procedure, and it is uncertain how long it would take to escape the local optimum. In this research, we chose to run the GA procedure again. Because the first generation is randomly created, the GA procedure will follow a new evolutionary path, avoiding the local optimum from the previous run. Nonetheless, our GA is still an efficient tool for us, as seen in three aspects:

1) GA-(1) and GA-(3) found similar inner and outer radii and resulted in nearly the same stationary B field. This indicates that GA successfully identified the good features for generating an ultra-strong stationary B field in the bull's-eye nanostructure.

2) The enhancement of optical E fields reached up to 80 times in all three optimal structures, creating stationary B fields in the tesla range. This outcome is exactly what we expected.

3) GA effectively reduced the time cost. Traversal scanning of 20 parameters in Lumerical FDTD takes an exponentially increased amount of time, while with GA, we obtained a good result within just one month.

3.4 Optimized nanoantenna

Comparing all three optimal results, the strongest stationary B field appears in GA-(1), reaching up to 4.1 T. Therefore, we choose the optimal result from GA-(1) as our final optimized nanoantenna. In this section, we study the time response and spectral response of this optimized nanoantenna.

3.4.1 Time response of optimized nanoantenna

We read data from the "field time" monitor in Lumerical FDTD to obtain the optical E field in the time domain. From these data, we can study the response of the stationary B field and the drift current in the time domain. The results are shown in the figure below.

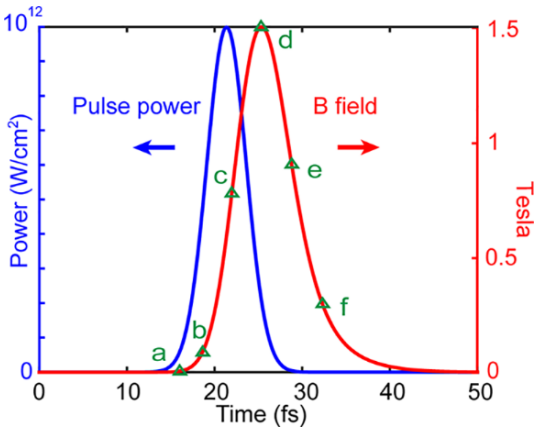

Figure 3-13. Time response of optimized nanostructure. Blue curve represents the power density in timeline. Red curve is the response of stationary B field at center of nanoantenna in time domain.

Figure 3-13 mainly reveals the response delay between incident light and induced stationary magnetic field. In Lumerical FDTD, the incident light is a pulse beam with a full-width at half-maximum power temporal duration of 5.3 fs. The incident power reaches its maximum at around 21 fs, as shown by the blue curve in Figure 3-13. The red curve shows the temporal behavior of the magnetic field created by the drift current. Firstly, we observe that the electrons' response time delays the magnetic pulse by about 4 fs with respect to the optical pulse. This delay is linked to the time needed for the structure to start being powered. [8, 9].

Furthermore, even though the optical pulse's peak power is the same as used in the search for an optimal structure by the GA, the magnetic field (B) created by the antenna reaches only about 1.5 T, which is quite different from the 4.1 T shown in the GA results. This discrepancy is due to the fact that the system does not have enough time to reach a steady state before the end of the optical pulse. The GA is based on frequency-domain simulation, which represents the steady state result of continuous wave (CW) excitation in the time domain. Therefore, the system takes time to reach this steady state once energy input begins. In the case of a short pulse incident beam, the system does not have enough time to reach the steady state during the pulse duration. For this reason, the nanostructure does not have time to be fully energized before the end of the pulse, preventing it from generating a stronger magnetic field. Hence, the stationary B field in Figure 3-13 declines before reaching 4.1 T.

This explanation is further verified by additional simulation results, where we incrementally increase the pulse duration. The peak values of the stationary B field over time from each simulation are recorded, as shown in the figure below.

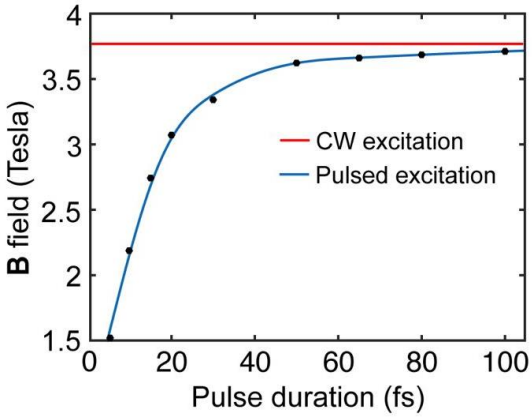

Figure 3-14. Peak value of stationary B field in time domain. Each dot represents an independent simulation with different time duration of incident pulse beam.

In Figure 3-14, each dot represents an independent simulation where the optimized nanoantenna is excited by a pulse beam of varying time durations. The peak values of the stationary B field in the time domain are recorded. We show the results in the figure with pulse duration on the X-axis and the stationary B field on the Y-axis. It is clearly displayed that the peak value of the stationary B field increases as we extend the pulse duration. The blue curve represents the fitted results, showing a continuous increase. The red line predicts the peak value if we excite the nanoantenna with a continuous wave (CW) beam. In the case of a long incident pulse beam, the maximum stationary B field in the time domain is quite close to 4.1 T, as derived from the frequency-domain calculation. Therefore, the explanation we proposed earlier is well verified. Using longer pulses, we could generate higher magnetic fields until saturation.

To visualize the delay between optical excitation and the induced stationary B field, we show the optical E field and stationary B field in the XZ plane at different times, as indicated by green triangles in Figure 3-13. The incident light comes from the (-z) direction and propagates to the (+z) direction. We display the Ey component of the incident light in the XZ plane so that both wavefront and phase information can be observed.

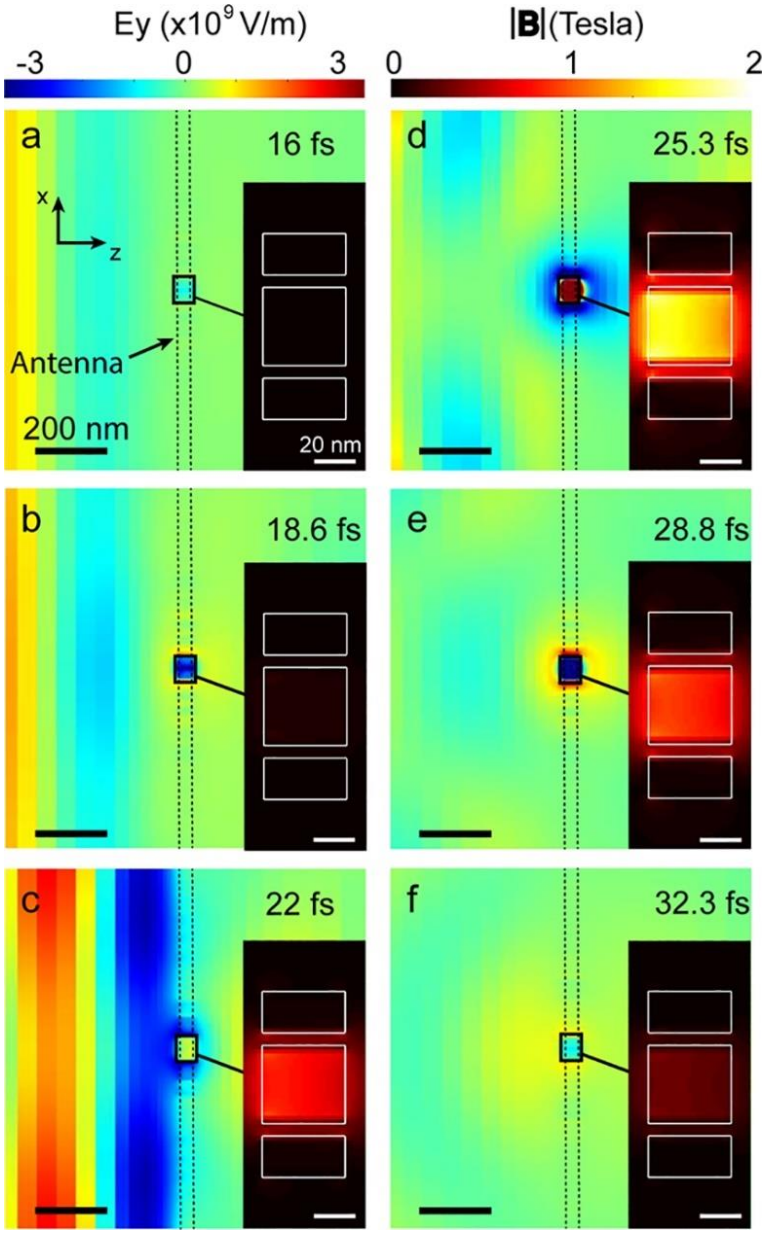

Figure 3-15. Distribution of stationary B field in the XZ plane (zoom in inset) induced by the optical pulse together with the E_y component of incident light propagating through the simulation window for different times. These times are also represented on the red curve in Figure 3-13 by green triangles. The position of the optimized plasmonic antenna in XZ plane is shown by dashed lines.

In Figure 3-15, we clearly observe the shift between the incident light and the induced stationary B field. While the optical pulse is already interacting with the optical nanoantenna, the stationary B field is still almost zero, as seen in Figure 3-15b. Conversely, in Figure 3-15d, when the optical pulse is almost at its minimum, the stationary B field is at its maximum.

Finally, although the electromagnetic wave has disappeared in Figure 3-15e and Figure 3-15f, the stationary B field is still present and decreases slowly due to the dissipation time of the energy within the nanostructure. Note that the stationary B field distributions shown in Figure 3-15 correspond to the instantaneous stationary field produced by the drift currents existing in the nanostructure at the time considered. This stationary B field results from two diametrically opposed currents in the nanoantenna, which rotate around each other, generating a stationary magnetic field in the center of the structure at every instant of the optical pulse.

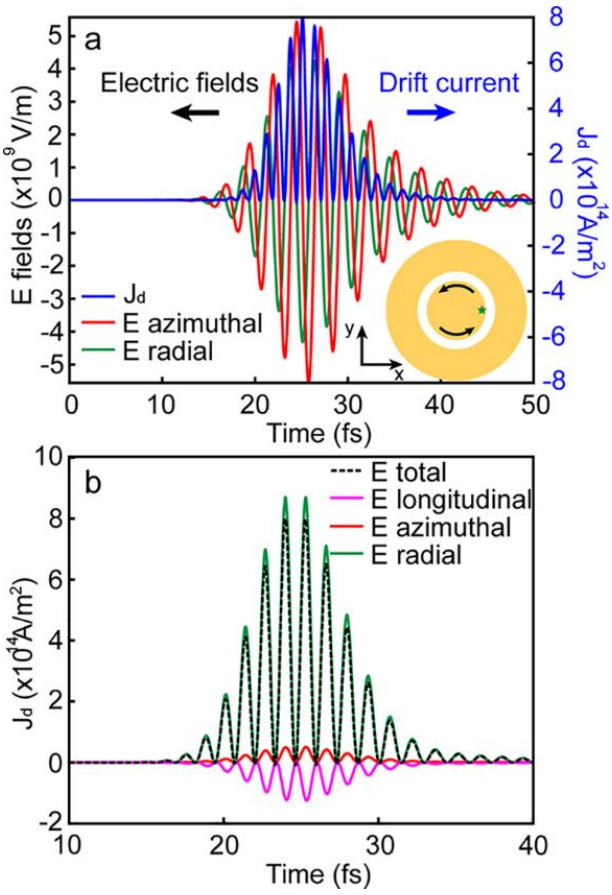

Figure 3-16. Temporal response of drift currents. (a) Temporal evolution of the drift currents (blue curve), superimposed on the temporal evolution of the radially (green curve) and azimuthally (red curve) polarized electric fields, inside the metal core of the plasmonic nanoantenna, symbolized by the green star in the inset drawing. (b) Contribution of the different components, longitudinal (along z), azimuthal and radial, of the electric optical field in generating drift currents

To further understand this temporal phenomenon, and in addition to what R. Hertel has demonstrated on long time scales, Figure 3-16 shows the temporal behavior of drift currents inside the metal (i.e., the real part of $e \cdot \delta n \cdot \mathbf{v}$), in the central part of the plasmonic nanostructure.

The exact location is indicated by a green star in the inset of the figure. Likewise, the radially and azimuthally polarized electric fields at the same position are also displayed. From this analysis, we can make two major observations. First, the generation of drift currents is in phase with the radially polarized electric field and is 90° out of phase with the azimuthally polarized electric field. Second, the temporal dynamics of the drift currents show behavior in good agreement with the nonlinear quadratic process described in Eq. (2-26). In particular, they are created at twice the frequency of the incident wave, when the azimuthal electric field is at its maximum and minimum. This means that two diametrically opposed drift currents coexist and rotate around each other at each moment in the plasmonic nanostructure (inset in Figure 3-16a), allowing the generation of a stationary magnetic field at any given time during the optical pulse.

To better understand the different vectorial contributions of the electric field, and since an azimuthal component of the electric field is required for the creation of the drift currents at the origin of the IFE in the nanoantenna, Figure 3-16b represents the different contributions of the electric field components in the generation of the drift currents inside the antenna. At the same position as in Figure 3-16a, the electric field is decomposed into longitudinal (along z), azimuthal, and radial components. Figure 3-16a shows the drift currents as a function of these different electric field components.

From these results, we can make several observations:

(1) The azimuthal drift currents are carried by the azimuthal component of the electric field.

(2) The main contribution to the drift current comes from the radial component of the electric field. This is directly related to the very strong confinement of the field in the first groove of the GA-optimized structure.

(3) The electric field's longitudinal contribution (along z) has a negative effect on the drift currents, contributing to a decrease in the latter.

These results provide a fine understanding of the physical mechanism involved and its temporality, allowing further manipulation of these drift currents.

3.4.2 Spectral response of optimized nanoantenna

The spectral characteristic of the optimized nanoantenna is also studied. We obtain the spectral response by varying the wavelength of the incident light step by step. As in the GA procedure, we choose the point at the center of the optimized nanoantenna and calculate the stationary B field in the frequency domain.

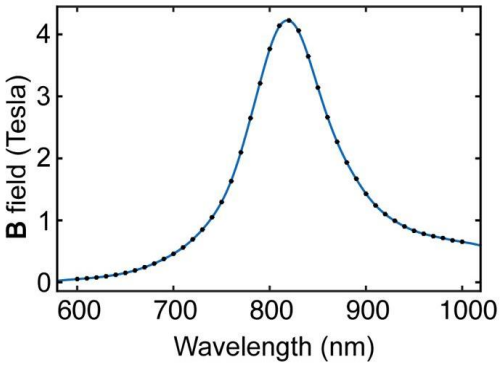

Figure 3-17. Spectral response of optimized nanostructure.

The stationary B field versus wavelength is displayed in the Figure 3-17. It reaches a maximum at around 820 nm, which is very close to the excitation wavelength chosen in this study (800 nm). This result again demonstrates the attractiveness of this algorithmic approach for optimizing plasmonic, and by extension, photonic resonant nanostructures.

3.5 Conclusion

In conclusion, we described the creation of drift currents in a bull's-eye nanostructure. We demonstrated that using this formalism, a plasmonic nanostructure optimized by a genetic algorithm could create stationary magnetic fields in the tesla range under high-power light excitation. This B-field is highly confined to a region of a few tens of nanometers, mainly oriented out of plane and reversible on demand by switching from right to left circular polarization, thus allowing total control of its out-of-plane orientation.

We also showed that under the influence of femtosecond optical excitation, a pulse of stationary magnetic field of the tesla order is created, lasting for a duration of a few femtoseconds. We established that the dynamics and intensity of this field are defined by the relaxation time of the electrons and the time needed by the optical nanostructure to dissipate the energy it had stored. Furthermore, we highlighted the contribution of the different components of the optical electric field in the generation of azimuthal drift currents in the plasmonic nanostructure, with significant representation of the radial component due to a strong capacitive effect in the antenna. This allows for a better understanding of the phenomenon and further manipulation of these currents.

Understanding the physical behavior of drift currents inside photonic nanostructures allows us to foresee even more efficient antenna designs for the generation of stationary

magnetic fields. In particular, in this study, only the azimuthal component of the drift current is used, but one could imagine utilizing all the spatial components of these currents with different antenna designs. Moreover, the generation of stationary direct current or stationary magnetic fields is only one of the applications we envision for these currents in metallic nanostructures.

The use of plasmonic nanostructures for the all-optical generation of stationary magnetic fields that are confined, intense, switchable on demand, and operable on the femtosecond time scale represents a turning point for many technological and scientific applications.

Additionally, the optimization is realized by a genetic algorithm. The modeling in Lumerical FDTD, simulation, and mathematical calculations in Matlab are all controlled by the algorithm itself, ensuring the optimization process is fully automated. The integration of Lumerical FDTD and Matlab through API allows us to employ multiple algorithms to achieve various research objectives, including but not limited to GA optimization. By incorporating various theoretical frameworks, we can delve into new scientific inquiries. By replacing GA with other algorithms, we can achieve multiple research objectives. This setup provides flexibility in tackling complex research challenges across different domains.

REFERENCE

[1] J. Kim, R. Soref, W.R. Buchwald, Multi-peak electromagnetically induced transparency (EIT)-like transmission from bull's-eye-shaped metamaterial, Optics express, 18 (2010) 17997-18002.

[2] H. Kollmann, X. Piao, M. Esmann, S.F. Becker, D. Hou, C. Huynh, L.-O. Kautschor, G. Bösker, H. Vieker, A. Beyer, Toward plasmonics with nanometer precision: nonlinear optics of helium-ion milled gold nanoantennas, Nano letters, 14 (2014) 4778-4784.

[3] F. Gerges, G. Zouein, D. Azar, Genetic algorithms with local optima handling to solve sudoku puzzles, Proceedings of the 2018 international conference on computing and artificial intelligence, 2018, pp. 19-22.

[4] J. Krüger, D. Dufft, R. Koter, A. Hertwig, Femtosecond laser-induced damage of gold films, Applied surface science, 253 (2007) 7815-7819.

[5] P. Poole, S. Trendafilov, G. Shvets, D. Smith, E. Chowdhury, Femtosecond laser damage threshold of pulse compression gratings for petawatt scale laser systems, Optics express, 21 (2013) 26341-26351.

[6] M. Mitchell, An introduction to genetic algorithms, MIT press1998.

[7] R. Hertel, Theory of the inverse Faraday effect in metals, Journal of magnetism and magnetic materials, 303 (2006) L1-L4.

[8] D. Gall, Electron mean free path in elemental metals, Journal of applied physics, 119 (2016).

[9] M. Blanco, F. Cambronero, M.T. Flores-Arias, E.C. Jarque, L. Plaja, C. Hernández-García, Ultraintense Femtosecond Magnetic Nanoprobes Driven by Azimuthally Polarized Laser Beams, European Quantum Electronics Conference, Optica Publishing Group, 2019, pp. eg_2_6.

4 Stationary magnetic field through linearly polarization

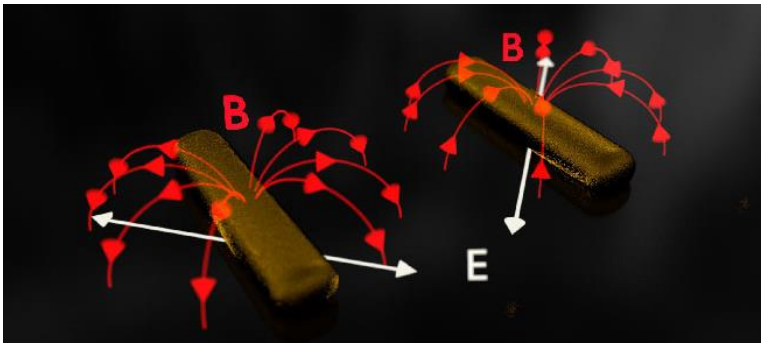

It is commonly believed that only circular polarizations can magnetize matter through the inverse Faraday effect (IFE)[1, 2]. In this chapter, we demonstrate a method to create a stationary magnetic field using linearly polarized incident light, as shown in the schematic above. This phenomenon results from the local manipulation of light by a plasmonic gold nano-antenna. We show that a gold nanorod excited by linearly polarized incident light generates non-zero magnetic fields when the incident polarization of the light is not parallel to the long axis of the rod. Moreover, by varying the angle of the incident linear polarization with respect to the nano-antenna, we demonstrate the on-demand flipping of the magnetic field orientation.

4.1 Excitation condition of stationary B field

The stationary B field in our research is induced by an annular DC current, also known as drift current, as described by Eq. (2-26). To illustrate the excitation condition of the stationary B field, we illuminate a gold nanosphere with circularly polarized light and linearly polarized light, respectively.

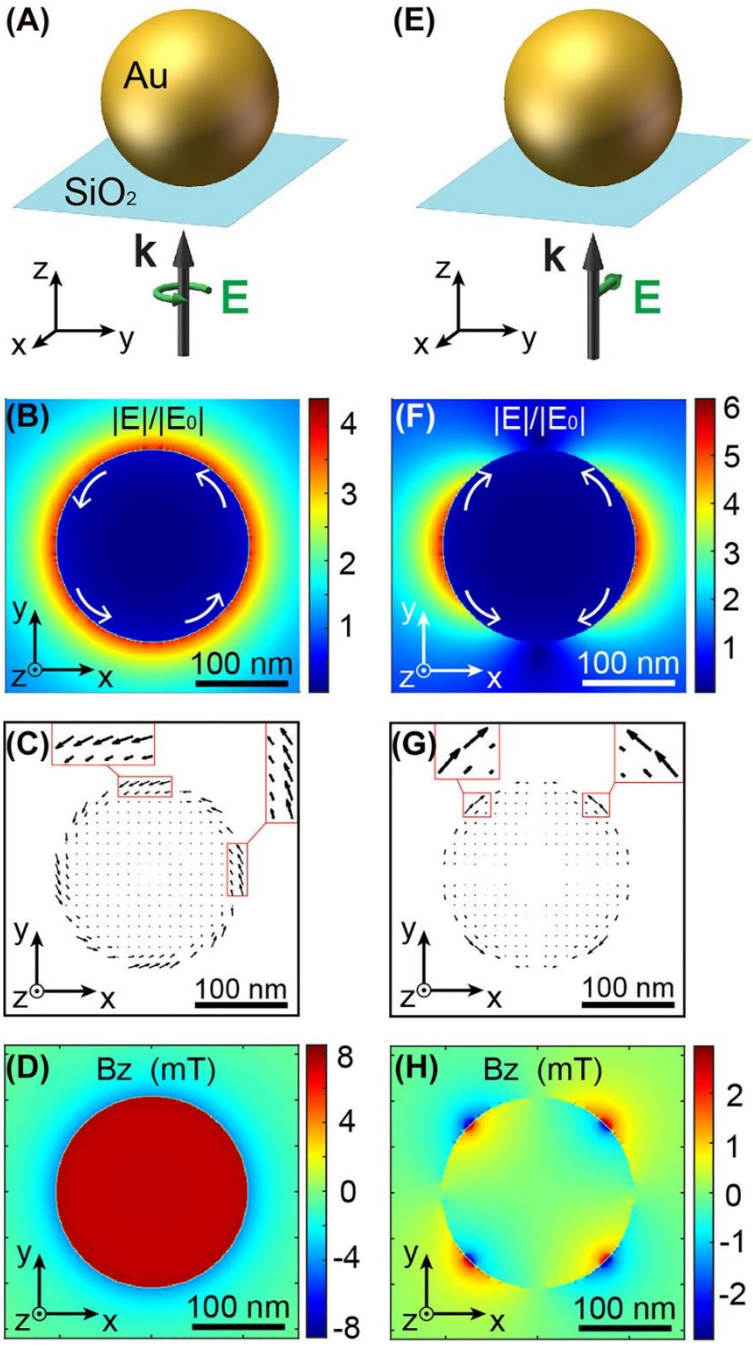

Figure 4-1. Drift current and stationary B field in a gold nanoparticle. Generation of drift currents and stationary magnetic fields in a gold nanoparticle excited by (a)–(d) a circular polarization and (e)–(h) a linear polarization. (a) and (e) Schematic representation of the gold nanoparticle excited by a right-circular or x-linear polarization, respectively, at the wavelength of 800 nm and for an intensity of 10^{12} W/cm2. For the two excitation conditions shown in (a) and (e), the normalized electric field distributions (b) and (f), the associated drift currents (c) and (g), and the generated stationary magnetic fields (d) and (h) are shown, respectively.

A gold nanosphere is a typical nanostructure used to excite drift currents and create a stationary B field[3]. Here, we excite an Au nanosphere with circularly polarized light and linearly polarized light of wavelength 800 nm, respectively, as shown in Figure 4-1a and Figure 4-1e. The Au nanosphere is surrounded by a medium with an index of n = 1 and placed on a glass substrate. The nanosphere has a diameter of 200 nm, which is close to the resonant dimension with respect to the wavelength of the incident light. Although the nanosphere is not at its resonant peak at 800 nm (Figure 4-2b), the magnetic field generated is maximal at this wavelength, as seen in Figure 4-2a.

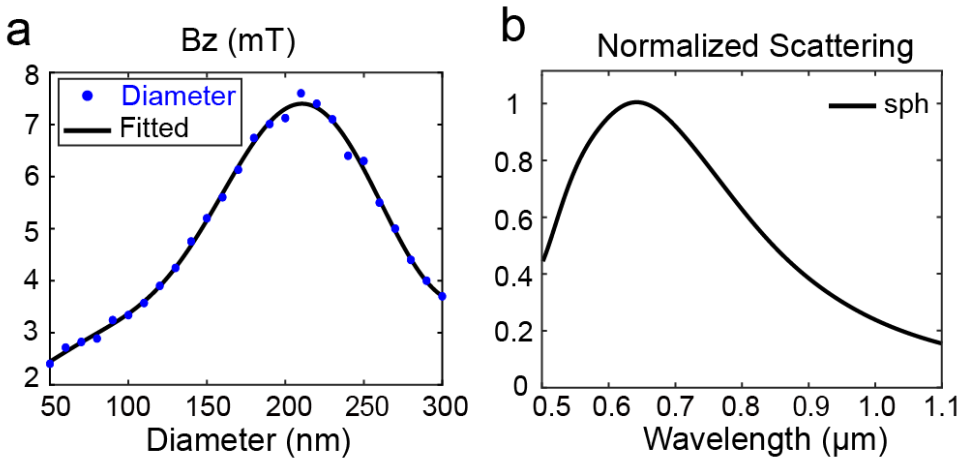

Figure 4-2. (a) Stationary B field generated in the center of nanosphere at 800 nm. Each blue dot represents a nanosphere of different diameter. Black curve is the fitted result, where the stationary reaches maximum at 200 nm. (b) Normalized scattering spectrum of Au nanosphere of diameter 200 nm, the resonant peak is around 650nm.

Figure 4-1b and Figure 4-1f show the optical electric field enhancement in the XY plane at the center of the nanoparticle, calculated by finite difference time domain simulations (Lumerical FDTD). The particle operates in the electric dipole (ED) resonant mode, as seen in the E field distribution in Figure 4-1f. The field enhancement is around 6 times. In contrast, Figure 4-1b shows less field enhancement because the incident light has a fixed power density of 10^{12} W/cm^2. In the case of circularly polarized light, the energy is uniformly distributed around the nanoparticle, resulting in less field enhancement. These distributions of electric fields and field gradients generated in the near-field of the nanoparticle create, via IFE and Eq. (2-26), in-plane drift currents azimuthally polarized inside the metal (Figure 4-1c and Figure 4-1g). The directions of the drift currents are also schematically displayed in Figure 4-1b and

Figure 4-1f by white arrows. Through the Biot-Savart law, these currents generate the magnetic field distributions in the near-field. Figure 4-1d and Figure 4-1h show the z component of this stationary B field.

We choose the z component for a clear comparison of the stationary B field generated by circularly polarized light and linearly polarized light. As previously reported, under circularly polarized excitation, a gold nanoparticle generates a non-zero stationary magnetic field of a few mT for this range of excitation intensity, which is displayed again in Figure 4-1d by our own calculation. On the other hand, when excited by linear polarization, the symmetry of the drift currents (Figure 4-2g) does not allow the creation of a global net magnetic field, as they cancel each other out.

Nevertheless, local B fields can still exist around the nanoparticle due to these drift currents (Figure 4-1h). The problem lies in the high symmetry of the drift current or stationary B field. However, the IFE requires circular polarization, which breaks this symmetry and generates a non-zero global magnetic field. The comparison between Figure 4-1c, d and Figure 4-1g, h is inspiring for us. If we find another way to break this symmetry, we could generate a stationary B field through linearly polarized incident light. This is something rarely described before.

4.2 Light-induced stationary B field in rod nanoantenna

Gold nanospheres are among the most popular plasmonic nanostructures due to their ease of production[4] and their exceptional properties in terms of optical confinement[5, 6], heat generation[7], and chemical catalysis[8]. Another extensively studied plasmonic system is gold nanorods[9]. Due to their elongated geometry, these nanoantennas allow for finer manipulation of the light–matter interaction, primarily due to their polarization sensitivity to the optical electric field[10]. More importantly for our purposes, the nanorod lacks symmetry along the transverse and longitudinal directions.

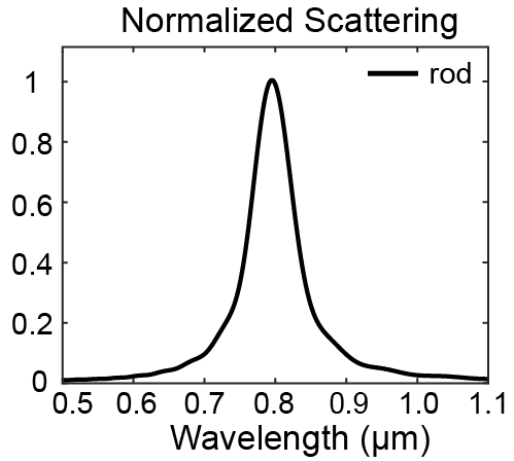

Figure 4-3. Normalized scattering spectrum of Au with geometric dimension of 120×20×40 nm^3 that corresponds to length, width and thickness, respectively.

The symmetry in a nanosphere system is destroyed by circularly polarized light, while in a nanorod, the symmetry is naturally broken due to its geometric shape. Therefore, we utilize this property to generate a stationary B field via the linear polarization of light. We set the width and thickness of the nanorod to be 20 nm and 40 nm, respectively. The length is specifically selected as 120 nm to ensure it operates in the ED mode, as seen in Figure 4-3.

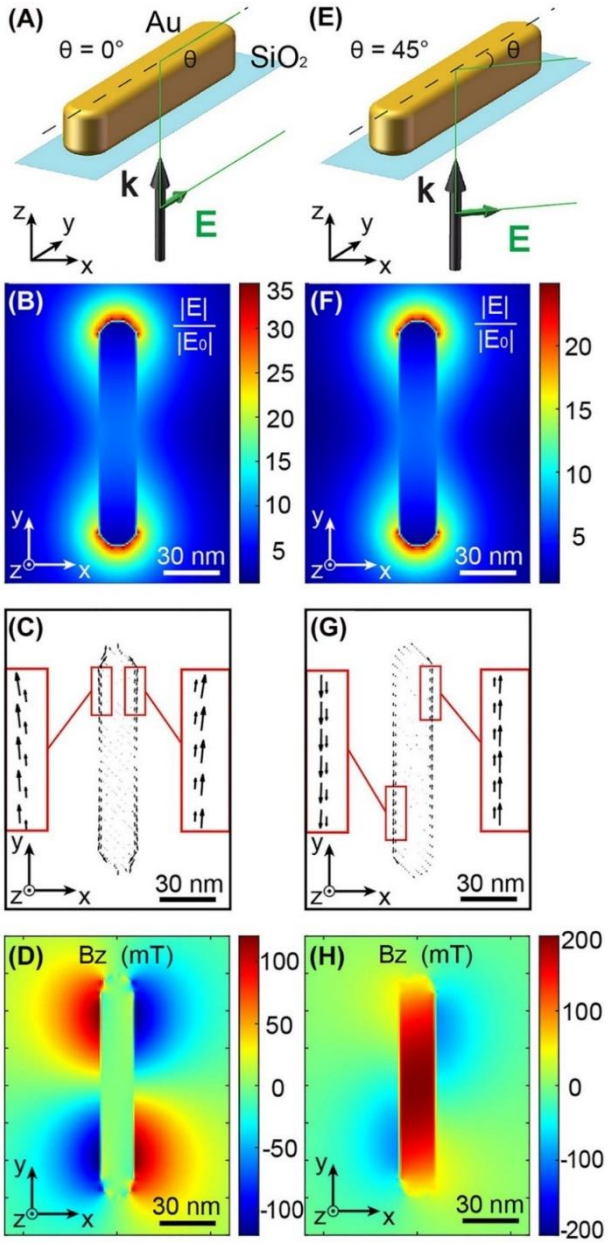

Figure 4-4. Light-induced stationary B field through linearly polarized incident light. Au nanorod of length L = 120 nm, thickness T = 40 nm, width W = 20 nm is excited by incident light polarized along (a-d) long side (θ = 90°) and (e-h) 45° from the x-axis. (a) and (e) are schematic representation of the gold nanorod excited by linear polarization at θ = 0° and 45° from the antenna's long axes, respectively. For the two excitation conditions shown in (a) and (e), the normalized electric field distributions (b) and (f), the corresponding drift currents (c) and (g), and generated stationary magnetic fields (d) and (h) are displayed, respectively.

Similar to the nanosphere, the Au nanorod is placed on a glass substrate and excited by a

linearly polarized plane wave with a wavelength of 800 nm from the (-z) direction, as seen in Figure 4-4a and Figure 4-4e.

The incident light has the same wavelength (800 nm) and power density (10^{12} W/cm^2). as before. Two linear polarization angles are studied in Figure 4-4. The first one (Figure 4-4a-d) is oriented along the y-axis (θ = 90°), corresponding to the long side of the antenna. The other one (Figure 4-4e-h) is oriented at 45° from the short side (x-axis) of the nanorod. We choose these polarization angles because 90° and 45° represent two typical situations: the presence of symmetry and the absence of symmetry. In the case of 90°, either the incident light or the nanorod has mirror symmetry along the y-axis, while for 45°, this symmetry is broken by the incident light.

Figure 4-4b and Figure 4-4f display the normalized electric field distributions in the XY plane at the center of the antenna for these two polarizations. As shown, the distributions are extremely similar because, in both cases, the nanorod operates in the ED resonant mode. They differ in E amplitude enhancement because the incident light has a fixed power density. For 90°, the incident energy is fully utilized to excite the ED resonance along the y direction, while for 45°, only half of the energy is directed along the y direction, leading to less E field enhancement. Although it is difficult to distinguish them from the E field distribution, the drift currents show quite different distributions in Figure 4-4c and Figure 4-4g. For the 90° case, drift currents are symmetrically distributed along the y axis due to the symmetry of the incident light and nanorod. They are located at the four corners of the antenna, and the drift currents on both sides of the y axis have the same amplitude and direction, as seen in the zoomed image of Figure 4-4c, creating an overall zero magnetic field by the structure (Figure 4-4d). In contrast, in Figure 4-4g, this balance is destroyed. The drift currents along the 45° direction are stronger than the others, leading to a macroscopic circulating current around the nanorod.

The different distribution of drift currents results in completely different stationary B fields. In Figure 4-4d, there is a highly anti-symmetric distribution of the stationary B field. This anti-symmetry arises from the properties of the Biot-Savart law. The cross product of the current and position vector in different directions leads to opposite B fields on either side of the y axis, hence no net stationary B field is created. In contrast, in Figure 4-4h, the circulating drift currents create a confined stationary B field inside the nanorod, similar to the nanosphere when excited by circularly polarized light in Figure 4-2d. For this reason, the magnetic fields generated by these currents are distributed in a very different way. This unexpected physical behavior is surprising given the similar optical electric field distributions for the different polarization angles used and described in Figure 4-4.

Something also interesting is that the local B-fields for a 45° polarization have an amplitude 25 times higher than the case of the gold sphere excited under the same conditions. This remarkable light-matter interaction demonstrates that light-induced magnetization is

possible using linear polarization of the light, which is rarely reported before.

4.3 Analytical explanation

As mentioned in Chapter 2, the direction of the drift current is related to spin density. Therefore, the behavior of symmetrically distributed drift currents and circulating drift currents can be explained by different spin density patterns. Spin density is defined by the cross product of the E field and its conjugate [Eq. (2-35)]. To demonstrate the origin of these different spin density patterns, we start with the calculation unit of spin density, which is the E field.

4.3.1 Linear decomposition of E field

Due to the geometric character of the nanorod, it has two basic modes. The local E field can therefore be separated into two parts, corresponding to the contributions from the transverse mode and the longitudinal mode, respectively. It is known that a gold nanorod behaves like an electric dipole, both in terms of radiation pattern[11] and field lines[12]. In fact, both two modes are, ED resonances oriented in different directions. They are excited by different components of the incident light, with the longitudinal mode corresponding to the y component of the incident light and the transverse mode corresponding to the x component of the incident light. At a polarization of 90°, when the incident light is parallel to the long side of the nanorod (y component), only the longitudinal mode is excited. On the other hand, at a polarization of 0°, only the transverse mode is excited, as seen in the schematic illustration in the first panel of Figure 4-5.

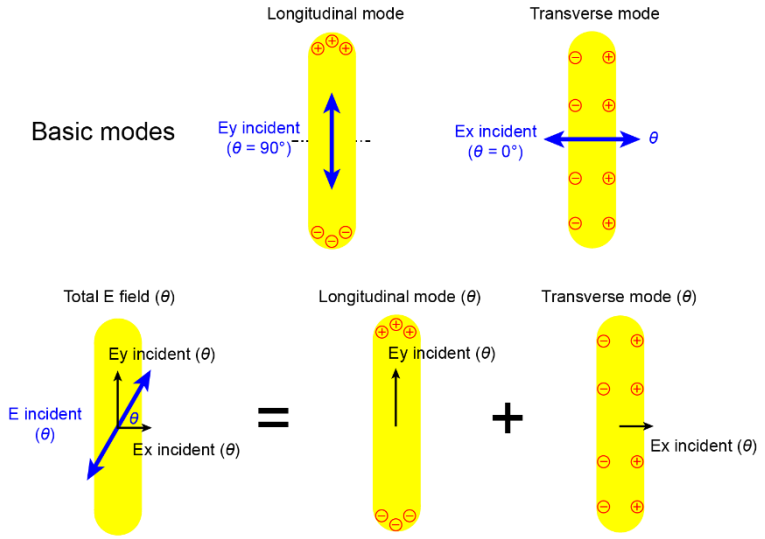

Figure 4-5. Schematic illustration of two basic modes. Total E field could be decomposed into contribution from longitudinal and transverse mode that excited by different components of incident light, respectively.

At a polarization of an arbitrary angle (θ), both modes are excited. Due to the linear properties of Maxwell's equations in this nanorod response system, the total E field can be decomposed into contributions from the longitudinal and transverse modes, as shown in the second panel of Figure 4-5. We denote the E field from the longitudinal mode as $\mathbf{E^L}$, and the E field from the transverse mode as $\mathbf{E^T}$. Therefore, the total field from the two modes is:

$$\mathbf{E}(\theta) = \mathbf{E}^L(\theta) + \mathbf{E}^T(\theta) \tag{4-1}$$

where

$\mathbf{E}(\theta)$	Total E field when polarization angle of incident light is θ
$\mathbf{E}^L(\theta)$	E field from longitudinal mode
$\mathbf{E}^T(\theta)$	E field from transverse mode

The two modes are independently excited by the x and y components of the incident light. The strength of the two modes is scaled to the source of this excitation, which is the amplitude of the x or y component from the incident light. In other words, they depend on the polarization angle (θ).

$$\begin{aligned} \mathbf{E}^L(\theta) &\rightarrow E_0^{inc} \cdot \sin(\theta) \\ \mathbf{E}^T(\theta) &\rightarrow E_0^{inc} \cdot \cos(\theta) \end{aligned} \tag{4-2}$$

where

E_0^{inc} Amplitude of incident light

As seen in Eq. (4-2), the polarization angle (θ) determines the proportion of incident energy allocated to the two modes

4.3.2 Decomposition of spin density

Since the E field is the calculation unit of spin density and we have already separated the E field into two parts, the spin density in Eq. (2-35) thereby becomes:

$$\mathbf{s}(\theta) = \frac{1}{E_0^2} \mathrm{Im}\left[\left(\mathbf{E}^L(\theta) + \mathbf{E}^T(\theta) \right)^* \times \left(\mathbf{E}^L(\theta) + \mathbf{E}^T(\theta) \right) \right] \tag{4-3}$$

Spin density, being a typical nonlinear effect, can be decomposed into four terms: contributions from the longitudinal mode, the transverse mode, and the two mode coupling parts.

$$\begin{aligned} \mathbf{s}(\theta) = & \frac{1}{E_0^2} \mathrm{Im}\left[\left(\mathbf{E}^L(\theta) \right)^* \times \left(\mathbf{E}^L(\theta) \right) \right] + \frac{1}{E_0^2} \mathrm{Im}\left[\left(\mathbf{E}^T(\theta) \right)^* \times \left(\mathbf{E}^T(\theta) \right) \right] \\ & + \frac{1}{E_0^2} \mathrm{Im}\left[\left(\mathbf{E}^L(\theta) \right)^* \times \left(\mathbf{E}^T(\theta) \right) \right] + \frac{1}{E_0^2} \mathrm{Im}\left[\left(\mathbf{E}^T(\theta) \right)^* \times \left(\mathbf{E}^L(\theta) \right) \right] \end{aligned} \tag{4-4}$$

In Eq. (4-4) two mode coupling parts in fact give same result.

$$\mathrm{Im}\left[\left(\mathbf{E}^L(\theta) \right)^* \times \left(\mathbf{E}^T(\theta) \right) \right] + \mathrm{Im}\left[\left(\mathbf{E}^T(\theta) \right)^* \times \left(\mathbf{E}^L(\theta) \right) \right] = 2\,\mathrm{Im}\left[\left(\mathbf{E}^L(\theta) \right)^* \times \left(\mathbf{E}^T(\theta) \right) \right] \tag{4-5}$$

Therefore, the total spin density is decomposed into three components: the spin density of the longitudinal mode, the spin density of the transverse mode, and the spin density from mode coupling.

$$\mathbf{s}(\theta) = \mathbf{s}^L(\theta) + \mathbf{s}^T(\theta) + \mathbf{s}^{L-T}(\theta) \tag{4-6}$$

To better understand and visualize this decomposition in Eq. (4-6), we perform three independent Lumerical FDTD simulations:

1) **Simulation 1**. Setting the polarization angle to 0°, so that only the transverse mode is excited. In this case, we display the z component of the spin density pattern (Figure 4-6a) because the z component describes the polarization state of the E field in the XY plane, which is directly related to the direction of the drift current, as demonstrated in Chapter 2. This pattern is indeed the visualization of the transverse mode's spin density pattern.

2) **Simulation 2**. Setting the polarization angle to 90°. For the same reason, we visualize the spin density pattern of the longitudinal mode (Figure 4-6b).

3) **Simulation 3**. Setting the polarization angle to an arbitrary value, here we choose θ = 45°. We then display the corresponding spin density pattern (Figure 4-6c).

Figure 4-6 shows the spin density patterns at different polarization angles, derived from three independent simulations. Figure 4-6b displays the spin density pattern at a polarization of 90°. It represents the spin density in the XY transverse plane at the center of the rod for an incident polarization oriented along the Y axis. Figure 4-6b shows high anti-symmetry along the x and y axes. This is the origin of the symmetrical drift currents displayed in Figure 4-4c and the global zero magnetic field in Figure 4-4d. Figure 4-6a shows the spin density pattern at 0°, which also exhibits anti-symmetry along the x and y axes. The corresponding spin density value is much lower than that in Figure 4-6b because the longitudinal dimension is the perfect resonant length of the nanorod at 800 nm, as shown in Figure 4-3, while the transverse dimension is not at the resonant length.

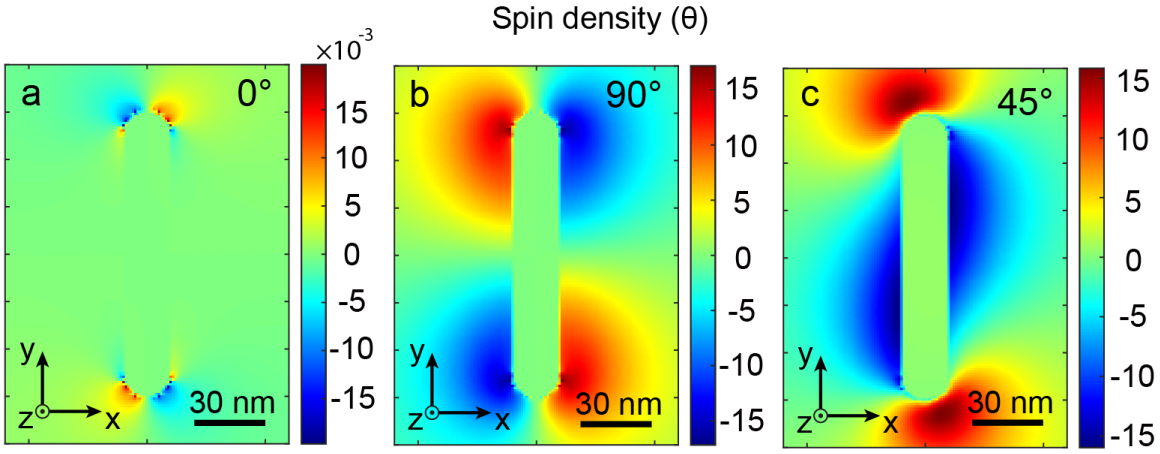

Figure 4-6. Spin density (z component) calculated by Eq. (2-35) at incident polarization angle of (a) 0°, (b) 90° and (c) 45°, respectively.

On the other hand, as observed in Figure 4-6c, changing the angle of the incident polarization θ = 0° to 45° modifies the spin density distribution altogether. While it was perfectly symmetrical in the case of θ = 0°, the distribution is now completely inhomogeneous, with large lobes along the nanorod (with negative spin density) and two smaller spots at the tips of the antenna (with positive spin density). This dissymmetry creates local elliptical polarization of the same sign along the nanorod.

Among the three, Figure 4-6a and Figure 4-6b are special because they represent the spin

density patterns of the transverse and longitudinal modes, respectively. According to Eq. (4-6), the spin density patterns of the transverse and longitudinal modes exist at any polarization angle. For different polarization angles, the strength of the transverse and longitudinal modes is modulated by the incident angle, as shown in Eq. (4-2). Therefore, Figure 4-6c should have an intrinsic relationship with Figure 4-6a and Figure 4-6b.

To reveal this relationship, we create a "numerically combined" spin density pattern for 45° polarization using Eq. (4-6). We achieve this through four steps

1) We preserve the E field data from Simulation 1), as it represents the transverse mode. The E field from Simulation 1) can be transferred into $\mathbf{E^T}$ in Eq. (4-1) and modified by the corresponding coefficient cos(θ), as shown in Eq. (4-2). Here, the coefficient is cos(45°). Therefore, we calculate $\mathbf{s^T}$ in Eq. (4-6) using the modified $\mathbf{E^T}$ from **Simulation 1**. This result is also displayed in Figure 4-7c.

$$\mathbf{s}^T = \mathrm{Im}\left[\left(\cos(45^\circ)\cdot\mathbf{E}^T\right)^* \times \left(\cos(45^\circ)\cdot\mathbf{E}^T\right)\right]$$

2) Similarly, for $\mathbf{s^L}$, we use $\mathbf{E^L}$ from **Simulation 2** modified by the coefficient sin(45°) (Figure 4-7a).

$$\mathbf{s}^L = \mathrm{Im}\left[\left(\sin(45^\circ)\cdot\mathbf{E}^L\right)^* \times \left(\sin(45^\circ)\cdot\mathbf{E}^L\right)\right]$$

3) For $\mathbf{s^{L\text{-}T}}$, we use $\mathbf{E^T}$ from **Simulation 1** and $\mathbf{E^L}$ from **Simulation 2** and modify them with cos(45°) and sin(45°), respectively.

$$\mathbf{s}^{L-T} = 2\cdot\mathrm{Im}\left[\left(\sin(45^\circ)\cdot\mathbf{E}^L\right)^* \times \left(\cos(45^\circ)\cdot\mathbf{E}^T\right)\right]$$

4) According to Eq. (4-6), we sum $\mathbf{s^T}$, $\mathbf{s^L}$ and $\mathbf{s^{L\text{-}T}}$ from Step (1-3) and display this “numerically combined” in Figure 4-7d.

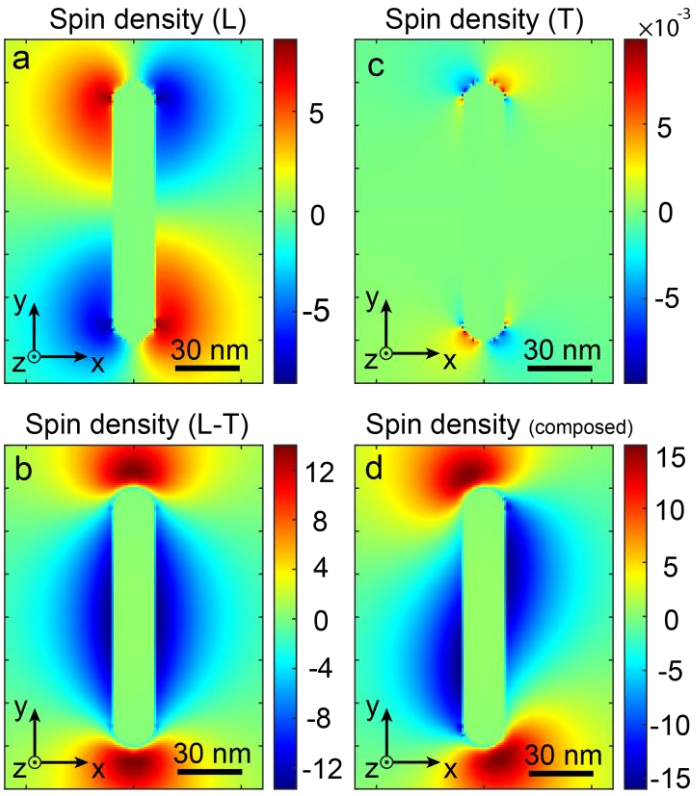

Figure 4-7. Decomposition of spin density. Contribution of (a) longitudinal mode, (b) mode couping and (c) transverse mode in spin density pattern. (d) Composed result from longitudinal mode, transverse mode and mode couping accroding to Eq. (4-6).

It should be noted that this result comes from a numerical combination of data from different Lumerical FDTD simulations. The composed result in Figure 4-7d is exactly the same as the spin density pattern of 45° in Figure 4-6c. From this decomposition in Figure 4-7, we can reveal the origin of the circulating drift current.

Since we have already separated spin density into three components, we can investigate the origin of the circulating drift current. The result in Figure 4-7, where the polarization of incident light is 45°, is a good example. Figure 4-7 displays the spin density pattern for each component in Eq. (4-6).

Figure 4-7a represents the spin density pattern from the longitudinal mode. As one can see, its distribution is the same as that in Figure 4-6b, but with a lower amplitude due to a lower amount of energy projected to this mode. Four lobes appear at the four corners of the nanorod with perfectly equal amplitude, having the same sign on the diagonal of the antenna but opposite signs on the same edge. The different signs of (s_z) can be understood as light confinements of different helicities. For light coming from the background and polarized in

the XY plane, a positive spin density can be associated with right circular polarization, while a negative density corresponds to left circular polarization. Therefore, the four corners of the nanorod are surrounded by differently circularly polarized light, leading to a zero net stationary B field. We have already shown this in Figure 4-4c and Figure 4-4d, where incident light polarized at 90° selectively excites the longitudinal mode and no net stationary B field exists.

Figure 4-7c depicts the spin density pattern of the transverse mode and shows an anti-symmetrical distribution in the four corners of the antenna, similar to the longitudinal mode, but with a much lower amplitude due to a lack of resonance. Consequently, the longitudinal and transverse modes will not create a global non-zero magnetic field since, in these anti-symmetries, the drift currents cancel out. While the two basic modes exist in the pattern of an arbitrary polarization angle, what matters for an arbitrary polarization angle is the coupling mode, not the two basic modes.

As shown in Figure 4-7b, the coupling mode exhibits a spin density distribution quite different from either basic mode. The left and right parts of the drift current show the same spin density. The spin density itself describes the polarization state of light. The spin density pattern in Figure 4-7b indicates that the nanorod is surrounded by circularly polarized light, similar to the case in Figure 4-1a. Therefore, the coupling mode can break the anti-symmetry along the x or y axis in the total spin density pattern. It is the origin of the asymmetric, circulating drift currents (Figure 4-4g) and generates the magnetic field presented in Figure 4-4h.

Hence, the sum of the three modes gives the distribution of spin density shown in Figure 4-7d, which is identical to Figure 4-6c. Thus, the coupling between the longitudinal and transverse modes of this plasmonic dipole antenna allows the generation of a stationary B field via linearly polarized light.

4.4 Manipulation of stationary B field

We have already explained the origin of the light-induced stationary B field in a nanorod via linearly polarized light, which is the coupling between the longitudinal and transverse modes. Since the incident energy that splits into the longitudinal and transverse modes is proportional to its y and x components, respectively, we can control the strength of the longitudinal and transverse modes by adjusting the polarization angle (θ). This allows us to manipulate the coupling mode. Based on this analysis, the light-induced stationary B field should be related to the polarization angle (θ), as described below.

The spin density of the coupling mode is calculated using the E field from the longitudinal and transverse modes, as seen in Eq. (4-5). The E fields from these two modes are proportional

to sin(θ) and cos(θ), respectively. Thus, the strength of the coupling mode is proportional to the product of sin(θ) and cos(θ).

$$\mathbf{s}^{L-T}(\theta) \propto \sin(\theta)\cdot\cos(\theta)$$
$$\mathbf{s}^{L-T}(\theta) \propto \frac{1}{2}\sin(2\theta) \tag{4-7}$$

Since the coupling mode is the only origin of the stationary B field, the light-induced stationary B field is proportional to sin(2θ). We choose the point at the center of the nanorod and show the stationary B field versus the polarization angle, as seen in Figure 4-8. Here, we display the Bz component to observe the variation in positive and negative values, which indeed represents the flip of the induced stationary B field along the z axis.

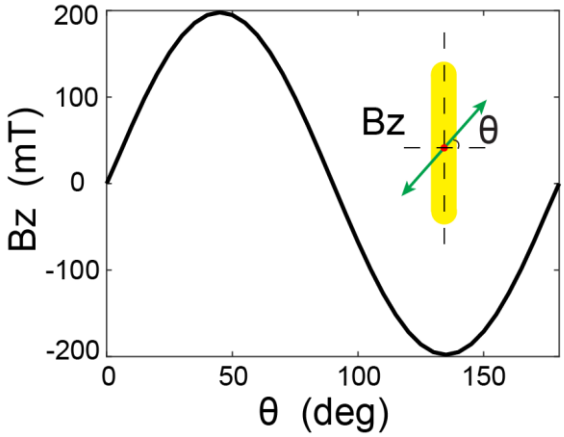

Figure 4-8. Stationary B field at the center of nanorod vs polarization angle.

The stationary B field at different polarization angles is depicted in Figure 4-8. It follows a standard sine function, exactly as demonstrated in Eq. (4-7). The stationary B field is zero for θ = 0°, 90° and 180°, as shown in Figure 4-4d. The magnetic field oscillates between a positive maximum for θ = 45° and a negative minimum for θ = 135°. Therefore, we can achieve continuous manipulation of the induced stationary B field in the nanorod. By rotating the linear incident polarization, the orientation of this magnetic field is also reversible.

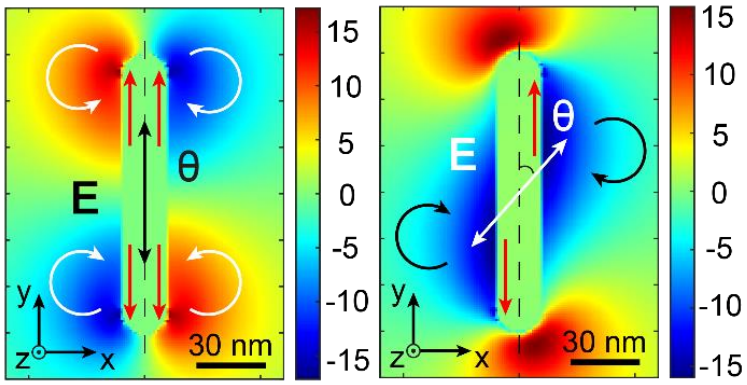

Figure 4-9. Comparison of $\theta = 90°$ (left) and $\theta = 45°$ (right). The color repersents spin density, which indicates local polarization state. The handedness of local elliptically polarized light is depicted by circle arrow. The red arrows represent drift currents.

Figure 4-9 displays the comparison of $\theta = 90°$ and $\theta = 45°$. It is clear shown that nanorod created symmetric drift currents and zero net stationary B field at 90°. However, when the polarization angle $\theta = 45°$, the symmetry of the spin density and drift current is broken. In summary, it is noteworthy that a linearly polarized light-induced stationary B field in a plasmonic antenna can, on demand, reverse the generated magnetic field by simply rotating the incident polarization. This behavior would be useful in the all-optical ultrafast manipulation of magnetic domains, as two opposite magnetic field orientations are achievable for the same power density and heat generation in the structure.

As a supplement to Figure 4-8, we also show the total spin density pattern in the corresponding XY plane for each polarization angle.

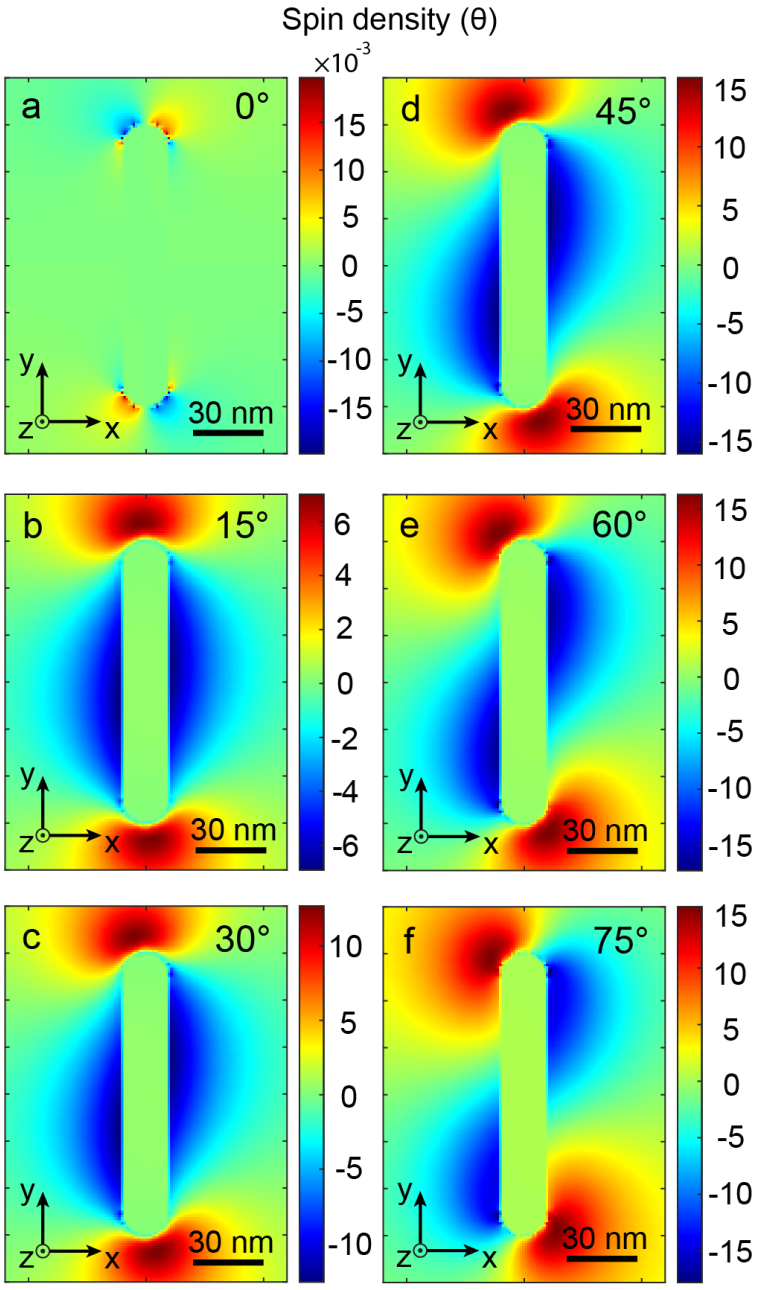

Figure 4-10. Spin density pattern for different polarization angles, from (a) 0° to (f) 75°.

Figure 4-10 shows the spin density pattern corresponding to polarization angles from 0° to 75°. An interesting observation is the spin density pattern for small polarization angles, such as 15° in Figure 4-10b, which has a similar pattern to the coupling mode in Figure 4-7b. However, the value of the spin density is much lower due to weak resonance in the y direction. For polarization angles greater than 45°, the spin density value reaches 15 due to the strong

ED resonance from the longitudinal mode, as seen in Figure 4-10d, e, and f. At 45°, the spin density has the strongest value as well as a well-distributed pattern that covers the main part of the nanorod.

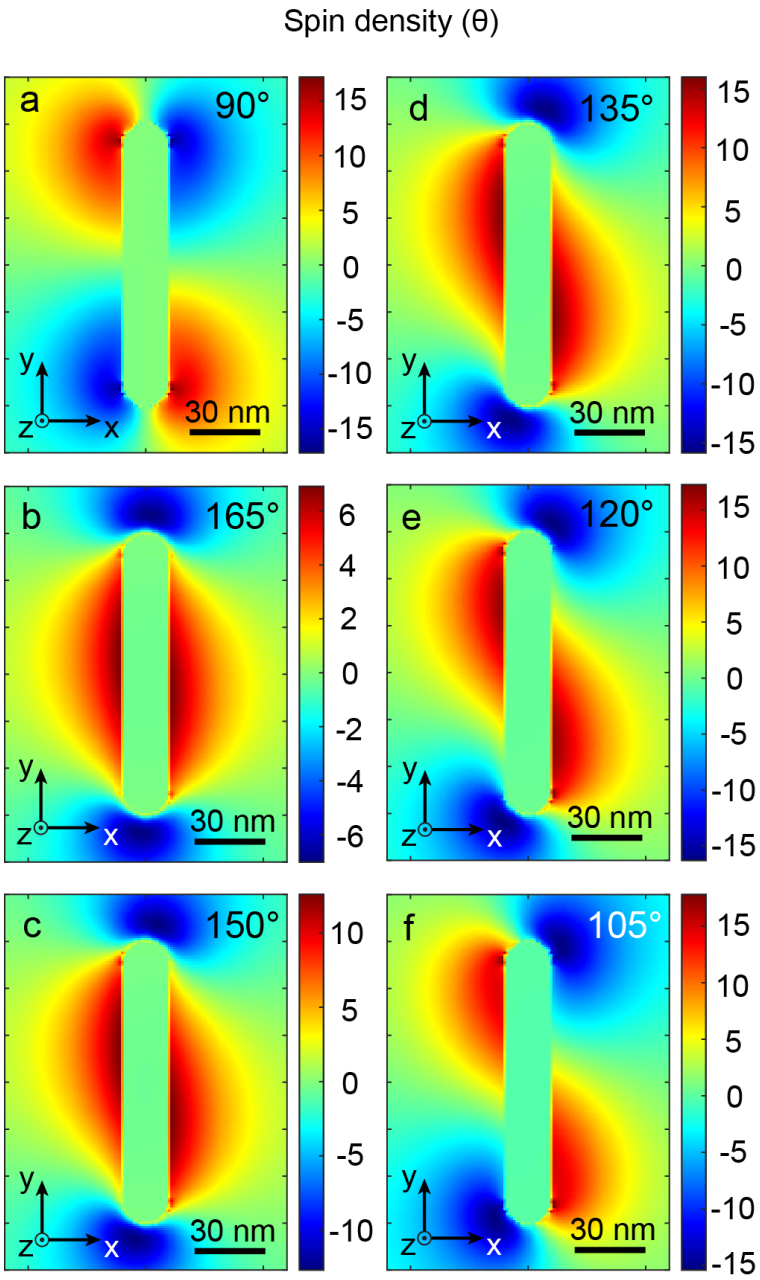

Figure 4-11. Spin density pattern for different polarization angles, from (a) 90° to (f) 165°.

In Figure 4-11, we show the spin density patterns for the remaining polarization angles.

We place results from pairs of complementary angles in the same position in Figure 4-10 and Figure 4-11. For instance, Figure 4-10b and Figure 4-11b give opposite values in spin density and a mirror reflection of the distribution along the y axis. We attribute this phenomenon to the same y component but opposite x component in the incident light, which reverses the handedness of the light.

From these spin density patterns, we can observe the evolution of the local polarization state along the incident polarization angle in the near field, providing a supplementary explanation of the result depicted in Figure 4-8.

4.5 Conclusion

In conclusion, we have demonstrated that linear polarization of light can generate a stationary B field. While this magneto-optical phenomenon is typically believed to be generated only by circular or elliptical polarization, we achieved this linear excitation of the stationary B field by manipulating light at the nanoscale with a plasmonic nanostructure. The demonstration of this intriguing physical effect originates from the local manipulation of the optical nano-antenna's spin density (local polarization state of the light).

In particular, the use of a gold nanorod excited by linear polarization oriented at 45° to its principal axes generates a homogeneously distributed spin density. Consequently, the nanorod creates circulating drift currents and a stationary B field. The magnetic field produced is then reversible on demand simply by changing the polarization angle with respect to the nanorod. Its intensity is up to 25 times higher than that of a gold nanoparticle excited by circular polarization of the same power and frequency.

Thus, this research will allow the ultrafast manipulation of magnetic domains in the near field through linear polarization. The induced magnetic field or magnetization could be simply manipulated by changing the angle of the incident polarization on the plasmonic nanoantenna.

REFERENCE

[1] J. Van der Ziel, P.S. Pershan, L. Malmstrom, Optically-induced magnetization resulting from the inverse Faraday effect, Physical review letters, 15 (1965) 190.

[2] H.-L. Zhang, Y.-Z. Wang, X.-J. Chen, A simple explanation for the inverse Faraday effect in metals, Journal of magnetism and magnetic materials, 321 (2009) L73-L74.

[3] A. Nadarajah, M.T. Sheldon, Optoelectronic phenomena in gold metal nanostructures due to the inverse Faraday effect, Optics Express, 25 (2017) 12753-12764.

[4] C. Louis, O. Pluchery, Gold nanoparticles for physics, chemistry and biology, World Scientific2017.

[5] P. Anger, P. Bharadwaj, L. Novotny, Enhancement and quenching of single-molecule fluorescence, Physical review letters, 96 (2006) 113002.

[6] S. Kühn, U. Håkanson, L. Rogobete, V. Sandoghdar, Enhancement of Single-Molecule Fluorescence Using a Gold Nanoparticle<? format?> as an Optical Nanoantenna, Physical review letters, 97 (2006) 017402.

[7] G. Baffou, R. Quidant, Thermo‐plasmonics: using metallic nanostructures as nano‐sources of heat, Laser & Photonics Reviews, 7 (2013) 171-187.

[8] D.T. Thompson, Using gold nanoparticles for catalysis, Nano Today, 2 (2007) 40-43.

[9] J. Pérez-Juste, I. Pastoriza-Santos, L.M. Liz-Marzán, P. Mulvaney, Gold nanorods: synthesis, characterization and applications, Coordination chemistry reviews, 249 (2005) 1870-1901.

[10] A. Singh, G. Calbris, N.F. Van Hulst, Vectorial nanoscale mapping of optical antenna fields by single molecule dipoles, Nano letters, 14 (2014) 4715-4723.

[11] A.G. Curto, G. Volpe, T.H. Taminiau, M.P. Kreuzer, R. Quidant, N.F. Van Hulst, Unidirectional emission of a quantum dot coupled to a nanoantenna, Science, 329 (2010) 930-933.

[12] T.H. Taminiau, F.D. Stefani, N.F. van Hulst, Optical nanorod antennas modeled as cavities for dipolar emitters: evolution of sub-and super-radiant modes, Nano letters, 11 (2011) 1020-1024.

5 Skyrmionic topology out of Inverse Faraday Effect

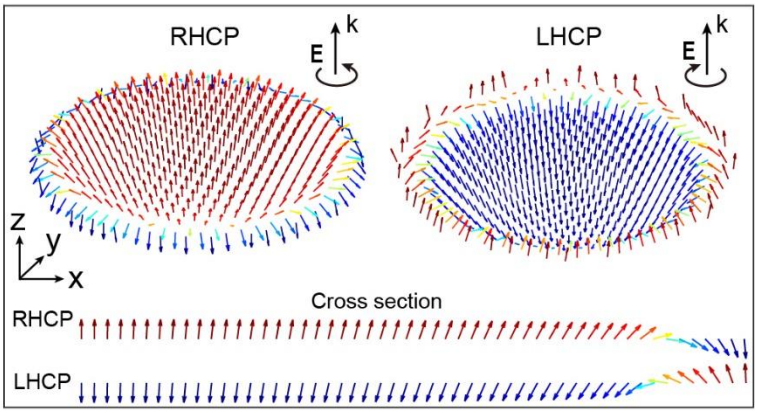

A skyrmion is a topologically stable field configuration constructed by an arbitrary unit vector field[1]. In the previous chapters, we demonstrated the method to generate and manipulate light-induced stationary B fields. In this chapter, we propose to create a skyrmion through the unit vector of the light-induced stationary B field.

5.1 Skyrmion

A skyrmion exhibits diverse topological structures[2]; however, our focus in this chapter centers exclusively on the Néel type. Figure 5-1a displays the schematic of a Néel-type skyrmion. This type is characterized by a continuous rotation of the unit vector field in the plane of the skyrmion, extending seamlessly from its center to its periphery, forming an intricate swirling pattern[3]. Figure 5-1b shows the corresponding normal perspective of this skyrmion. The Néel-type skyrmion has high circular symmetry in the XY plane and closely resembles the stationary B field generated by a DC annular current through the Biot-Savart law. Figure 5-1c and Figure 5-1d depict one method of attaining such a vectorial distribution in the magnetic field, involving the generation of two counter-propagating currents with different radii. Figure 5-1d shows the unit vector field of the induced stationary B field by DC current in Figure 5-1b. The similar configuration in Figure 5-1a and Figure 5-1d indicates the possibility of creating this Néel-type skyrmion through a stationary B field.

Based on our experience in the creation and manipulation of light-induced stationary B

fields in the near field, we propose the use of a ring-shaped plasmonic nanoantenna to create this intricate vectorial distribution within a nanoscale magnetic field, as illustrated in Figure 5-1e. Here, the proposed nanoring is positioned on a glass substrate and excited by a right-circularly polarized plane wave coming from the substrate side. Ultimately, we aim to create a Néel-type skyrmion at the nanoscale.

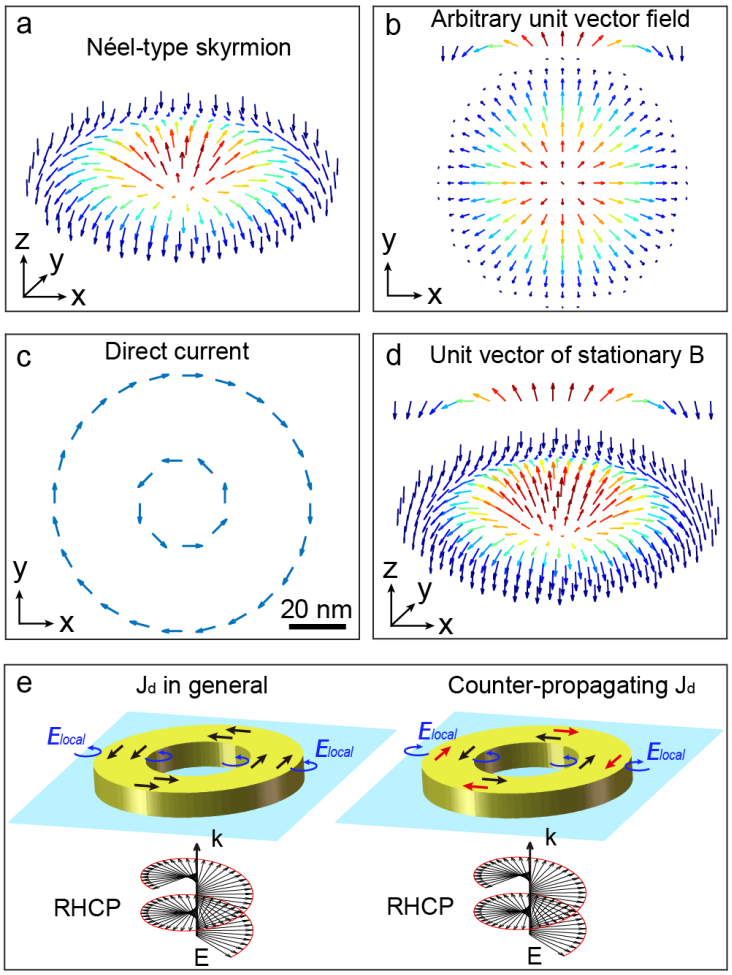

Figure 5-1. Description of a Néel-type skyrmion. (a) 3D and (b) normal perspective of unit vector distribution of a Néel-type skyrmion. The arrows represent the orientation of the vectors, and the colors are the amplitude of their Z component. (c) Distribution of electric direct currents in an XY plane, required for the realization of (d) a skyrmion-like distribution of unit vector field from stationary B field generated by dc currents. (e) Schematic description of the plasmonic nanostructure considered in this study to generate a skyrmionic distribution by light-induced stationary B field, a gold nanoring is placed on a glass substrate and excited by a right circularly polarized plane wave incident from the substrate side. Two cases are considered: drift currents (J_d) propagate in the same direction and in opposite directions between the inner and outer parts of the nanoring. The blue arrows represent the local polarization required to generate the drift currents shown in the drawing, black and red arrows indicate the direction of drift currents.

As shown in Figure 5-1, two counter-propagating DC annular currents can create a skyrmion-like distribution from the unit vector induced stationary B field through the Biot-Savart law. The required DC currents can be generated in the nanoring based on R. Hertel's theory[4], which describes drift currents arising from the interaction between a plasmonic nanoantenna and circularly polarized light. By manipulating this magneto-optical interaction, we can adjust the skyrmion-like vector field and make it a true Néel-type skyrmion. For a Néel-type skyrmion, the skyrmion number (Q) should be ±1. The skyrmion number is defined by the unit vector **u**, expressed as[1]

$$Q = \frac{1}{4\pi}\iint \mathbf{u}\cdot\left(\frac{\partial \mathbf{u}}{\partial x}\times\frac{\partial \mathbf{u}}{\partial y}\right)dxdy \tag{5-1}$$

where

Q	Skyrmion number
u	Unit vector of stationary B field

The skyrmion number in Eq. (5-1) is the criterion for our skyrmion creation, calculated by the unit vector of the light-induced stationary B field.

5.2 Ring-shape nanoantenna

We have already shown that DC drift currents are generated from an Au nanosphere by circularly polarized light in Chapter 4 where the drift currents mainly appear at the edge of the nanosphere. A nanoring, with both its inner and outer edges, can create counter-propagating drift currents. We choose a nanoring as an example, featuring an inner diameter "d" of 120 nm and an outer diameter "D" of 240 nm with a thickness of 30 nm, to explore the condition of exciting counter-propagating drift currents.

5.2.1 Bonding mode

A nanoring can be treated as a combination of two distinct structures: a circular nanohole and a nanopatch, each exhibiting an ED resonance mode[5]. Either the nanohole or the nanopatch can create circulating drift currents under circular polarization. Figure 5-2 displays the drift currents generated by an isolated nanohole and a nanopatch from the nanoring. Each

of them has the same dimensions as in the nanoring and is excited by right circularly polarized light at their respective resonant frequencies. Figure 5-2a and Figure 5-2c show the results for the nanopatch excited by incident light (λ = 754 nm) from the background. Figure 5-2a displays the z component of spin density (s_z) distributed in the XY plane. As demonstrated in Chapter 4, s_z indicates the direction of the drift current, which plays a key role in this research. This spin density is opposite to the incident light, which is consistent with the spin density from two perpendicular, 90° de-phased EDs. The corresponding drift current is depicted in Figure 5-2c. The nanohole is also excited by right circularly polarized light, but with a wavelength of λ = 825 nm. The results are displayed in Figure 5-2b and Figure 5-2d.

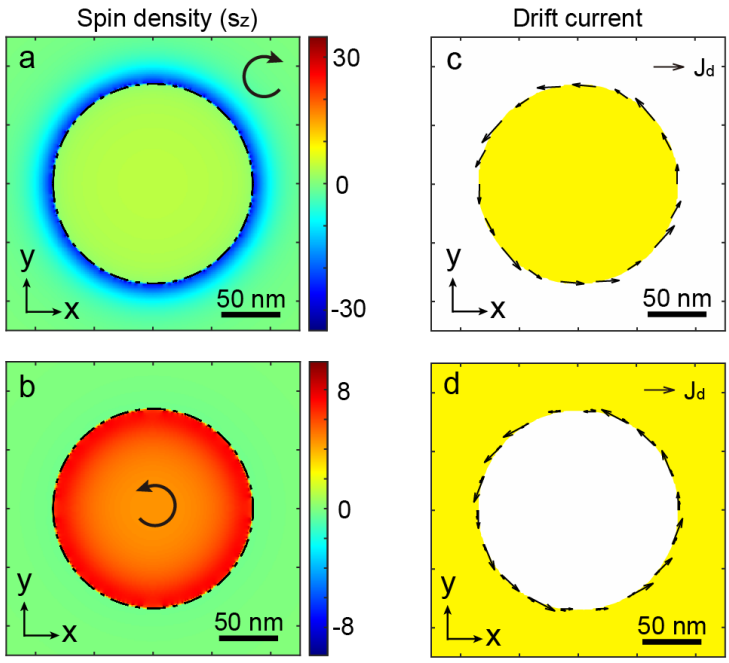

Figure 5-2. Comparison of isolated nanostructure types: nano-patch and nanohole for a 30 nm gold thickness, deposited on a glass substrate, and for excitation at λ = 754 nm and 825 nm with right circular polarization, respectively. Spatial distribution of spin densities in an XY plane at the center Z of a) a nano-patch and b) a nanohole. The arrows represent the helicity of local light near the antennas. An important observation here is that for the same excitation polarization of these plasmonic nanostructures, the local light polarization is opposite. c) and d) Spatial distribution of drift currents associated with the spin densities shown in a) and b), respectively. The length of the arrows represents the relative amplitude of drift currents.

In summary, for isolated nanopatch and nanohole excited by RHCP light, both create counterclockwise drift currents in the XY plane. For a structure combined from the nanopatch and nanohole, the nanoring exhibits characteristics from their respective parts. We show the corresponding results in Figure 5-3.

Figure 5-3a illustrates the spectral response of the electric field enhancement at the XYZ center of a nanoring. Notably, the structure exhibits two resonances in its spectral response[6-8]: one weaker around 570 nm and the other more pronounced at approximately 1100 nm. The stronger resonance represents the most general situation. Let's initially delve into the characteristics of the stronger resonance. In Figure 5-3b, the electric field distribution in the XY plane at the Z center of the structure is delineated at a wavelength λ of 1100 nm. This visualization reveals a notable increase in the electric field both inside and outside the nanoring at this specific wavelength.

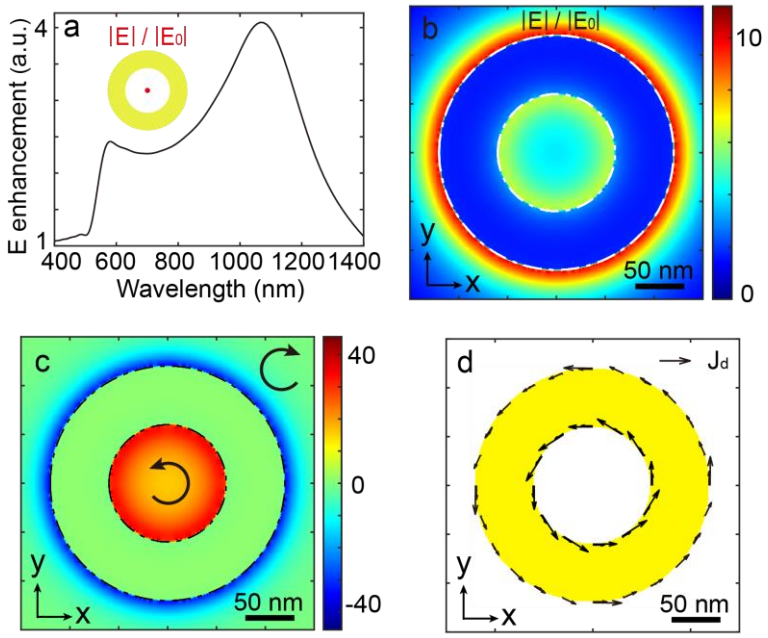

Figure 5-3. Description of the physical behavior of the nanoring. a) Spectral response in terms of electric field enhancement at the XYZ center of a nanoring with an inner diameter of 120 nm, outer diameter of 240 nm, and thickness of 30 nm. Spatial distribution in an XY plane at the Z center of the nanoantenna for b) electric field enhancement normalized by the incident field, c) spin density, and d) drift currents.

Then, Figure 5-3c shows the spin density distribution in the same plane as the field in Figure 5-3b. As described in Chapter 2 and Chapter 4, spin density is related to direction of drift current. While its direction plays a key role in the creation of Neel-type skymion. Figure 5-3c displays Z component of spin density describing the handedness of light in XY plane. A positive spin density in our reference system signifies a right helicity, a negative spin density corresponds to a left helicity, and a zero density denotes linear polarization. From Figure 5-3c, it is apparent that the spin densities within and outside the ring exhibit opposite signs. This local light polarization state does not align with the prerequisite for counter-propagating drift

currents, as explained earlier and detailed in Figure 5-1c. Because in this case, the currents will flow in the same direction, as illustrated in Figure 5-3d, and it will not generate a skyrmionic structure through light-induced stationary B field.

5.2.2 Anti-bonding mode

Nevertheless, these annular plasmonic structures are known in the literature for supporting a diversity of modes. The combination of the nanohole and nanopatch results in the ability to sustain two distinctive coupled modes (Figure 5-4a): a bonding mode (commonly referred to as a bright mode) and an anti-bonding mode (commonly referred to as a dark mode)[9]. The manifestation of these modes becomes evident when examining the spectral response with respect to charge density (Figure 5-4b) within the inner and outer metallic components of the antenna. Charge density distributions corresponding to the bonding and anti-bonding modes identified in Figure 5-4b are presented in Figure 5-4c and Figure 5-4d, respectively. As anticipated, the charge densities between the inner and outer regions of the antenna exhibit an out-of-phase relationship for the anti-bonding mode, while they are in phase for the bonding mode. Upon inspecting the spectral response regarding spin densities for the inner and outer segments of the nanoring (Figure 5-4e), it is evident that polarizations are opposite in the case of the bonding mode (at λ = 1100 nm in Figure 5-4e). In contrast, for the anti-bonding mode, the spin densities exhibit the same sign within a specific wavelength range (at λ = 570 nm in Figure 5-4e).

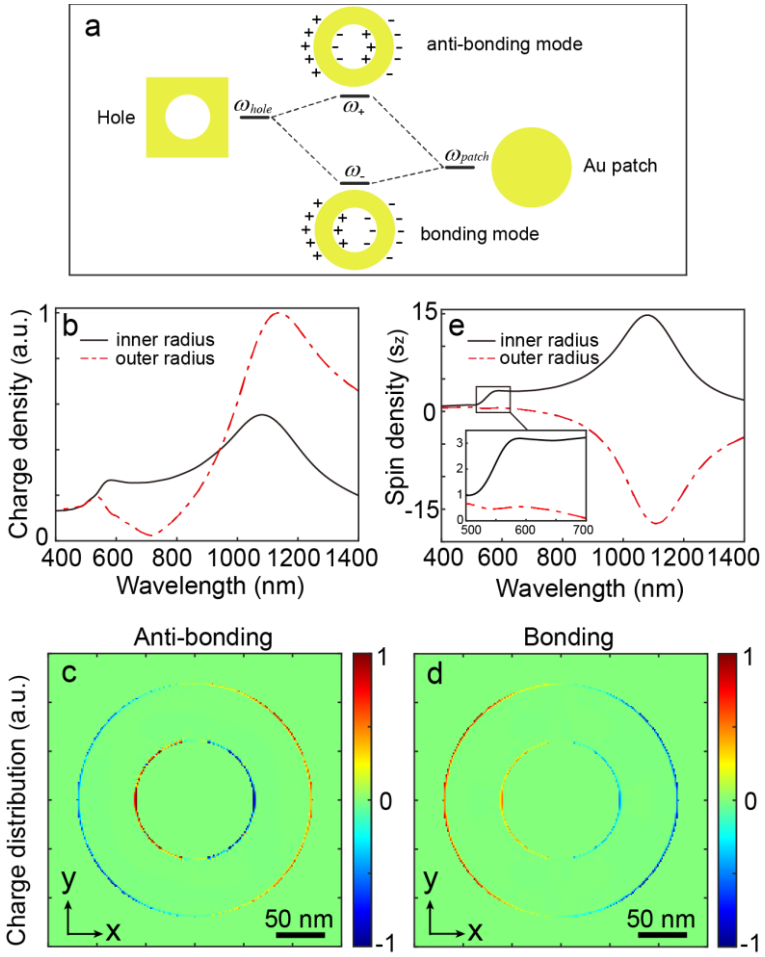

Figure 5-4. Multipolar behavior of the nanoring. a) A nanoring can be seen as the combination of two distinct structures, namely a nanohole and a nanopatch. Each of these structures has its resonance mode, and their coupling results in a structure itself carrying two resonance modes, one bright, known as bonding, at a lower frequency, and the other dark, known as anti-bonding, at a higher frequency. b) Spectral response in terms of electron density for the inner (black line) and outer (red dashed lines) parts of the metal. Spatial distributions of electron densities in an XY plane at the Z center of the nanoring for c) the anti-bonding mode and d) the bonding mode. e) Spectral response in terms of spin density for the inner (black line) and outer (red dashed line) parts of the nanoring. A zoom of the portion corresponding to the anti-bonding mode is shown in the inset

To illustrate this difference, Figure 5-5a and Figure 5-5b present spin density distributions in the XY plane at the Z center of the nanoring for the two modes inherent in this antenna. The contrasting polarizations are clearly visible in these depictions. Subsequently, Figure 5-5c and Figure 5-5d exhibit the drift currents corresponding to the spin densities in Figure 5-5a and Figure 5-5b. In the bonding mode, we observe that the drift currents propagate in the same

direction within the inner and outer regions of the nano-antenna. In contrast, in the scenario of the anti-bonding mode, the currents exhibit counter-propagation on each side of the nanoring. Consequently, this dark mode is anticipated to facilitate the generation of a skyrmionic topological distribution through the light-induced stationary B field, as illustrated in Figure 5-1c and Figure 5-1d.

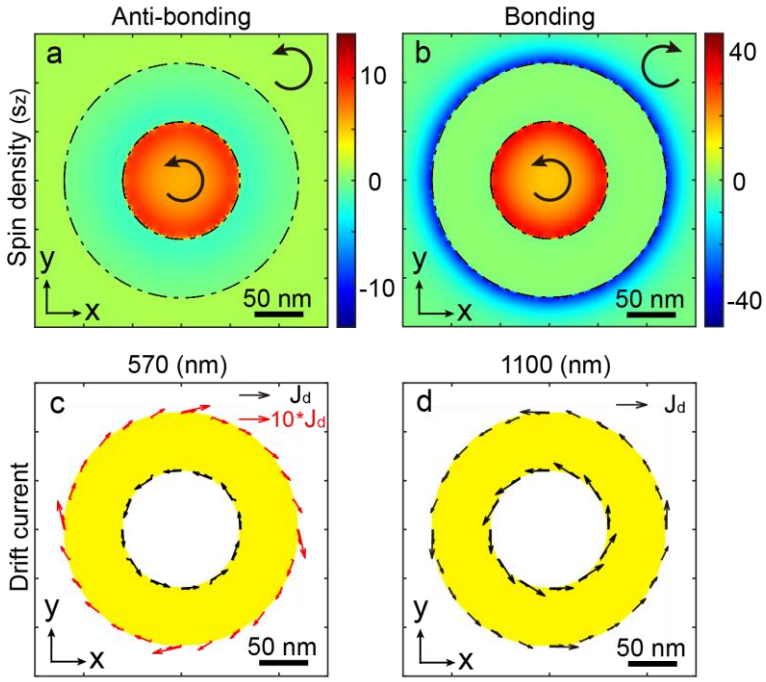

Figure 5-5. Comparison of dark and bright modes in the nanoring. Spatial distributions of spin densities in an XY plane at the Z center of the plasmonic nanostructure for a) the anti-bonding mode (λ = 570nm) and b) the bonding mode (λ = 1100 nm). Arrows represent the helicity of light. Spatial distributions of drift currents in an XY plane at the Z center of the nanoring for c) the anti-bonding mode and d) the bonding mode. The length of the arrows represents the relative amplitude of the generated photocurrents.

The dissimilarity in local polarization between these two modes is found in the dipolar nature of the bonding mode and the coupling between two dipolar modes within the anti-bonding mode. We will explain this by examining the coupling of the E field from the induced ED source in the near field.

5.2.3 Explanation of spin density in nearfield

The spin density itself characterizes the handedness of local elliptically polarized light,

and the local polarization state, or the near-field electric field, is directly influenced by the charge distribution in Figure 5-4c and Figure 5-4d. Notably, the two intrinsic modes exhibit entirely different charge distributions. Figure 5-6 shows a schematic of the interaction between ED sources.

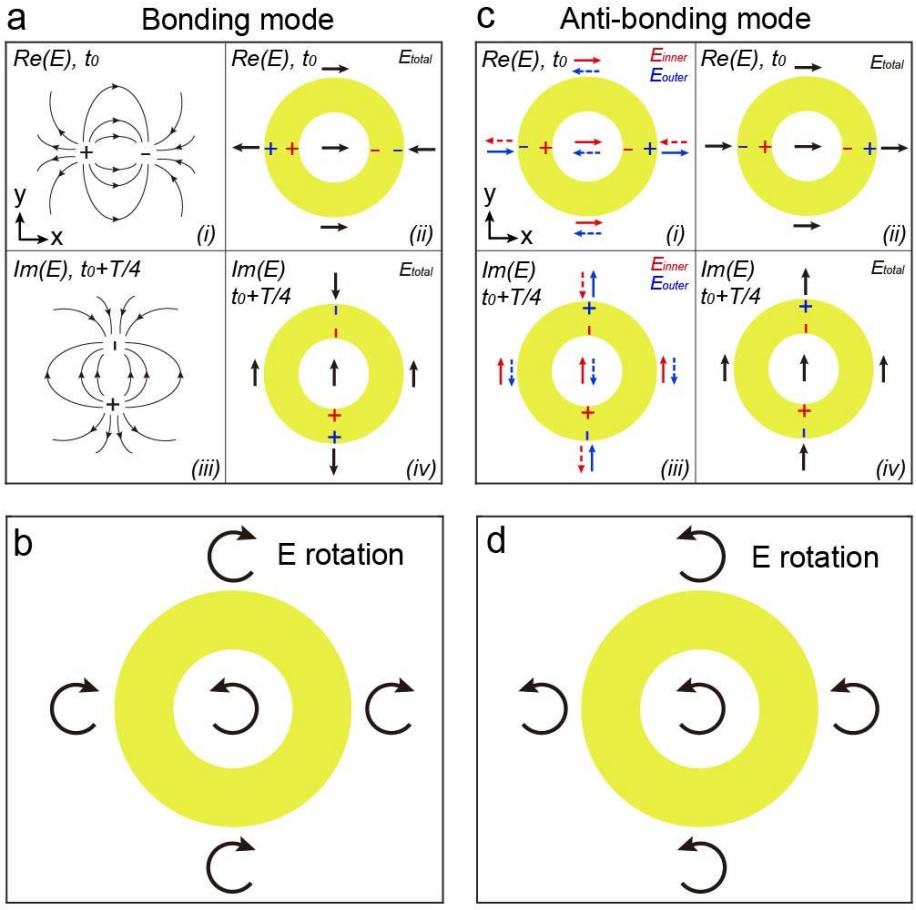

Figure 5-6. Dipolar study of bonding and anti-bonding modes. a) Spatial orientation in an XY plane of the electric field for i) a dipole oriented along X, ii) the nanoring excited by right circular polarization at t0 and at the wavelength of the bonding mode, iii) an electric dipole oriented along Y, and iv) the nanoring excited by right circular polarization at t0 + T/4 and at the wavelength of the bonding mode. b) Local polarization resulting from excitation of the nanoring by right circular polarization for the bonding mode. The arrows represent the helicity of light. c) Spatial orientation of the electric field resulting from the coupling between two opposite dipolar modes for excitation by right circular polarization of the nanoring at the wavelength of the anti-bonding mode at i, ii) t0 and iii, iv) t0 + T/4. In i) and iii), the red arrows represent the contribution of the inner dipole of the nanoring, the blue arrows represent that of the outer dipole, and the solid arrows represent the main contributions. In ii) and iv), the black arrows represent the orientation of the total electric field once the contributions of each dipole are taken into account. d) Local polarization resulting from excitation of the nanoring by right circular polarization for the anti-bonding

mode. The arrows represent the helicity of light.

In the case of the bonding mode, depicted in Figure 5-6a, it is composed of two parallel electric dipoles (ED). Each ED exhibits a spider-like electric field distribution in the near field. Consequently, the total electric field results from the contribution of both EDs, producing the same electric field distribution as shown in Figure 5-6a. To assess the handedness of the local light, the orientation of the electric field at different times is indicated by black arrows in Figure 5-6a(ii, iv). Considering that the nanoring is excited by right-handed circularly polarized (RHCP) light, the charge distribution and electric field undergo a 90-degree rotation after a quarter time period, as seen in Figure 5-6a(i, ii) and Figure 5-6a(iii, iv). In a complex representation, the electric field distribution in Figure 5-6a(i, ii) and Figure 5-6a(iii, iv) can be treated as the real and imaginary parts of the electric field. The change of orientation between Re(E) and Im(E) (alternatively between t0 and t0+T/4) reveals the handedness of local elliptical light, as depicted in Figure 5-6b. This distribution is further validated by numerical simulation results from Lumerical FDTD. Figure 5-7(a, b) and Figure 5-7(c, d) display the real (Re(E)) and imaginary (Im(E)) parts of the distribution at 1100 nm (bonding mode), respectively. The opposite handedness inside and outside the nanoring aligns with the spin density distribution in Figure 5-4b.

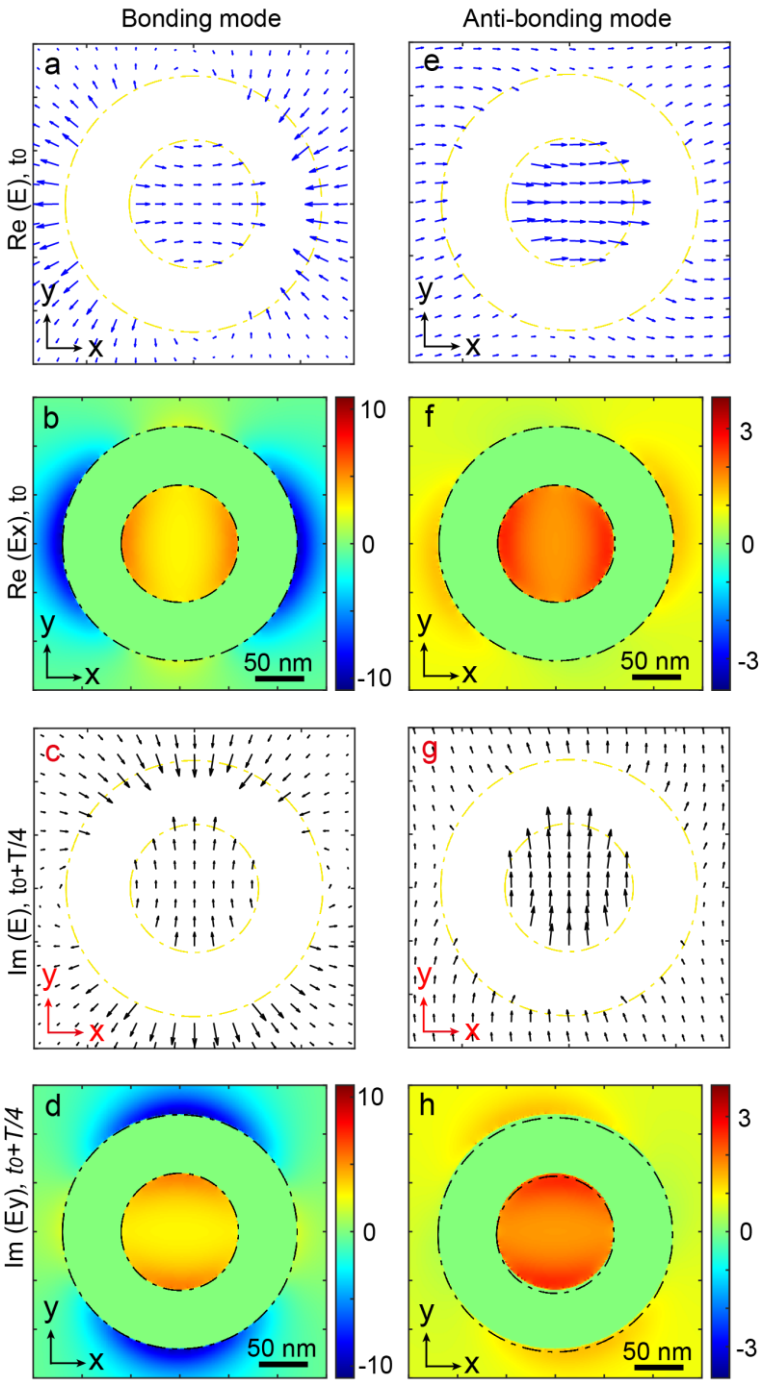

Figure 5-7. Distribution of electric fields in the nanoring for bonding (λ = 1100 nm) and anti-bonding (λ = 570 nm) modes at different times in an optical cycle and excited by right circularly polarized light. a, c) Vectorial distribution and b, d) amplitude of the electric field component in an XY plane at the center Z of the nanoring at a, b) t=t0 and c, d) t=t0 + T/4 for the bonding mode. e, g) Vectorial distribution and f, h) amplitude of the electric field component in an XY plane at the center Z of the antenna for times e, f) t = t0 and g, h) t=t0 + T/4 in the case of the anti-bonding mode.

A similar analysis is applied to the anti-bonding mode, but it is more intricate due to the opposing EDs in Figure 5-6c. In this case, the total electric field combines contributions from the inner (E_inner - red) and the outer (E_outer - blue) EDs. These two EDs exhibit destructive interference in the near field, and the orientation of the total electric field is determined by the relative strength of the local E_inner and E_outer. The strength of the local E_inner and E_outer depends on the intensity of the ED and the distance to each ED source. According to the spectrum of charge density in Figure 5-4b, the anti-bonding mode appearing at 570 nm has a relatively stronger inner ED and a weaker outer ED. Consequently, E_inner is stronger than E_outer at positions farther from the two ED sources, which are the top, bottom, and middle positions in Figure 5-6c(i). Here, the solid line indicates a stronger local electric field, while the dashed line indicates a weaker local electric field. As for the left and right positions in Figure 5-6c(i), they are situated next to the outer ED. In this small region, E_outer will be stronger than E_inner, benefiting from the shorter distance to the source. As a result, the total electric field has a nearly homogeneous distribution in the near field, as shown in Figure 5-6c(ii). Subsequently, the total electric field undergoes a 90-degree rotation after a quarter time period considering RHCP incident light, as depicted in Figure 5-6c(iii and iv). Figure 5-7(e, f) and Figure 5-7(g, h) display the real (Re(E)) and imaginary (Im(E)) parts of the distribution at 570 nm (anti-bonding mode), respectively. The homogeneous handedness inside and outside the nanoring aligns with the spin density distribution in Figure 5-4a.

5.3 Searching for skyrmion

Since we have explained the principle of creating the same spin density around the nanoring to generate counter-propagating drift currents that enable a skyrmion-like stationary B field, the next step is to optimize the geometric dimensions of the nanoring for a real Néel-type skyrmion. We explore the dimensions needed to induce drift currents in both the internal and external regions of the nanoring, resulting in a skyrmion by the unit vector of the stationary B field with uniform magnetic amplitude. Figure 5-8 explores the set of parameters “d” and “D” to achieve a skyrmionic vector distribution of the magnetic field. In Figure 5-8a, the skyrmion number of the nanoring is presented for excitation at a wavelength of 600 nm, considering various values of "d" and "D" with a gold thickness of 30 nm. The skyrmion number, defined in Eq. (5-1), is used to characterize the winding of spins in the magnetic texture.

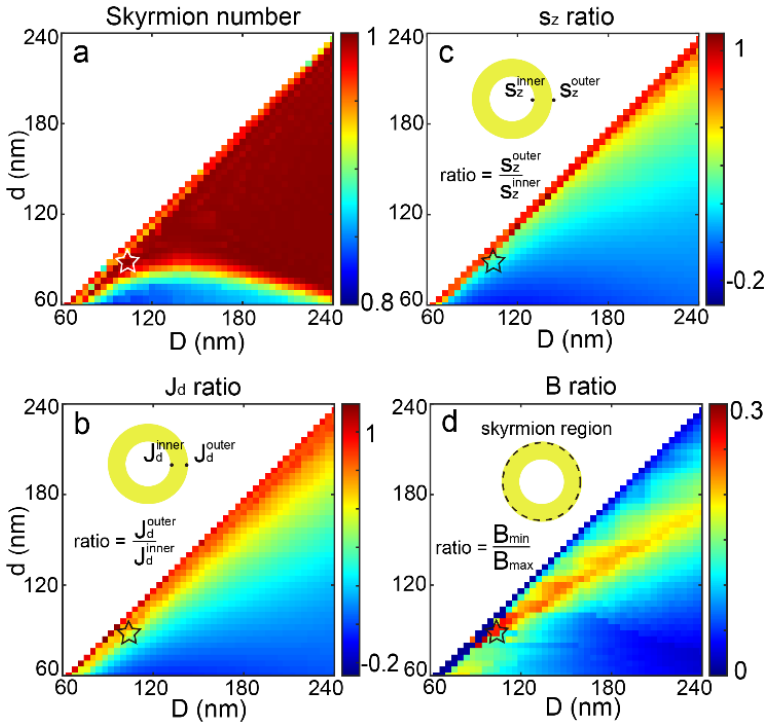

Figure 5-8. Study of skyrmion generation by light-induced stationary B field for different inner "d" and outer "D" nanoring diameters, with a 30 nm gold thickness and excitation at λ = 600 nm. The selected nanoring is marked by a star. a) Skyrmion number values. b) Ratio of spin density values along Z between the inner and outer parts of the plasmonic nanostructure. c) Ratio of drift currents (absolute values) associated with the spin densities shown in b) between the inner and outer parts of the nanoring. d) Ratio of magnetic field amplitudes generated from the drift currents shown in c) between the inner and outer parts of the plasmonic nanoantenna

In our investigation, the vectorial distribution closest to a perfect Néel-type skyrmionic topology is observed when the skyrmion number, Q, approaches ±1. The sign of Q dictates the up or down orientation of the magnetic field at the center of the antenna. Figure 5-8a illustrates that numerous pairs of parameters, "d" and “D", can yield a value of Q close to 1, indicating that various physical parameters can be manipulated to achieve a skyrmion. Despite the magnetic field's vector distribution taking on a skyrmionic topology, our objective was to develop a plasmonic nanoantenna with a relatively uniform magnetic field amplitude in this vectorial distribution.

Figure 5-8b presents the ratio of spin density amplitudes between the inner and outer segments of the nanoring for different diameter values. This ratio aligns well with the ratio of drift countercurrents between the inner and outer metal components, as depicted in Figure 5-8c. Additionally, we calculate the ratio of magnetic fields on either side of the nanoring walls, as

illustrated in Figure 5-8d. This figure provides a range of parameters that enable the skyrmionic distribution to exhibit a relatively homogeneous magnetic field amplitude.

5.4 Neel-type skyrmion constructed by stationary B field

Based on the results in Figure 5-8, we selected the dimensions to create a perfect skyrmion. The selected nanoantenna is displayed in Figure 5-9a, having a thickness of 30 nm, an inner diameter of 88 nm, and an outer diameter of 104 nm. For this optimized nanoantenna, we consider two types of optical excitations: right-circularly polarized and left-circularly polarized. Figure 5-9b and Figure 5-9c illustrate the normalized distribution of the Z-component of the optically induced magnetic field. It is normalized by the magnetic field in the center, where |B| = Bz, in the case of right- and left-circular polarizations, respectively. These vector distributions are perfectly inverted in orientation, as shown in Figure 5-9d and Figure 5-9e, presenting these fields in 3D at 1 nm from the gold surface of the antenna.

Figure 5-9d and Figure 5-9e present the unit vector of this light-induced stationary B field. As observed, a skyrmionic topological distribution manifests on the surface of this antenna. The magnetic field is perpendicular to the surface at the center of the antenna, progressively rotating within the skyrmion plane from the center to the periphery of the antenna, forming a swirling pattern that completely reverses at the edge of the nanoantenna. To illustrate this vectorial motion in space, Figure 5-9f displays the orientation of the magnetic field and its unit vector for a linecut from the center to the edge of the antenna. The spatial inversion of the magnetic field is evident, with the magnetic field maintaining the same sign over the entire nanoantenna, and a flip of the magnetic field occurring at the end of the nanostructure.

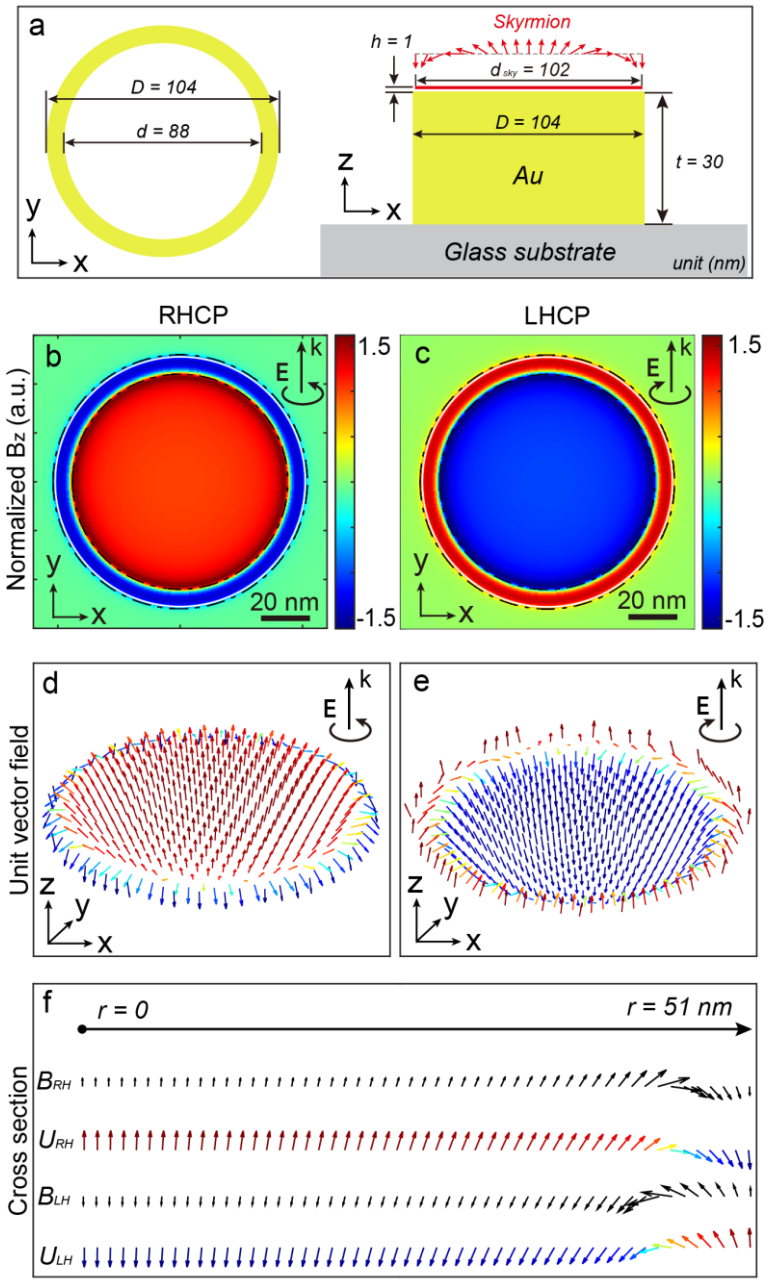

Figure 5-9. Example of a nanostructure generating a perfect Néel-type skyrmion for excitation at λ = 600 nm. a) Schematic representation of a nanoring enabling the generation of a Néel-type skyrmion by IFE. Its dimensions include an inner diameter of 88 nm, an outer diameter of 104 nm, and a 30 nm gold thickness. Spatial distribution of the normalized magnetic field along Z generated by IFE in an XY plane 1 nm above the nanoring for b) right and c) left circularly polarized optical excitation, in this presentation B at center is set to be 1. d) and e) 3D vectorial distribution of normalized magnetic fields represented in b) and c), respectively. f) Line cut of vectorial distributions of magnetic fields in amplitudes (B) and normalized (U) from the center to the edge of the nanostructure for right-handed (RH) and left-handed (LH) circular

polarizations

This outcome is particularly noteworthy, aligning with the observed behavior in many skyrmionic spin structures found in magnetic materials[10]. This characteristic could facilitate the implementation of such vectorial structures in magnetic materials using plasmonic-enhanced light-induced stationary B fields. Additionally, the composition of magnetic materials defines the physical size of skyrmionic topologies. Thus, the ability to adjust the size of the vectorial distributions with this symmetry by changing the dimensions of plasmonic nanostructures would be a valuable advantage in the all-optical generation of skyrmions.

5.5 Conclusion

In conclusion, our theoretical investigation has demonstrated that the manipulation of light in the near field enables the generation of a vectorial magnetic field distribution exhibiting the topology of a Néel-type skyrmion. The induced Néel-type skyrmion has a skyrmion number of ±1 for right-handed circular polarization and left-handed circular polarization, respectively.

This novel observation arises from utilizing the anti-bonding mode (or dark mode) in a ring-shaped gold nanostructure. In the anti-bonding mode, the nanoantenna generates a pure spin density around it. According to our previous studies, the direction of the drift current is related to the spin density in the local area. In the case of a pure spin density around the nanoantenna, two counter-propagating drift currents are induced in the inner and outer segments of the ring.

We attribute the pure spin density, or the same polarization state in other words, to the complex interaction of the electric field in the near field. When the nanoring is excited by circularly polarized light, we perform a linear decomposition of this response. The total E field is decomposed into the responses from two perpendicular, 90° de-phased, linearly polarized incident lights. Therefore, we only need to focus on one of the linear responses, and we can infer the other by using the circular symmetry. For each linear excitation, the nanoring is treated as a composition of a hole and a patch, each sustaining an ED resonance. Both contribute to the total E field under linear polarization excitation, and the distribution of the E field plays a key role, as demonstrated in the schematic illustration in Figure 5.6. In the anti-bonding and bonding modes, the nanoantenna exhibits quite different charge distributions. This difference results in distinct E field distributions in the near field, leading to different polarization states.

Therefore, we explain this pure spin density by the complex interaction of the E fields from four ED resonances, which leads to two counter-propagating drift currents and a skyrmion-like stationary B field. Furthermore, we have demonstrated that a diverse set of parameters can be employed to achieve this anti-bonding mode and, consequently, a vectorial distribution characteristic of a skyrmion. We show the induced stationary B field as well as its unit vector distribution that constructs the Néel-type skyrmion. By replacing the incident light from RHCP to LHCP, we can flip the skyrmion in the Z direction, leading to the exchange of the skyrmion number from (+1) to (-1)

Ultimately, this distribution was illustrated through a case study showing the reversal of the magnetic field orientation in the spatial vector distribution from the center to the edge of the plasmonic structure. This behavior aligns well with the anticipated characteristics of skyrmion symmetry. The findings presented in this study represent a significant advancement in the generation and manipulation of nanoscale magnetic field distributions by the IFE.

This research may find applications in various fields, including manipulating magnetic processes, ultrafast magnetic modulation, magnetic trapping, spin currents, and spin precession, with direct applications such as ultrafast data writing and processing.

REFERENCE

[1] B. van Dijk, Skyrmions and the dzyaloshinskii-moriya interaction, 2015.

[2] Y. Shen, E.C. Martínez, C. Rosales-Guzmán, Generation of optical skyrmions with tunable topological textures, ACS Photonics, 9 (2022) 296-303.

[3] Y. Tokura, N. Kanazawa, Magnetic skyrmion materials, Chemical Reviews, 121 (2020) 2857-2897.

[4] R. Hertel, Theory of the inverse Faraday effect in metals, Journal of magnetism and magnetic materials, 303 (2006) L1-L4.

[5] M. Grande, M.A. Vincenti, T. Stomeo, G. Morea, R. Marani, V. Marrocco, V. Petruzzelli, A. D'Orazio, R. Cingolani, M. De Vittorio, Experimental demonstration of a novel bio-sensing platform via plasmonic band gap formation in gold nano-patch arrays, Optics Express, 19 (2011) 21385-21395.

[6] J. Aizpurua, P. Hanarp, D. Sutherland, M. Käll, G.W. Bryant, F.J. García de Abajo, Optical properties of gold nanorings, Physical review letters, 90 (2003) 057401.

[7] E. Prodan, C. Radloff, N.J. Halas, P. Nordlander, A hybridization model for the plasmon response of complex nanostructures, science, 302 (2003) 419-422.

[8] M. Jahn, S. Patze, I.J. Hidi, R. Knipper, A.I. Radu, A. Mühlig, S. Yüksel, V. Peksa, K. Weber, T. Mayerhöfer, Plasmonic nanostructures for surface enhanced spectroscopic methods, Analyst, 141 (2016) 756-793.

[9] E. Prodan, P. Nordlander, Plasmon hybridization in spherical nanoparticles, The Journal of chemical physics, 120 (2004) 5444-5454.

[10] I. Gross, W. Akhtar, A. Hrabec, J. Sampaio, L. Martínez, S. Chouaieb, B. Shields, P. Maletinsky, A. Thiaville, S. Rohart, Skyrmion morphology in ultrathin magnetic films, Physical Review Materials, 2 (2018) 024406.

6 Summary and prospect

In this PhD project, we demonstrated a method to manipulate the inverse Faraday effect (IFE) at the nanoscale. We began by introducing the theory of IFE, the corresponding light-induced DC current, and the stationary magnetic field. Then, we explored the direction dependence of drift current. According to our study, the direction of the drift current is related to the local polarization state. We described the polarization state of local light through the concept of spin density. By designing plasmonic nanoantennas, we were able to manipulate the local light and, consequently, the light-induced DC drift current. Drift currents were capable of generating a stationary magnetic field via the Biot-Savart law. Therefore, we could manipulate the corresponding stationary magnetic field through these drift currents, achieving different research goals by IFE.

6.1 Ultrafast, strong stationary magnetic field

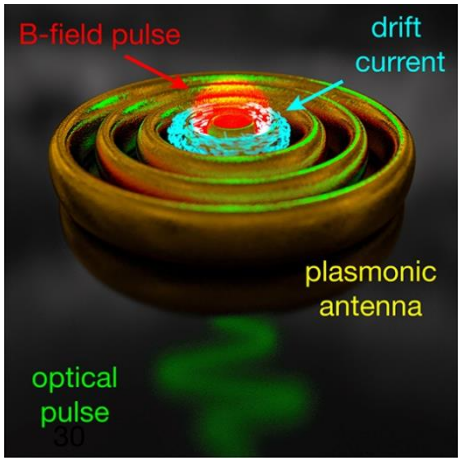

Figure 6-1. Ultrafast, strong stationary magnetic field through bull-eye nanoantenna

In this research, we designed a bullseye nanoantenna and created an ultra-strong stationary magnetic field at its center. The bullseye nanoantenna is composed of multiple concentric golden rings, which can efficiently confine electromagnetic energy in the near field through plasmonic resonance. We then introduced a genetic algorithm to optimize the geometric dimensions of the nanoantenna. For the optimized nanoantenna, the light-induced

stationary magnetic field is effectively confined in the central area and reaches the tesla range, with a response time within a few femtoseconds. We analyzed the optimized bullseye nanostructure and physically explained the origin of these strong magnetic fields. Finally, we studied the time-domain response of this stationary magnetic field. Numerical calculations verified that the generation of this ultra-strong stationary magnetic field is superfast, occurring within a few femtoseconds. As a result, an ultrafast, confined, and strong stationary magnetic field was efficiently generated by our bullseye plasmonic nanoantenna.

The bull-eye nanoantenna was optimized using a genetic algorithm (GA). In this GA optimization, it was challenging to distinguish local optimal results. To avoid local optimal results, we chose to launch GA optimization three times. The disadvantage of this approach is the increased time cost, as we spent triple the resources. Another method to address this issue is to improve the algorithm itself. It is possible to increase the efficiency of GA optimization by designing a better loss function and better evolutionary logic, making the GA more robust against local optimal traps.

6.2 Stationary magnetic field through linearly polarized incident light

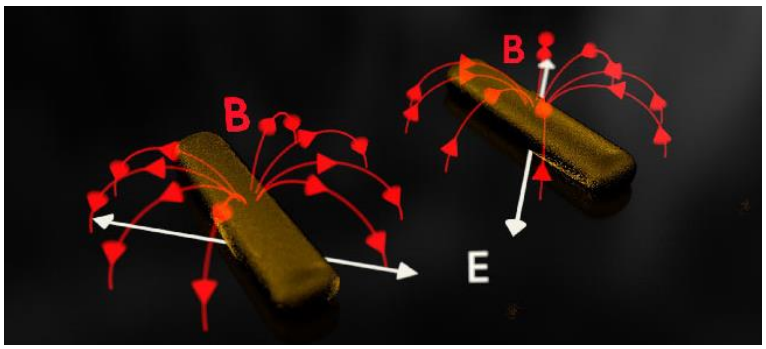

Figure 6-2. Schematic of plasmonic nanorod and light-induced stationary B field by linearly polarized incident light.

In this project, we demonstrated the generation of a stationary magnetic field in a gold nanorod through linearly polarized incident light. In many nano-optical studies, nanoantennas have shown multiple abilities to manipulate electromagnetic fields in the near field. Here, we take advantage of the polarization conversion property of the plasmonic nanorod. Under specific light conditions, a gold nanorod can generate a local circularly polarized field through linearly polarized incident light, making it possible to create a stationary magnetic field with linearly polarized light. The nanorod has two intrinsic modes, and the coupling between these

modes results in local elliptically polarized light. Elliptically polarized light is exactly the excitation condition for the inverse Faraday effect (IFE). By manipulating the local polarization state, we successfully generated circulating drift DC current in the nanorod, thereby creating a stationary magnetic field.

Linearly excited IFE is rarely mentioned in many research studies. Here, we have theoretically demonstrated this light-induced stationary magnetic field. In further investigations, we hope to experimentally verify this phenomenon. The IFE excited by linearly polarized incident light, as demonstrated in this thesis, is more flexible, allowing us to manipulate IFE through the polarization of linearly polarized incident light. This represents a new degree of freedom in IFE manipulation, enabling us to easily adjust the strength and sign of the induced stationary magnetic field by simply changing the polarization angle. Because of its all-optical nature, this light–matter interaction paves the way for ultrafast nanomanipulation of magnetic processes such as domain reversal, skyrmions, circular dichroism, and control of spin, its currents, and waves, among others.

6.3 Skyrmionic topology out of Inverse Faraday Effect

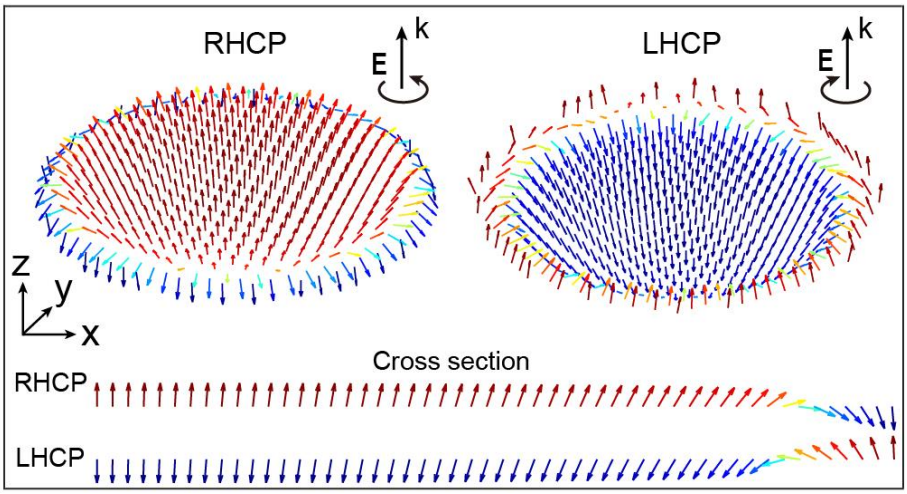

Figure 6-3. Neel-type skyrmion constructed by unit vector of light-induced stationary magnetic field at RHCP and LHCP.

In this research, we proposed creating a Néel-type skyrmion through a light-induced stationary B field. Skyrmions are topologically stable quasiparticles that have been predicted and demonstrated in quantum fields, solid-state physics, and magnetic materials. Skyrmions can be constructed by unit vector fields of optical E, H, spin density vectors, etc. Here, we

proposed constructing a skyrmion using a stationary magnetic field. In this project, we manipulated the distribution of the stationary B field generated by DC current in a plasmonic gold nanoring and thereby constructed a Néel-type skyrmion.

We chose the nanoring due to its two intrinsic resonant modes, named the bonding mode and anti-bonding mode (also known as bright mode and dark mode), respectively. These two modes originate from the coupling between the disk part and the cavity part of the nanoring. We discovered that in the anti-bonding mode, the nanoring created the same spin density inside and outside of the nanoring. According to our demonstration in Chapter 2, spin density indicates the direction of the drift current. For the same spin density distribution around the nanoring, it created two counter-propagating drift currents at the inner and outer edges. These counter-propagating drift currents could generate a skyrmion-like stationary magnetic distribution.

We then manipulated the induced stationary magnetic field by adjusting the geometric size of the nanoring. In this way, we transformed the skyrmion-like stationary magnetic distribution into a Néel-type skyrmion. Finally, by exciting the anti-bonding mode of the nanoring with RHCP and LHCP incident light separately, we successfully reversed the skyrmion number from +1 to -1

This research was illustrated through a case study showing the reversal of the magnetic field orientation in the spatial vector distribution from the center to the edge of the plasmonic structure. This behavior aligns well with the anticipated characteristics of skyrmion symmetry. We proposed a method to create and manipulate a skyrmion constructed by a light-induced stationary magnetic field. The skyrmion is confined at the nanoscale, realized by all-optical means, and benefits from plasmonic resonance. This confined, optically induced skyrmion from the stationary magnetic field might find applications in many areas. The findings presented in this study represent a significant advancement in the generation and manipulation of nanoscale magnetic field distributions by the IFE.

Acknowledgments

I couldn’t have finished my PhD project and thesis without the help of many people over the past four years. I’d like to take this opportunity to thank them for their support.

First, my sincere thanks to my supervisor and personal PhD committee. My supervisor, Mathieu Mivelle, provided invaluable help, both in academic research and in daily life. For a newcomer to France like me, his assistance was particularly significant. I would also like to thank my personal PhD committee members, Lionel Aigouy and Vidal Franck, for their willingness to spend time listening to my CST report every year and for their patience and support.

Next, thanks to all the members of our research team: Agnes Maitre, Laurent Coolen, Catherine Schwob, Bruno Gallas, Eric Charron, Maria Sanz-Paz, Hugo Defienne, Yoann Prado, and Willy Daney de Marcillac. They offered me invaluable academic support over the past years. In particular, I would like to thank Agnes Maitre for giving me the opportunity to join this excellent team.

I also appreciate my colleagues, Ye Mou, Lingfei Cui, Benoit Reynier, Homero Restrepo Zapata, Shuhui Yang, Pascale Nasr, and Obren Markovic, along with the students who are currently employed or have graduated from our team.

In the end, thanks for the support in daily life from my girlfriend Mimi Tian.

Thanks to the financial support from Chinese Scholarship Council (CSC) and Sorbonne University.

Activities and achievements

Publications

[1] Tesla-range femtosecond pulses of stationary magnetic field, optically generated at the nanoscale in a plasmonic antenna
X Yang, Y Mou, B Gallas, A Maitre, L Coolen, M Mivelle
ACS nano 16 (1), 386-393, (2021).

[2] An inverse Faraday effect generated by linearly polarized light through a plasmonic nano-antenna
X Yang, Y Mou, R Zapata, B Reynier, B Gallas, M Mivelle
Nanophotonics 12 (4), 687-694, (2023).

[3] Achiral Magnetic Photonic Antenna as a Tunable Nanosource of Chiral Light
L Cui, X Yang*, B Reynier, C Schwob, S Bidault, B Gallas, M Mivelle*
ACS photonics 10 (11), 3850-3857, (2023).

[4] Full control of electric and magnetic light–matter interactions through a nanomirror on a near-field tip
B Reynier, E Charron, O Markovic, X Yang, B Gallas, A Ferrier, S Bidault, M Mivelle
Optica 10 (7), 841-845, (2023).

[5] A reversed inverse Faraday effect
Y Mou, X Yang, B Gallas, M Mivelle
Advanced Materials Technologies 8 (21), 2300770, (2023).

[6] A chiral inverse Faraday effect mediated by an inversely designed plasmonic antenna
Y Mou, X Yang, B Gallas, M Mivelle
Nanophotonics 12 (12), 2115-2120, (2023).

[7] A Magnetic Monopole Antenna
B Reynier, X Yang, B Gallas, S Bidault, M Mivelle
ACS photonics 10 (9), 3070-3076, (2023).

[8] Femtosecond drift photocurrents generated by an inversely designed plasmonic antenna
Y Mou, X Yang, M Vega, R Zapata, B Gallas, J Bryche, A Bouhelier, M Mivelle
Nano Letters, (2024).

Attended international conference

Conference: Nanophotonics and Micro/Nano Optics International Conference 2022 (NANOP 2022)
Activity: oral presentation.
Title: An Inverse Faraday effect generated by linearly polarized light through a plasmonic nano-antenna
*Xingyu Yang, Ye Mou, Homero Zapata, Benoît Reynier, Bruno Gallas, and Mathieu Mivelle**
Sorbonne Université, CNRS, Institut des NanoSciences de Paris, INSP, F-75005 Paris, France